POLITECNICO

MILANO 1863

SCUOLA DI INGEGNERIA INDUSTRIALE
E DELL'INFORMAZIONE

Aerogel-based collection of ejecta material from asteroids from Libration point orbits: dynamics and capture design

TESI DI LAUREA MAGISTRALE IN
SPACE ENGINEERING - INGEGNERIA SPAZIALE

Author: **Carlo Burattini**

Student ID: 10613747
Advisor: Prof. Camilla Colombo
Co-advisors: Dr. Mirko Trisolini
Academic Year: 2022-23

Abstract

Nowadays, the scientific interest concerning asteroids and their environmental features keeps growing. These bodies provide hints on the primordial Solar System and, not less important, they could represent a valuable source of metals, silicates and water. Several missions, such as Deep Impact (NASA), OSIRIS-REx (NASA), Hayabusa and Hayabusa2 (JAXA), in the past few years were aimed to improve and better identifying the main properties of these yet poorly known celestial bodies. Asteroids, in fact, grant also the possibility to conduct space exploration at reasonable costs, representing therefore the perfect targets for the next space achievements. Within this context, the goal of this work is to assess the feasibility of an in-orbit asteroid samples collection mission, applied in this scenario to the asteroid Ryugu. This will be of huge importance since not only it will prevent any complication related to landing maneuvers, but also it will avoid all the dead times present in a landing mission. According to the Circular Restricted Three-Body dynamics, which considers also the effects of solar radiation and asteroid aspherical potential, particles of different sizes ejecting from different longitudes and with different ejection angles are then classified according to their evolution, finally building a database. In doing this, bouncing behavior is investigated, applying, for each impact angle, restitution coefficients arising from the interpolation of previously available data, analysing the cases of rigid body model and point mass approximation for two different sites on the asteroid. Then, through Hill's equations, trajectories around the second Libration Point L2 are studied, to understand the best possible solution for an orbiting spacecraft. Finally, an aerogel-based collection strategy, already used in Stardust-NExT (NASA), is here studied, initialising a preliminary design for such a collection mechanism.

Keywords: three-body problem, ejecta dynamics, bouncing behavior, Libration point orbits, asteroid sample collection, aerogel capture

Abstract in lingua italiana

Al giorno d'oggi, l'interesse scientifico per gli asteroidi e le loro caratteristiche ambientali continua a crescere. Si ritiene infatti che questi corpi forniscano importanti indizi sul Sistema Solare primordiale e, non meno importante, potrebbero rappresentare una preziosa fonte di metalli, silicati e acqua. Diverse missioni, come Deep Impact (NASA), OSIRIS-REx (NASA), Hayabusa e Hayabusa2 (JAXA), negli ultimi anni hanno portato avanti sforzi volti a identificare meglio le principali caratteristiche di questi corpi celesti ancora poco conosciuti. Gli asteroidi, infatti, garantiscono anche la possibilità di condurre esplorazioni spaziali a costi ragionevoli, rappresentando quindi i bersagli perfetti per le prossime conquiste spaziali. In questo contesto, l'obiettivo del lavoro proposto è quello di valutare la fattibilità di una missione di raccolta di campioni di asteroide rimanendo in orbita, studiando in questo caso l'asteroide Ryugu. Ciò potrebbe essere di grande importanza poiché non solo eviterebbe qualsiasi complicazione legata alle manovre di atterraggio, ma anche tutti i tempi morti presenti in una missione che lo preveda. Secondo la dinamica del Problema dei Tre Corpi Circolare Ristretto, e considerando anche gli effetti della radiazione solare e del potenziale asferico dell'asteroide, particelle di diverse dimensioni espulse da diverse longitudini e con diversi angoli di eiezione sono classificate in base al loro destino, costruendo infine un database. Nel fare ciò, viene indagato il meccanismo di rimbalzo, applicando, per ogni angolo di impatto con Ryugu, coefficienti di restituzione derivanti dall'interpolazione dei dati precedentemente disponibili, sia applicando il modello di corpo rigido sia quello di corpo puntiforme, per due diversi siti sull'asteroide. Quindi, attraverso le equazioni di Hill, vengono trovate e studiate le traiettorie attorno al secondo Punto di Librazione L2, indagando sulla migliore soluzione possibile per un satellite in orbita. Infine, viene studiata una strategia di raccolta basata sull'aerogel, già utilizzata in Stardust-NExT (NASA), inizializzando il design preliminare per tale sistema di raccolta.

Parole chiave: problema dei 3 corpi, dinamica attorno agli asteroidi, meccanismo di rimbalzo, Orbite ai punti lagrangiani, raccolta campioni di asteroide, cattura con aerogel

Contents

Introduction

An asteroid is a rocky body orbiting the Sun as also planets do, but it is much smaller than them. Asteroids are leftovers from the formation of our solar system, which happened about 4.6 billion years ago: some of the condensing dust in the primitive cloud became planets, while part of the material never had the chance to coalesce into planets but rather it formed asteroids.

This origin makes it easy to understand that different asteroids were formed in different moments under a wide variety of conditions, therefore each one presents its own features in terms of shape, dimension, speed, material and orbit, that evolved in time. For example, in the category known as *Apollo asteroids*[1] (see Table 1.1) it is possible to find both the satellites *Didymos* and *Ryugu*: the former is mainly composed of silicates while the latter of carbonaceous rocks, therefore falling into class S and class C respectively (see Chapter 1.2). Both these asteroids are classified as Near Earth Objects (NEO), meaning that they can represent an ideal target for space exploration, since their proximity to Earth allows to plan a ground-controlled mission at a reasonable cost [1]. In fact, Ryugu has been already targeted in the mission Hayabusa2 (JAXA), which successfully touched-down on the asteroid to collect samples of the soil to be analysed on Earth. Such a mission has to deal with small bodies with properties and environments that are mostly unknown or unfamiliar. Their irregular shape, for instance, causes a non-uniform gravitational potential, and this aspect gets worse considering also a non-uniform unknown density and compactness.

Nevertheless, this kind of asteroid exploration mission is crucial to better characterise the physical composition of asteroids, which are rich in valuable resources such as metals, silicates, and water. These could be exploited not only for planning future mining missions but also can be useful for potential In-Situ Resource Utilization (ISRU), such as extraction of water to be used for rocket fuel. Furthermore, asteroid exploration is the key factor to mitigate the impact risk: improving our knowledge, in fact, will lead to increased efficiency of asteroid deflection techniques to enable planetary protection if and when a possible collision is detected. To underline the importance of this, the recent

---

[1]https://scienceworld.wolfram.com/astronomy/ApolloAsteroid.html

NASA's Dart mission proved that it is possible to change the path of an asteroid through an impactor hitting the celestial body.

Moreover, a less practical aspect, but not less important, that pushes towards an active and energetic asteroid exploration, is represented by the sake of knowledge. For what has been previously said, in fact, asteroids are remnants of our early Solar System and likely they carry fundamental information on its evolution: a detailed investigation of their composition provides insight into the origins of life and the formation of the planets. These motivations justify the willingness for detailed asteroid characterization and therefore the development of missions to send a spacecraft to an asteroid [2][3][4].

Thesis objectives

The final goal of this work is to perform a feasibility analysis in view of an on-orbit collection of the ejecta from an asteroid. The collection, in fact, is thought to occur by keeping the satellite on orbit about the second lagrangian point of the Sun-Asteroid system, therefore falling in the domain of the three-body problem. Specifically, this will be investigated considering the third body having a negligible mass when compared with the primaries that, furthermore, are assumed to follow circular paths: these approximations lead to the study of the so-called Circular Restricted Three-Body Problem (CR3BP).

The chosen approach concerns the ejecta energy level: starting from that, it is possible to recover the so-called Zero Velocity Curves (ZVC), which are able to clearly separate zones in the space that are naturally accessible to the ejecta during their motion and the ones that are not: this, in the end, means that for a given energy and position, the ejecta velocity will be uniquely defined as well [2].

Assessing the feasibility of such a collection strategy will imply understanding how many particles will pass through the L2 gap which opens in the ZVC for certain energy levels. The main difficulties, in fact, are to understand if an ejecta particle, once left the asteroid's soil, will escape through the L2 gap, permanently orbit the asteroid itself, or re-impact on it. According to this, each ejecta particle can be classified into five classes, as suggested by Scheeres et al. [5]: in class I the re-impact is immediate, occurring prior to the first periapsis passage; class II features an eventual re-impact after the first periapsis passage; in class III it is possible to find all those ejecta captured into a long-term stable orbit about the asteroid; the ejecta in class IV eventually present at least one periapsis passage before the escape; finally, in class V the escape is immediate, prior to the first periapsis passage. It is easy to understand how most of the ejecta are expected to fall within the first and fifth classes [5].

Furthermore, this study aims to define a reasonable threshold value below which the

collection is said to be non-feasible and, equally important if not more, the amount of time required to collect a sufficient number of items. This last aspect is a key parameter to understanding and assessing the feasibility and the efficiency of a collection mission.

Thesis novelties

The novelties that this work aims to introduce are a few. One of the most important features that this thesis wants to add is to expand the region of interest from just the libration point, as already done by Latino et al. in [1], to a suitable halo orbit around it. This will return a more realistic and useful point of view on the portion of space where the ejecta can be captured. Moreover, this will increase the area of interest, likely leading to more ejecta transits at the same time, finally increasing the feasibility of this collection strategy. The second contribution is to perform a preliminary design of the satellite in the Halo orbit around the libration point. In particular, a study on the possible capturing mechanisms will be performed. As stated by Zhai et al. [6], for this kind of operation a flexible capture is preferred with respect to a rigid system. Contrarily, a robotic-based on-orbit service (OOS), implies an attitude disturbance to the satellite's base caused by the physical interception between the robot and the target object, as reported by Flores-Abad et al. [7].

However, both these techniques are not suitable for the capture of multiple particles having also a wide size range. The most adapt capture mechanism is found to be based on aerogel, a novel material developed in the past few years. Aerogel has been already used for the Stardust-NeXT mission (NASA), which therefore will be used as a guide to take the first steps of the capture preliminary design.

Thesis outcomes

The outcomes of this thesis will be crucial to push forward and better understand the technology and the tools required to perform an efficient asteroid exploration. This work in fact will understand the behavior of halo orbits and where to put the satellite and will better identify the requirements of the aerogel collection system.

Moreover, assessing the feasibility of an on-orbit collection of asteroid samples will lead to the complete removal of the closing maneuver needed to land on the soil, which, in the case of on-orbit capture, will be unnecessary. This is a pivotal aspect since it not only mitigates the risk related to the landing phases but also avoids the dead times that in a landing-mission will be present. Considering again the case of the mission Hayabusa2, in fact, since each operation starts and finishes with the satellite at Home Position, it is

required, in order to grant a safe landing of the spacecraft, to wait for the dissipation of the generated ejecta plume around the asteroid ($\sim$ 2 weeks for 1 mm size particles) [8]. Overall, the aim here is to increase our knowledge and experience with these celestial bodies: being able to complete the program of this work, apart from its intrinsic goal, would make the asteroid's environment more familiar, moving closer to the prospects introduced until now.

Thesis outline

The thesis is organised as described in the following lines. In Chapter 1, a brief summary of asteroid's distribution and main properties are reported. Then, a recap of the main missions performing samples collection of asteroids and comets. Within these, Hayabusa2 will be the most investigated since, as clarified later on, Ryugu is the target of the mission proposed. Chapter 2, instead, introduces the Circular Restricted Three-Body Problem, at first in sidereal frame but then expressed in the synodic one, to be then reformulated as adimensional. The Jacobi Constant and the Lagrangian points are then introduced, and their behavior with respect to the perturbations considered, i.e. asteroid's aspherical potential and solar radiation, will be analyzed. In this chapter, also the recovery of the so-called Hill's problem, useful to study the periodic orbits around libration points, is exposed. In Chapter 3 the actual work starts. Here, in fact, the procedure to obtain a database reporting the final fate of the ejecta dependently on their initial conditions, is presented. Specifically, after discussing how to recover the ejection conditions, this chapter explains how the restitution coefficients are found, which category are defined and what are the ranges considered for the longitude, ejection angle and size for an ejecting particle. In Chapter 4 takes place the dissertation regarding the periodic orbits around L2. After introducing the families of orbits, the chapter will introduce the differential corrections and the continuation method used to recover those families. Finally, the trajectories in the neck region are recovered for two different scenarios. In Chapter 5 the post-processing of the work is carried on, analysing the results obtained, i.e. trends, behaviors and the amount of particles that fall back on Ryugu, orbit it or leave its system., and establishing a threshold to recover the minimum amount of time required to consider the collection feasible. This, of course, will consider just the time spent in the asteroid's system, without taking into account the duration of the travel to reach the target. Chapter 6, instead, deals with the identification of the best possible technique with which actually perform the capture. This is found out to be an aerogel based mechanism, for which, a preliminary design is carried on, approximating the dimensions needed and defining the main first requirements involving the main sub-systems. Finally, in Chapter 7 the work is briefly

summarised, underlining the principal outcomes of the work proposed.

1 | Literature review

In this chapter, the asteroids' main features will be introduced, in terms of orbital characteristics, and therefore their distribution within the Solar System; and in terms of physical features, which are size, mass, shape, rotation rate and spin axis. Furthermore, this section will also analyze the techniques used to model the shape of an asteroid, a task which becomes crucial to recover the gravitational field of the body and therefore to understand the dynamics of the ejecta moving around it. Finally, a brief summary of past missions concerning asteroid exploration will be presented. Specifically, JAXA's missions Hayabusa and Hayabusa2 will be here reviewed more in detail, particularly highlighting the aspects that this last mission revealed about Ryugu, since it will represent the target of this work.

1.1.   Asteroids distribution within the Solar System

Asteroids form a large and scattered group of Sun-orbiting bodies. The oldest and the vast majority of them rotate around the Sun between the orbits of Mars and Jupiter, in the so-called *Asteroid Belt*, with distances of 2.2-3.5 AU from the star, generally in relatively low-eccentricity orbits. Asteroids in this region range in size from Vesta, with 530 kilometers of diameter, to bodies that are less than 10 meters across. The total mass of all the bodies belonging to the asteroid belt is less than that of Earth's Moon: the most likely value on the total mass of the asteroid belt is estimated to be ~ 2440 kg, which is only about 4% of the mass of the Moon. The four largest objects, Ceres, Vesta, Pallas, and Hygiea, account for approximately 62% of the belt's total mass, with 25% accounted for by Ceres alone. All these data can be easily found on NASA's website, highlighting how this belt represents the oldest and most studied group of asteroids and therefore, in general, they represent the best-known category when compared with other asteroid groups.

At the end of 2016 there were more than 750.000 cataloged asteroids, a number that is currently increasing by thousands every month: to give an idea, the belt is now estimated to contain between 1.1 and 1.9 million asteroids larger than 1 km in diameter, and millions

of smaller ones. These asteroids probably were formed simultaneously with the major planets from the protoplanetary disk, but in this region, the accretion of planetesimals into planets was prevented by large gravitational perturbations imposed by Jupiter.

Despite what has been said, the main belt is mostly empty since the asteroids are spread over such a large volume that reaching an asteroid without aiming carefully would be improbable: therefore there is no worry about space probes hitting an asteroid on their way to the outer Solar System but, contrarily, to get even close to an asteroid takes a great deal of effort [9].

Another main group of asteroids takes the name of *Trojans*. A trojan is an asteroid that shares the orbit of a larger body, remaining in a stable orbit approximately 60° ahead or behind the main body near one of its Lagrangian points L4 and L5. In the Solar System, most known trojans share the orbit of Jupiter and are divided into the *Greek camp* and *Trojan camp*: the former is at L4 (ahead of Jupiter), and the latter is at L5 (trailing Jupiter). More than a million Jupiter trojans larger than one kilometer are thought to exist, especially in the Trojan camp, which is the most numerous.

Finally, the most interesting class of asteroids is represented by the *Near Earth Asteroids (NEAs)*. These bodies have orbits that pass close to that of Earth, having a semi-major axis smaller than 1.3 AU. Sometimes, they can take the name of *Earth-crossers* in all those cases in which the asteroid's trajectory crosses Earth's orbital path. A small number of NEAs are actually extinct comets, while the rest, the bigger part, are asteroids driven out of the main belt by gravitational interactions with Jupiter. Depending on their semi-major axis (a), perihelion (r_p) and aphelion distances (r_a), NEAs are classified as stated in Table 1.1[1].

Class	Description	Parameters
Atiras	Orbits strictly inside Earth's orbit	$a < 1$ AU; $r_a < 0.983$ AU
Atens	Earth-crossers with SMA smaller than 1AU	$a < 1$ AU; $r_a > 0.983$ AU
Apollos	Earth-crossers with SMA bigger than 1AU	$a > 1$ AU; $r_p < 1.017$ AU
Amors	Orbits strictly outside Earth's orbit	$a > 1$ AU; $1.017 < r_p < 1.3$ AU

Table 1.1: NEAs classification.

In addition to this classification, another distinction can be done on the so-called Potentially Hazardous Asteroids (PHAs). These bodies are near-Earth objects with trajectories presenting close approaches to Earth and, simultaneously, large enough to cause significant damage if an impact occurs. The key parameter is the Minimum Orbit Intersection

---

[1]Credits: NASA NEO Groups.

Distance (MOID) with Earth that, for PHAs, is less than 0.05 AU [1].

Although potentially dangerous for Earth, as aforementioned, their proximity to the planet allows planning missions at a low cost, meaning that NEAs represent an ideal target for space exploration. This aspect has been particularly well highlighted by Turconi [10], from which Figure 1.1 comes.
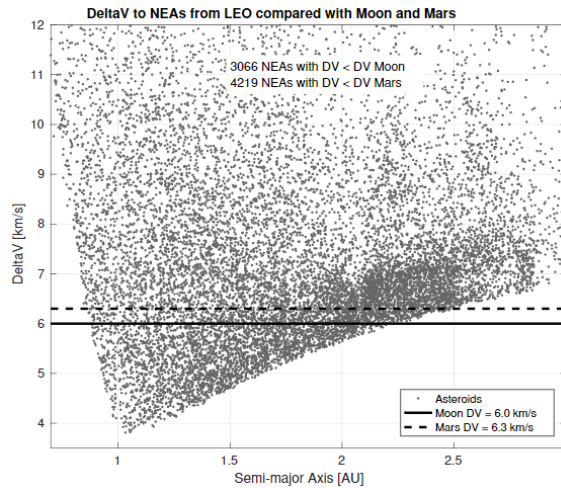

Figure 1.1: ΔV from LEO to closest NEAs, compared to the Moon and Mars [10]

Finally, a clear vision of the distribution of the asteroids within the Solar System is reported in Figure 1.2.
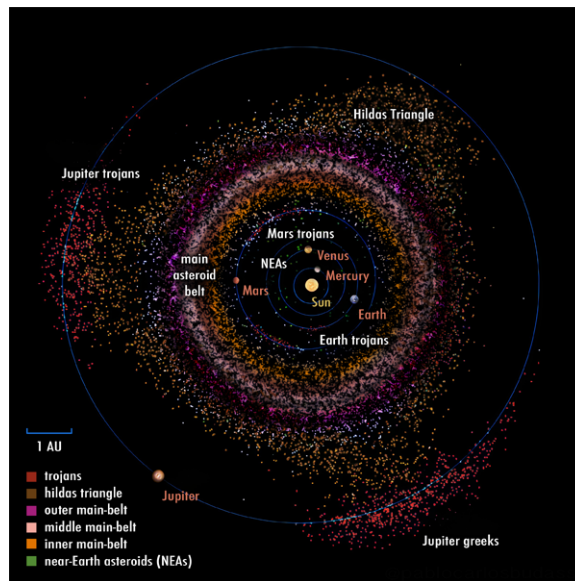
Figure 1.2: Distribution of asteroids within our Solar System. Credits: Pablo Carlos Budassi.

1.2.   Asteroids physical characteristics

Despite knowing the orbital parameters of thousands of asteroids, only for a few tens of them the masses are also known. The only way to accurately estimate their masses is to evaluate the effects of their perturbations on other objects thanks to observations. This method, even though does not depend on the angle between the orbital plane and the line of sight, can be considered a valid approach only for the most massive asteroids, otherwise the disturbing action would be too small. Nowadays, thanks to more accurate telescopes, interferometry and star occultations (or transit) have become the best methods to determine the asteroids' shapes and dimensions. Actually, the most precise results are obtained through spacecraft flybys, which is clearly not feasible for all existing asteroids. Regarding asteroids' size, also this varies greatly for each asteroid, from almost 1000 km for the largest down to rocks just 1 meter across. The biggest asteroids are very much like miniature planets: they are roughly spherical, have at least partly differentiated interiors and are thought to be surviving protoplanets. The vast majority, however, is much smaller and irregularly shaped.

Concerning asteroids' rotation, the spin is usually about the axis of their maximum moment of inertia, which is stable and it offers the minimum energy for a rotating body. The rotation rates, instead, are typically of the order of some hours. This, as reported by Johansson et al. [11], is related to the diameter of the asteroid itself. As shown in Figure 1.3, in fact, the rotation period T_{rot} shows a remarkably sharp cutoff which lies very close to 2 hours for asteroids with diameters bigger than ~ 150 m. Shorter periods are associated with diameters smaller than 0.5 km. This is because most of the asteroids are composed of material kept together by gravity rather than by cohesive bonds; then, to rotate faster, the small body is forced to split into binary asteroids. In agreement with this, in the same figure can be seen how smaller asteroids can rotate faster but are relatively rarer. Of course, it must be underlined that smaller bodies are also more difficult to detect and study, then this information could be partial or suffering by this bias.

Concerning instead the composition, which is widely differentiated and in most cases poorly understood, asteroids can be classified by their characteristic emission spectra. The majority falls into the C-type, X-type, or S-type classes, being mainly composed of carbon, metals, or silicates respectively. Within the X-type class, it is possible to further distinguish, according to their albedo, between P-type (the darkest), M-type and E-type (the brightest), as already described by Tholen's classification in 1984 [12]. The modern classification takes the name of *Small Main-Belt Asteroid Spectroscopic Survey (SMASS)*: this includes several smaller classes, ending up defining 24 different types of
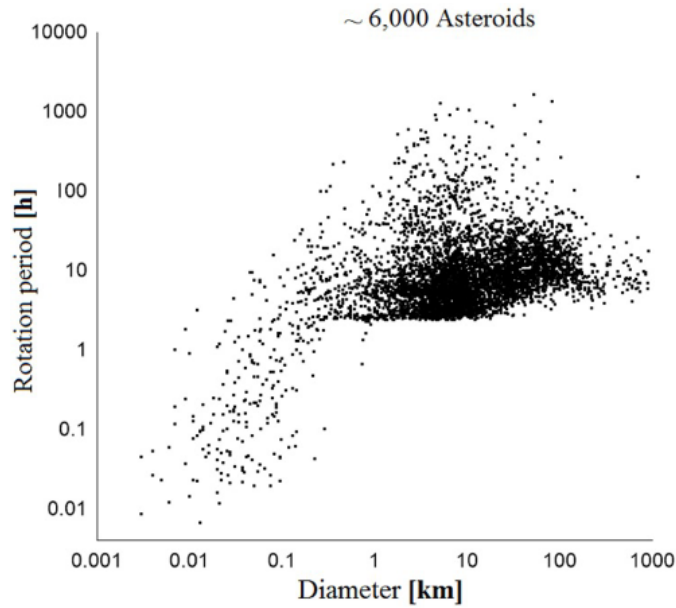
Figure 1.3: Asteroids' rotation period vs size [11]

asteroids. However, a deep discussion about the different classes of asteroids is outside the aim of this work therefore, if interested, please refer to [13], which provides also the clear plot shown in Figure 1.4: this reports asteroids' mass as function of their density, distinguishing between six different taxonomic groups. The figure shows how these bodies lay around a mass value equal to 10^{19} kg, having larger dimensions for lower densities.
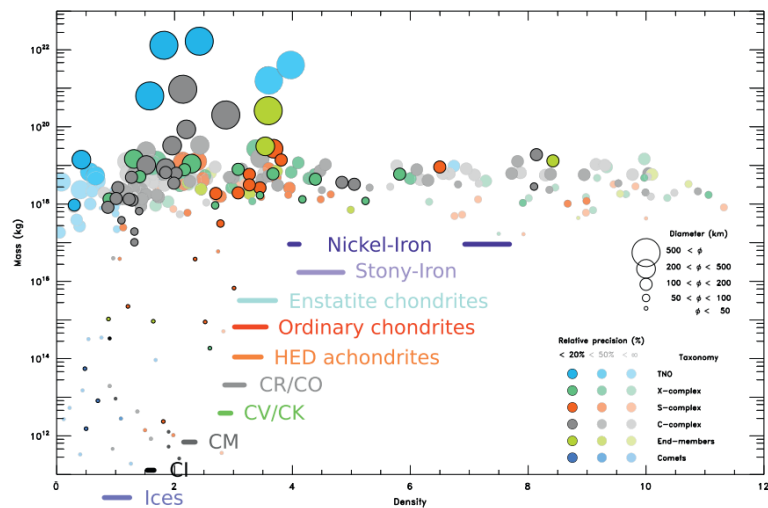

Figure 1.4: Density vs Mass for different taxonomic groups. Bodies with unknown taxonomy are plotted in black [13].

1.2.1.   How to model asteroids' shape to recover the gravity field

Maintaining missions in the proximity of small bodies requires extensive orbit determination, which implies the use of more and more accurate models to approximate the shape of an asteroid, to finally recover its gravity field. The most used techniques nowadays are [14][5][10]:

- The tri-axial ellipsoid;

- The mascons model (multi-point mass);

- The polyhedral model.

The first approximates the shape of the asteroid with a simple geometric body. It is useful for situations when a precise model of the gravity field is not needed, since it is obvious that a basic geometric shape cannot describe the irregular surface of the asteroid, which shows also asymmetries. Its advantages are that it is relatively simple to code and does not present singularities.

The representation of a body with mascons, instead, compromises simplicity with adequate fidelity. Assuming that observations can provide a good representation of the asteroid's surface, this method fills entirely its volume with non-overlapping spheres, each one with a particular mass density and size assigned to it. This approach can lead to regions of poor gravity field computation on the surface and it is inefficient if a high resolution is desired. Nevertheless, with this model, a *Shape Continuation Method (SCM)* can be applied [15]. This method refers to the sequential approximation of the potential of an asteroid, adding at each step one or more mascons to the simpler starting shape, which is usually an ellipsoid.

Last, with the polyhedral model, the overall efficiency is usually higher than in the previous method, since this approach must only sum over the surface elements of the body, rather than over the overall volume as in the mascons technique. This model also has the advantage of giving a direct indication of whether the point is inside or outside the asteroid. However, a large number of elements are required for an accurate field recovery, thus increase of computational demand could represent a limit .

1.3.   Asteroid exploration review

In this section, a review of past asteroid exploration missions is carried on. In particular, the main focus will be on missions that performed impact with asteroid or sample collection landing on it rather than missions that have "just" performed a flyby or an imaging study. This choice comes out directly from the purpose of this work.

For all the followings, the main sources come directly from the mission agency's website.

1.3.1. Deep Impact (NASA)

Deep Impact is a NASA Discovery Mission and represents the first space mission to search beneath the surface of a comet, trying to reveal the secrets of its interior. The target chosen for its objective was the comet Tempel1, which takes the name from its first discovery attributed to Ernst Tempel in 1867. The comet represented a well-known subject that had made many passages through the inner solar system, orbiting the Sun every 5.5 years. This aspect makes Tempel1 a good target to study the evolutionary change in the mantle or upper crust.

The mission involved a two-part spacecraft: a projectile body of about 370 kg and a fly-by probe. After 174 days from departure, which happened on January 12th, 2005, the spacecraft reached its target. On July 3rd, the separation between the two parts occurred. The projectile impacted with the comet's sunlit side surface only 24 hours later, releasing $\sim 1.96 \cdot 10^{10}$ J of kinetic energy, equivalent to 4.5 tons of TNT: the so-formed crater presented about 200 m of diameter and a depth of 30-50m but, anyway, this was not enough to cause an appreciable change in the comet's orbital path around the Sun. After the release of the impactor, the flyby spacecraft maneuvered to a new path featuring a closest approach from the comet of about 500 km. This enabled the spacecraft to observe and record the impact, the ejected material blasted from the crater, and the structure and composition of the crater's interior. Astronomers, helped with data from Deep Impact, came up with a list of compounds thought to be the recipe for planets, comets and other bodies in the solar system. These include silicates, or sand, clay, carbonates, iron-bearing compounds and even aromatic hydrocarbons. Finally, in February 2006, Deep Impact team was able to discover water ice on comet Tempel1, marking the complete success of the mission.

1.3.2. Stardust-NExT (NASA)

Stardust-NExT is a low-cost mission that aimed to expand the investigation of comet Tempel1 initiated by NASA's Deep Impact mission herein-above. Launched on February 7th, 1999, the probe successfully collected samples and fragments of the comet Wild2, before arriving at Tempel1 on February 14th, 2011. En route to Wild2, the spacecraft flew past asteroid 5535 Annefrank in 2002, where it performed a flyby at very high speed. This was enough to derive an estimation of the asteroid's shape and albedo. On the contrary, due to the short time window, the spacecraft could not estimate the rotation rate of the body. This was consistent with the very slow rotation period supposedly owned
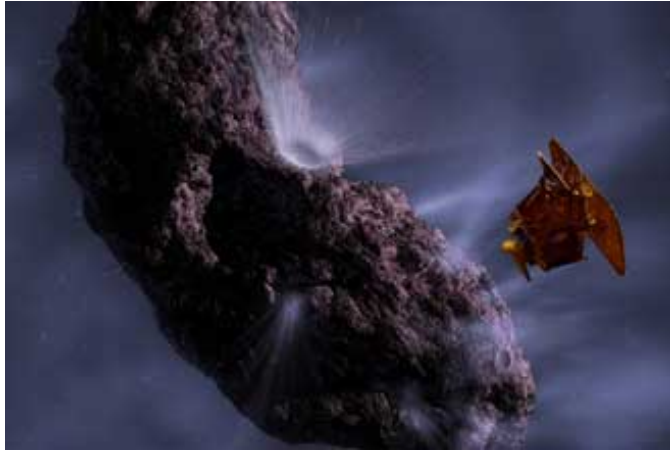
Figure 1.5: Artist's concept of Deep Impact. Credits: NASA

by the body.

On March 24th, 2011, the mission ended since all the propellant was consumed. The gathered material was therefore sent by means of a special capsule back to Earth, where it landed on January 15th, 2006. The main novelties of this mission regarded the technique exploited for the collection: Stardust in fact used a special low-density aerogel where fragments remained stuck. This approach is perfectly suitable also for the kind of on-orbit capture studied in this thesis, and therefore will be later examined in more details (see Chapter 6).

1.3.3. OSIRIS-REx (NASA)

OSIRIS-REx (Origins, Spectral Interpretation, Resource Identification, Security, Regolith Explorer) is NASA's first asteroid sample return mission. The mission was designed with the aim of collecting at least 60g of soil samples from the asteroid 101955 Bennu, an apollo asteroid of type B, and returning them on Earth for detailed analysis. The selection of Bennu as the target body is made possible by the regular encounters of the asteroid with the Earth. Moreover, the similarity of their orbits, it is responsible for a higher collision probability by the end of the 22nd century, increasing the interest regarding this celestial object.

NASA launched OSIRIS-REx on September 8th, 2016 and it arrived at Bennu in December 2018. After this, the spacecraft surveyed the asteroid for more than two years in order to observe Bennu and, on October 20th, 2020 it landed to collect samples, stowing them in its sample return capsule. The re-entry of the gathered material on Earth is thought to occur during 2023 but this represents one of the most critical tasks. The delivery itself, in fact, is not simple: OSIRIS-REx must approach Earth at a precise speed and direction
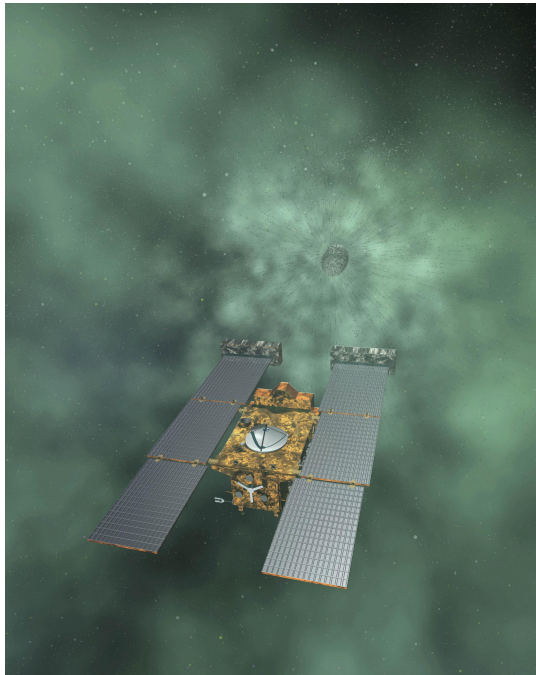
Figure 1.6: Artist concept of NASA's Stardust-NExT mission. Credits: NASA/JPL-Caltech/LMSS.

to deliver its sample return capsule into Earth's atmosphere. If the capsule is angled too high, it will skip off the atmosphere, and contrarily, if angled too low it will burn up in Earth's atmosphere. For this reason, OSIRIS-REx team changed the spacecraft's trajectory since it left Bennu on May 10th, 2021. Following this course adjustment as well as a series of maneuvers planned for July 2023, the spacecraft will arrive at altitude of about 250 km from Earth's surface, close enough to release the capsule for a precise parachute landing.

.

1.3.4. Hayabusa (JAXA)

The Japanese mission was the first asteroid sample-return mission ever attempted, aiming to experimentally research new engineering technologies necessary for returning planetary samples to Earth. The mission's target was the asteroid *Itokawa*, a strange peanut-shaped S-type asteroid with a rubble-pile structure. The launch was performed on May 9, 2003, and, after a swing-by of the Earth in May 2004, it reached the celestial body on September 12, 2005, after traveling about 2 billion kilometers. After rendezvoused with Itokawa, Hayabusa studied the asteroid's shape, spin, topography, color, composition and density by means of remote-sensing techniques such as high-resolution imaging and
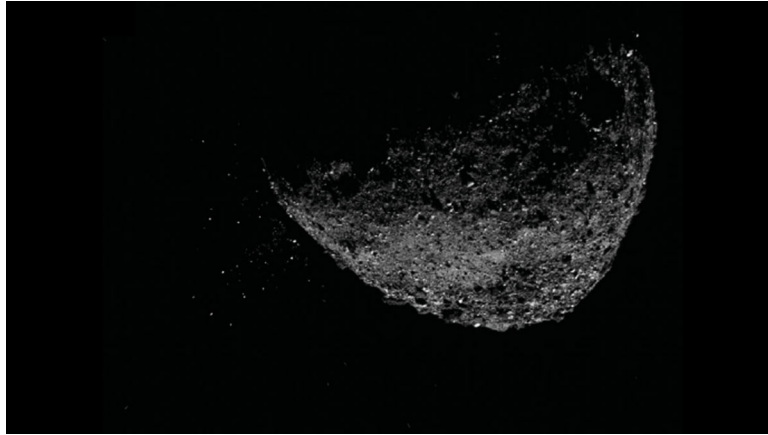
Figure 1.7: Asteroid Bennu ejected particles from its surface on Jan. 6, 2019, as seen by NavCam1 imager aboard NASA's OSIRIS-REx spacecraft. Credits: NASA/Goddard/University of Arizona/Lockheed Martin.

LIDAR sensing. This first phase ended in October of the same year. Due to the extremely weak gravitational pull of the small body and non-negligible Solar Radiation Pressure disturbance, the spacecraft actually did not achieve a proper orbit about the asteroid but rather was forced to use a hovering approach exploiting its thrusters to perform an active control, keeping the desired position with respect to Itokawa. Nevertheless, in November 2005, the probe successfully landed twice on the asteroid to collect samples in the form of tiny grains of material, which returned to Earth aboard the spacecraft on 13 June 2010. The results of the mission were then published in a special edition of the U.S. scientific journal "Science", marking the first successful sample return from an asteroid.
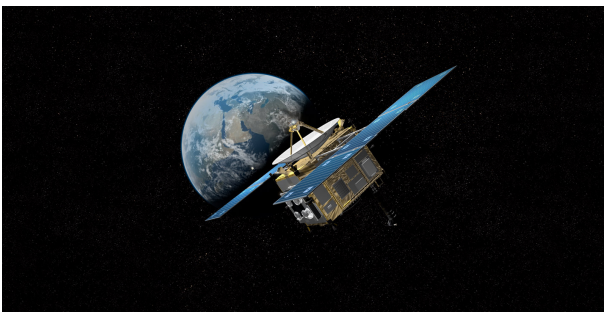
Figure 1.8: Rendering of Hayabusa
Credits: JAXA website
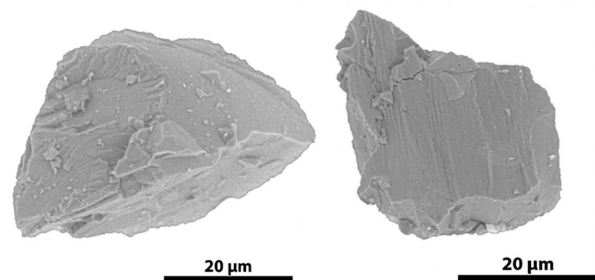
Figure 1.9: Two Itokawa's samples
Credits: JAXA website

1.3.5. Hayabusa2 (JAXA)

This sequel mission, Hayabusa2 (Figure 1.10), aimed to investigate *Ryugu*, an asteroid that follows an orbit with an eccentricity of 0.19 and an inclination of 6° with respect to the ecliptic.

Ryugu is a different type of asteroid with respect to Itokawa, being a type C asteroid. The experience gained with the previous mission has been exploited here: Hayabusa2, in fact, followed the same method performed by the first Hayabusa mission, exploiting a hovering approach to match the trajectory of the small body orbiting around the Sun rather than the asteroid itself. The selection of the target asteroid was driven by the belief that the composition of C-type asteroids still includes organic matter and water from when the Solar System was forming. Moreover, this mission wanted to investigate the origin of the Earth's water and the origin of the organic matter that initially formed life. A further aspect was to examine how the planets were formed through the collision, destruction, and combination of planetesimals. *"In short* - as declared by JAXA itself on its website - *Hayabusa2 is a mission designed to elucidate the creation of life and the birth of the Solar System"*.

The main payloads based on remote sensing operations were:

- The Optical Navigation Cameras (ONCs), used for navigation and proximity operation, as well as to search for interplanetary dust around the asteroid;

- The LIght Detection And Ranging (LIDAR) altimeter, which, scanning the distance between the spacecraft and the asteroid's soil, determined in detail the dimensions and shape of Ryugu.

However, Hayabusa2 carried and deployed many other payloads, such as Rover-1A (HI-BOU) and Rover-1B (OWL) that landed on the asteroid providing the world's first photograph from the surface of an asteroid; and the Mobile Asteroid Surface Scout (MASCOT) which included an infrared spectrometer, a magnetometer, a radiometer and a camera able to image the small-scale structure of regolith material. A further payload, actually one of the most important, was the *SmallCarry-on Impactor (SCI)*, consisting of a 2.5 kg copper projectile shot to the surface by an explosive propellant charge (Figure 1.11). It was used to excavate a crater revealing the inner layers of the asteroid.

The probe arrived at Ryugu on June 27, 2018, collected samples from the asteroid during two touchdowns in 2019, and finally delivered the sample capsule back to the Earth on December 6, 2020.
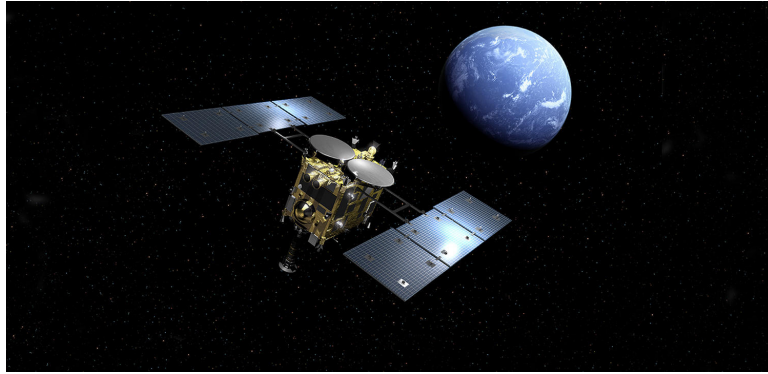
Figure 1.10: Rendering of Hayabusa2
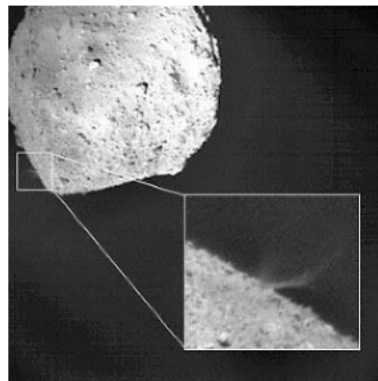Credits: JAXA website

Figure 1.11: Photo of the impact of the SCI with Ryugu's surface. Credits: JAXA website

Hayabusa2 results

The samples gathered were stored in two different chambers. Chamber A stored the samples collected during the first touch-down sampling, for a total of 3.237 ± 0.002 g of material. This was assumed to represent the surface material of Ryugu at the uppermost centimeter-scale layer, which is the one more influenced by Sun, radiations, temperature cycling and micrometeoritic impacts. Chamber C, instead, picked up the samples during the second touch-down sampling, collecting 2.025 ± 0.003 g. The second touchdown was close to the artificial crater excavated by the SCI and therefore these samples are assumed to be representative of subsurface materials, that have not experienced long-term exposure to space [16].

The samples obtained have sizes ranging from ~ 8 mm, the largest average diameter, down to fine sub-millimeter dust, with millimeter-scale particles being the most common. Figure 1.12 shows the size distribution of the collected material for both chambers.

Figure 1.12 highlights a power index for chamber A+C steeper than the global average
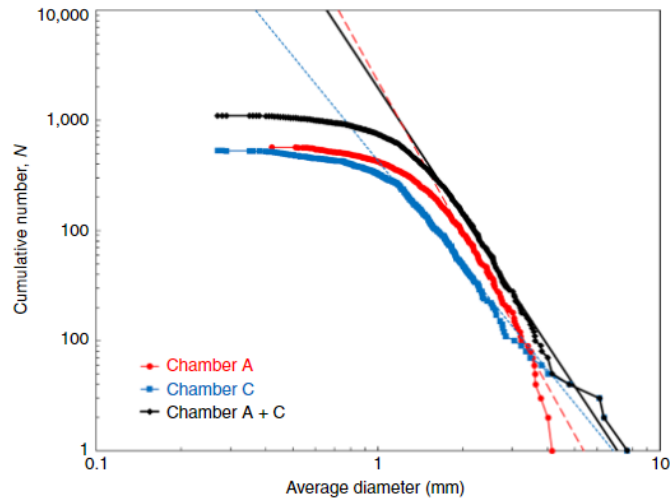
Figure 1.12: Size distributions of Ryugu's particles [16].

index observed by the ONCs, underlining a higher relative abundance of the smaller particles [16]. There are several possible interpretations for this, among which a further fragmentation during sampling impacts or the shocks and vibrations experienced during Earth re-entry are the more convincing ones.

Concluding, all the features examined indicate that Ryugu is most similar to C1 chondrites[2] but have a lower albedo, higher porosity and more fragile characteristics. However, for further clarifications and details, if interested please refer to [16].

Table 1.2 summarises the main properties of Ryugu [8][16][17].

Property	Value
Rotational Period	$7.631h$
Orbital Period	$1.3years$
Effective Radius	$440m$
Ellipsoid Axis	$a = 446.5m; b = 439.7m; c = 433.9m$
μ_a	$32m^3/s^2$
Density (Bulk)	$1282kg/m^3$
Mass	$(4.50 \pm 0.06) \cdot 10^{11}kg$

Table 1.2: Main properties of Ryugu.

---

[2]C1 chondrites are a group of rare carbonaceous chondrite, a type of stony meteorite. They are rich in volatiles-water, organics, and other light elements/compounds.

2 | Dynamical model and equations

Being involved in the study of a Sun-Asteroid system implies, of course, that this work is inserted in the context of the so-called *Three-Body Problem*. A spacecraft, therefore, will be subjected to the gravitational attraction of the two primaries, which move along their orbits around the system's barycentre by virtue of their mutual attraction. Moreover, indicating with m_s, m_a and $m_{S/C}$ the masses of Sun, asteroid and spacecraft respectively, it will hold that $m_s > m_a >> m_{S/C}$: this means that the third body can be considered as a "mass-less" object that cannot affect the motion of the other bodies of the system. With this consideration, and assuming also that the primaries follow circular paths, it is possible to reduce the problem to the so-called *Circular Restricted Three Body Problem (CR3BP)*, whose equations of motion are :

$$\ddot{\boldsymbol{r}} = \frac{\mu_1}{|\boldsymbol{A} - \boldsymbol{r}|^3}(\boldsymbol{A} - \boldsymbol{r}) + \frac{\mu_2}{|\boldsymbol{B} - \boldsymbol{r}|^3}(\boldsymbol{B} - \boldsymbol{r}) \tag{2.1}$$

In the previous equation, centered in the system's center of mass, μ_i represents the gravitational constant of the i_{th} body ($i = 1$ for the biggest primary, $i = 2$ for the smallest), A is the distance from the origin to the biggest primary, B is the distance from the origin to the smallest primary and $\boldsymbol{r}$ is the position vector of the third body. In particular, A and B can be expressed as follow:

$$\begin{cases} A = A(t) = -A\cos(\omega t)\boldsymbol{i} - A\sin(\omega t)\boldsymbol{j} \\ B = B(t) = B\cos(\omega t)\boldsymbol{i} + A\sin(\omega t)\boldsymbol{j} \end{cases} \tag{2.2}$$

In Equation 2.2, ω is the rotational velocity of the system around its barycentre, which coincides with the origin of the system, while $\boldsymbol{i}$ and $\boldsymbol{j}$ are the axis of the so-called sidereal frame. This frame is fixed in space, leading therefore to the description of non-autonomous systems. As a consequence of this, in fact, in Equation 2.2 the time appears as an inde-

pendent variable.

2.1.   From sidereal to the synodic reference frame

Nevertheless, in the study of the CR3BP, it is much more convenient to work with autonomous systems, which are all those systems that do not depend explicitly on time. The biggest advantage arising from this is that all the features investigated and studied within this context will be valid at any time instant. Basically, the aim here is to transform the description of the problem from $\dot{\boldsymbol{x}} = \boldsymbol{f}(\boldsymbol{x}, t)$ to $\dot{\boldsymbol{x}} = \boldsymbol{f}(\boldsymbol{x})$, deleting the explicit time-dependence. In the previous expressions, $\boldsymbol{x}$ is the vector containing the states of the problem. In this case, the motion of the third "mass-less" body, i.e. the spacecraft, can be completely described through its position and velocity, meaning that $\dot{\boldsymbol{x}}$ can be expressed as stated in Equation 2.3.

$$\boldsymbol{x} = \begin{bmatrix} x \\ y \\ z \\ \dot{x} \\ \dot{y} \\ \dot{z} \end{bmatrix} \implies \dot{\boldsymbol{x}} = \begin{bmatrix} \dot{x} \\ \dot{y} \\ \dot{z} \\ \ddot{x} \\ \ddot{y} \\ \ddot{z} \end{bmatrix} \tag{2.3}$$

To reach this goal, it is possible to pass from an inertial frame, the sidereal one, to the so-called synodic frame. This frame rotates in the x-y plane with the same angular rate as the system, with the outcome that the position of the two primaries remains fixed with respect to the origin, located at the system's barycenter. Identifying as $\{\hat{\boldsymbol{i}}, \hat{\boldsymbol{j}}, \hat{\boldsymbol{k}}\}$ the base of this new rotating system, the absolute velocity can be expressed as follow [18]:

$$\boldsymbol{v} = \frac{d\boldsymbol{r}}{dt} = \dot{x}\hat{\boldsymbol{i}} + x\frac{d\hat{\boldsymbol{i}}}{dt} + \dot{y}\hat{\boldsymbol{j}} + y\frac{d\hat{\boldsymbol{j}}}{dt} + \dot{z}\hat{\boldsymbol{k}} = \dot{x}\hat{\boldsymbol{i}} + \dot{y}\hat{\boldsymbol{j}} + \dot{z}\hat{\boldsymbol{k}} + \left(x\frac{d\hat{\boldsymbol{i}}}{dt} + y\frac{d\hat{\boldsymbol{j}}}{dt} \right) \tag{2.4}$$

Defining now a vector $\boldsymbol{\Omega}$=[0 0 ω], Equation 2.4 can be modified into

$$\boldsymbol{v} = \frac{\delta\boldsymbol{r}}{dt} + (\boldsymbol{\Omega} \times \boldsymbol{r}) \tag{2.5}$$

Deriving again in time Equation 2.5 it is possible to recover the absolute acceleration, expressed as reported in Equation 2.6.

$$\boldsymbol{a} = \frac{d\boldsymbol{v}}{dt} = \frac{\delta\boldsymbol{v}}{\delta t} + (\boldsymbol{\Omega} \times \boldsymbol{v}) = \frac{\delta^2\boldsymbol{r}}{\delta t^2} + (\dot{\boldsymbol{\Omega}} \times \boldsymbol{r}) + 2\boldsymbol{\Omega} \times \frac{\delta\boldsymbol{r}}{\delta t} + \boldsymbol{\Omega} \times (\boldsymbol{\Omega} \times \boldsymbol{r}) \qquad (2.6)$$

For the *circular* problem, however, $\dot{\boldsymbol{\Omega}} = 0$, therefore the second term of the right-hand side of Equation 2.6 vanishes.

It can be noticed that, up to now, the discussion regarded just mechanical transformations. The CR3BP dynamics is introduced only now, using the definition of the gravitational forces acting on the third body. Exploiting a new variable μ, defined in Equation 2.7, it is possible to write the gravitational force as expressed in Equation 2.8.

$$\mu = \frac{m_2}{m_1 + m_2} \qquad (2.7)$$

$$\boldsymbol{F} = -G\frac{m_1 m_{S/C}}{r_1^3}\boldsymbol{r_1} - G\frac{m_2 m_{S/C}}{r_2^3}\boldsymbol{r_2} \qquad (2.8)$$

In Equation 2.8, G is the universal gravitational constant while, calling R the distance between the two primaries, r_1 and r_2 can be found as stated in the following expressions:

$$\boldsymbol{r_1} = (x + \mu R)\hat{\boldsymbol{i}} + y\hat{\boldsymbol{j}} + z\hat{\boldsymbol{k}} \qquad (2.9)$$

$$\boldsymbol{r_2} = (x + (\mu - 1)R)\hat{\boldsymbol{i}} + y\hat{\boldsymbol{j}} + z\hat{\boldsymbol{k}} \qquad (2.10)$$

From the second law of dynamics, however, it is known that $\boldsymbol{a} = \boldsymbol{F}/m$ therefore, equating Equation 2.6 to Equation 2.8 divided by $m_{S/C}$, it is possible to obtain the equations of motion for the CR3BP expressed in the synodic frame (Equation 2.11).

$$\frac{\delta^2\boldsymbol{r}}{\delta t^2} = -G\left(\frac{m_1}{r_1^3}\boldsymbol{r_1} + \frac{m_2}{r_2^3}\boldsymbol{r_2}\right) - \boldsymbol{\Omega} \times (\boldsymbol{\Omega} \times \boldsymbol{r}) - 2\boldsymbol{\Omega} \times \frac{\delta\boldsymbol{r}}{\delta t} \qquad (2.11)$$

At this point, it is useful to define the potential energy of the system. In particular, starting from the gravitational contribution (Equation 2.12) and the rotational one (Equation 2.13), it is possible to recover the total potential energy of the three-body problem as reported in Equation 2.14.

$$U_{grav} = -G\left(\frac{m_1}{r_1} + \frac{m_2}{r_2}\right) \qquad (2.12)$$

$$U_{rot} = -\frac{1}{2}\Omega^2(x^2 + y^2)$$ (2.13)

$$U = U_{grav} + U_{pot} = -G\left(\frac{m_1}{r_1} + \frac{m_2}{r_2}\right) - \frac{1}{2}\Omega^2(x^2 + y^2)$$ (2.14)

It can be shown that the gradient of U is equal to the first two terms of the right-hand side of Equation 2.11, therefore the equations of motion become:

$$\frac{\delta^2 \boldsymbol{r}}{\delta t^2} = -\nabla U - 2\boldsymbol{\Omega} \times \frac{\delta \boldsymbol{r}}{\delta t}$$ (2.15)

The dynamics expressed in this is useful to reveal information otherwise hidden. For example, such a dissertation is able to drive to the definition of an integral of motion, the so-called *Jacobi constant*, and the identification of five equilibrium points in space, the *Lagrangian points*. These arguments will be discussed in sections 2.3 and 2.4.

2.2.   Adimensional equations of motion

The equations of motion in the synodic frame were already introduced with Equation 2.11. However, what is typically done is to adimensionalise the problem, transforming it in order to work with non-dimensional quantities. This leads to the advantage of dealing with more familiar numbers, as well as improving the efficiency and accuracy of computational and numerical methods applied to study the problem. To make Equation 2.11 adimensional, a proper choice of the reference length, mass and time must be done. Usually [19]:

- the reference mass is chosen equal to $M_{ref} = m_1 + m_2$;

- the most natural choice for the reference length is represented by the distance between the two primaries, called R in Equations 2.9 and 2.10;

- the chosen time unit τ is such that the frequency of the system is 2π, driving to an unit angular rate ($\Omega = 1$).

These considerations will also fix the numerical value of G to one, as demonstrated in with the following expression [1]:

$$\Omega = 1 = \sqrt{\frac{G(m_1 + m_2)}{R^3}} = \sqrt{\frac{GM_{ref}}{R^3}} = \sqrt{\frac{G \cdot 1}{1^3}} \rightarrow G = 1$$ (2.16)

The adimensional equations of motion, expressed in the synodic frame, become:

$$\begin{cases} \ddot{x} - 2\dot{y} = x - \dfrac{(1-\mu)(x+\mu)}{r_{sp}^3} - \dfrac{\mu(x+\mu-1)}{r_{ap}^3} \\[2mm] \ddot{y} + 2\dot{x} = y - \dfrac{(1-\mu)}{r_{sp}^3}y - \dfrac{\mu}{r_{ap}^3}y \\[2mm] \ddot{z} = -\dfrac{(1-\mu)}{r_{sp}^3}z - \dfrac{\mu}{r_{ap}^3}z \end{cases} \tag{2.17}$$

In Equation 2.17 appear the terms r_{sp} and r_{ap}: they coincide with the adimensional formulation of r_1 and r_2 already defined in relations 2.9 and 2.10. They can be expressed as follow:

$$r_{sp} = \sqrt{(x+\mu)^2 + y^2 + z^2} \tag{2.18}$$

$$r_{ap} = \sqrt{(x+\mu-1)^2 + y^2 + z^2} \tag{2.19}$$

2.3. Jacobi constant

Analysing Equation 2.15, it is possible to take the dot product with $\dfrac{\delta \boldsymbol{r}}{\delta t}$:

$$\frac{\delta \boldsymbol{r}}{\delta t} \cdot \frac{\delta^2 \boldsymbol{r}}{\delta t^2} = -\frac{\delta \boldsymbol{r}}{\delta t} \cdot \nabla U - 2\frac{\delta \boldsymbol{r}}{\delta t} \cdot \left(\boldsymbol{\Omega} \times \frac{\delta \boldsymbol{r}}{\delta t} \right) \tag{2.20}$$

In the previous equation:

- $-2\dfrac{\delta \boldsymbol{r}}{\delta t} \cdot (\boldsymbol{\Omega} \times \dfrac{\delta \boldsymbol{r}}{\delta t}) = 0$, since the dot product is performed between two vectors perpendicular to each other;

- $\dfrac{\delta \boldsymbol{r}}{\delta t} \cdot \dfrac{\delta^2 \boldsymbol{r}}{\delta t^2} = \boldsymbol{v} \cdot \dot{\boldsymbol{v}} = \dfrac{1}{2}\dfrac{d}{dt}v^2$;

- $\dfrac{\delta \boldsymbol{r}}{\delta t} \cdot \nabla U = \dfrac{\delta x}{\delta t} \cdot \dfrac{\delta U}{\delta x} + \dfrac{\delta y}{\delta t} \cdot \dfrac{\delta U}{\delta y} + \dfrac{\delta z}{\delta t} \cdot \dfrac{\delta U}{\delta z} = \dfrac{dU}{dt}$

These considerations lead to:

$$\frac{1}{2}\frac{d}{dt}v^2 + \frac{dU}{dt} = 0 \implies v^2 + 2U = -C \tag{2.21}$$

Equation 2.21 defines the so-called *Jacobi constant*, indicated with C. This quantity, by definition, is half and opposite in sign with respect to the total energy of the system,

expressed in Equation 2.22.

$$E = \frac{1}{2}v^2 + U = -\frac{1}{2}C \tag{2.22}$$

This quantity, as can be understood by Equation 2.21, is conserved in time and through the motion of the particle defining the only integral of motion of the system. Nevertheless, since this is the only quantity conserved, the 3BP can not be solved in close form.

The Jacobi constant is important since it can be used as a check during computational integration of the equations of motion but, more importantly, also because it can be used to bound the motion of the third body within a prescribed region. In fact, if an energy level and an initial position are fixed, then the magnitude of the velocity at any point is uniquely determined as well but, on the other hand, if the velocity is set to be zero at a given energy, the possible natural motion is bounded within space region that must solve the following equation [1]:

$$-2U - C = 2G\left(\frac{m_1}{r_1} + \frac{m_2}{r_2}\right) + \Omega^2(x^2 + y^2) - C = 0 \tag{2.23}$$

$$\Big\downarrow \text{[adimensionalized]}$$

$$-2U - C = 2\left(\frac{1-\mu}{r_{sp}} + \frac{\mu}{r_{ap}}\right) + (x^2 + y^2) = 0 \tag{2.24}$$

Equation 2.23 defines the so-called *Zero Velocity Curves (ZVC)*, given by the intersection of an object's energy, which is constant, with the potential energy. In particular, an object will be able to move inside the ZVC but never to go outside it (or vice versa) since, as the name suggests, it will arrive on this surface with null velocity. In particular, defining a critical Jacobi constant $C^* = -2U$, the forbidden regions will be all those that feature $C \geq C^*$, since this leads to $v^2 < 0$ that is physically unfeasible. Moreover, the ZVCs define, with their surfaces, the boundaries of the so-called *Hill's Region*. To be clearer, Figure 2.1 shows the ZVC for the Eart-Moon system obtained fixing $C = -1.5061$: after the definition of the Lagrangian points in section 2.4, it will be highlighted how the ZVCs vary dependently on the energy level of a body (see Figure 2.6).
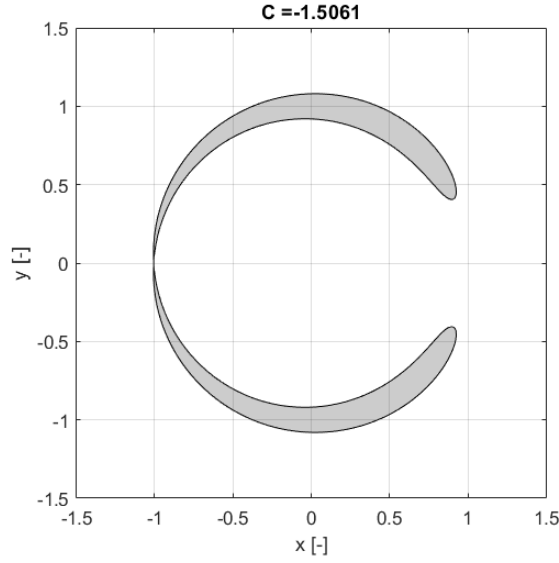
Figure 2.1: Earth-Moon system ZVC for C=-1.5061.

2.4. Lagrangian points

Another piece of information that comes out of writing the problem in the synodic frame is related to the existence of five equilibrium points fixed relatively to the rotating line linking the primaries of the system. These points the name *Lagrangian or Libration points* and represent the region in space where the centrifugal force is balanced by the gravitational attractions of the primaries. Recalling Equation 2.15, it is possible to write

$$\frac{\delta^2 \boldsymbol{r}}{\delta t^2} + 2\boldsymbol{\Omega} \times \frac{\delta \boldsymbol{r}}{\delta t} = -\nabla U \tag{2.25}$$

This expression, expressed component-wise, can be transformed into[1]:

$$\begin{bmatrix} \ddot{x} \\ \ddot{y} \\ \ddot{z} \end{bmatrix} + 2 \begin{bmatrix} 0 \\ 0 \\ \Omega \end{bmatrix} \times \begin{bmatrix} \dot{x} \\ \dot{y} \\ \dot{z} \end{bmatrix} = - \begin{bmatrix} \dfrac{\partial U}{\partial x} \\[2mm] \dfrac{\partial U}{\partial y} \\[2mm] \dfrac{\partial U}{\partial z} \end{bmatrix} \implies \begin{cases} \ddot{x} - 2\Omega\dot{y} = -\dfrac{\partial U}{\partial x} \\[3mm] \ddot{y} + 2\Omega\dot{x} = -\dfrac{\partial U}{\partial y} \\[3mm] \ddot{z} = -\dfrac{\partial U}{\partial z} \end{cases} \tag{2.26}$$

A static equilibrium, such as the condition that Lagrangian points provide, it is necessary

---

[1]For sake of simplicity and conciseness, eq. 2.26 shows only the three equations for the acceleration.

to force that $\dot{x} = \dot{y} = \dot{z} = \ddot{x} = \ddot{y} = \ddot{z} = 0$. Feeding Equation 2.26 with these conditions leads to:

$$\begin{cases} 0 = -\dfrac{\partial U}{\partial x} \\[2ex] 0 = -\dfrac{\partial U}{\partial y} \\[2ex] 0 = -\dfrac{\partial U}{\partial z} \end{cases} \tag{2.27}$$

This expression makes evident how the Lagrangian points coincide with critical points of the total potential energy, shown in Figure 2.2 for the Earth-Moon system.
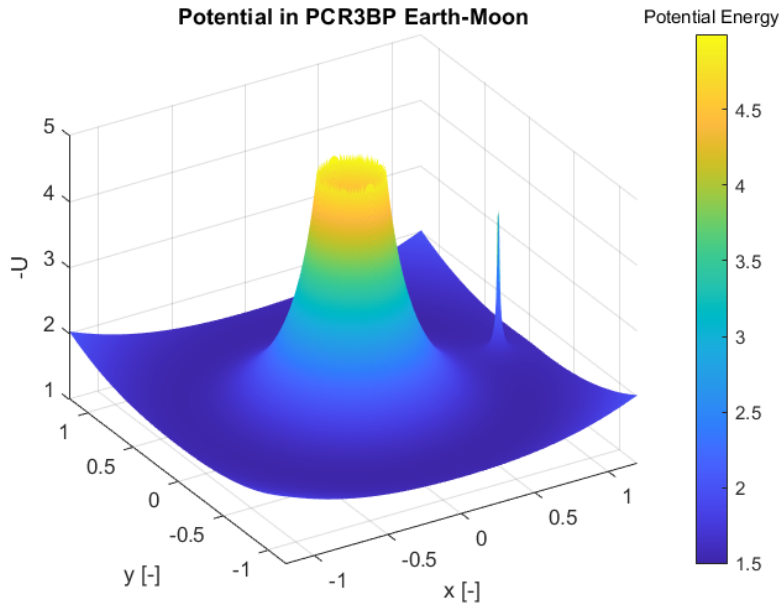
Figure 2.2: Total potential energy for PCR3BP having Earth and Moon as primaries.

2.4.1.　How to locate the Lagrangian points

As already said, the Lagrangian points are five equilibrium solutions of the *Planar Circular Restricted Three-Body Problem (PCR3BP)*. They can be divided into the so-called *collinear points*, which are three unstable equilibrium points (L_1, L_2, L_3) all located along the line connecting the primaries, i.e. the x-axis; and the so-called *equilateral points*, two points of stable equilibrium called L_4 and L_5.

Following Westra [20], let first seek for the point that does not lie along the x-axis, i.e.

the equilateral points. Denoting with r_1 and r_2 the distances from the CoM of the biggest and smallest primary respectively, the balance of forces leads to:

$$\alpha(\boldsymbol{r} - \boldsymbol{r_1}) + \beta(\boldsymbol{r} - \boldsymbol{r_2}) = \boldsymbol{r} \tag{2.28}$$

where α and β are coefficients depending on $\boldsymbol{r}$ through $|\boldsymbol{r} - \boldsymbol{r_1}|$ and $|\boldsymbol{r} - \boldsymbol{r_2}|$, respectively. Rearranging Equation 2.28 it is possible to conclude that $\alpha\boldsymbol{r_1} + \beta\boldsymbol{r_2}$ has to be parallel to $\boldsymbol{r}$. Since by construction both $\boldsymbol{r_1}$ and $\boldsymbol{r_2}$ lie along the y-axis, this means that a solution is possible only for $\alpha\boldsymbol{r_1} + \beta\boldsymbol{r_2} = 0$ (excluding $y = 0$). From the property of the center of mass it is known that $M_1\boldsymbol{r_1} + M_2\boldsymbol{r_2} = 0$, meaning that $\alpha\boldsymbol{r_1} + \beta\boldsymbol{r_2} = 0$ if and only if $\alpha : \beta = M_1 : M_2$. Precisely, α and β will take the form of

$$\begin{cases} \alpha = \dfrac{M_1}{|\boldsymbol{r} - \boldsymbol{r_1}|} \\ \beta = \dfrac{M_2}{|\boldsymbol{r} - \boldsymbol{r_2}|} \end{cases} \tag{2.29}$$

The proportional relation therefore will be satisfied only if $|\boldsymbol{r} - \boldsymbol{r_1}| = |\boldsymbol{r} - \boldsymbol{r_2}| = s$. The balance of forces expressed 2.28 becomes:

$$\frac{M_1}{s^3}(\boldsymbol{r} - \boldsymbol{r_1}) + \frac{M_2}{s^3}(\boldsymbol{r} - \boldsymbol{r_2}) = \frac{M_1 + M_2}{|\boldsymbol{r_1} - \boldsymbol{r_2}|}\boldsymbol{r} \tag{2.30}$$

Straightforwardly, this equation is satisfied only if $s = |\boldsymbol{r_1} - \boldsymbol{r_2}|$. Finally, this means that the two Lagrangian points searched are two points in the xy-plane, equally distant from the two primaries. These solutions, therefore, lie on the vertex of equilateral triangles whose base is the segment linking the two primaries. By convention, the point that is 60° ahead with respect to the smallest primary along its orbit is called L4, while L5 is the one trailing the smallest primary 60° behind it.

Let now focus instead on the research of the collinear Lagrangian points, therefore fixing $y = 0$. Following Koon et al. [21], it is possible to write the adimensional potential for the PCR3BP as:

$$U(x, 0) = -\frac{1}{2}x^2 - \frac{1 - \mu}{|x + \mu|} - \frac{\mu}{|x + \mu - 1|} \tag{2.31}$$

Referring to Koon et al. it is possible to say that $U(x, 0)$ shall present one critical point (i.e. one Lagrangian point) in each of the intervals reported in brackets in relation 2.32.

$$\begin{cases} L_1 \longrightarrow x \in (-\mu, 1 - \mu) \\ L_2 \longrightarrow x \in (1 - \mu, \infty) \\ L_3 \longrightarrow x \in (-\infty, -\mu) \end{cases} \tag{2.32}$$

Furthermore, from 2.31, it is straightforward to compute the second derivative of the potential with respect to the x-coordinate, reported in 2.33.

$$\frac{d^2 U}{dx^2}(x, 0) = -1 - \frac{1 - \mu}{|x + \mu|^3} - \frac{\mu}{|x + \mu - 1|^3} \tag{2.33}$$

Expression 2.33 is always negative, meaning that $U(x, 0)$ is always concave in each of the intervals reported in 2.32, therefore it will present precisely one critical point within each interval. This is clearly highlighted in Figure 2.3, where the potential function is depicted for $\mu = 0.1$.
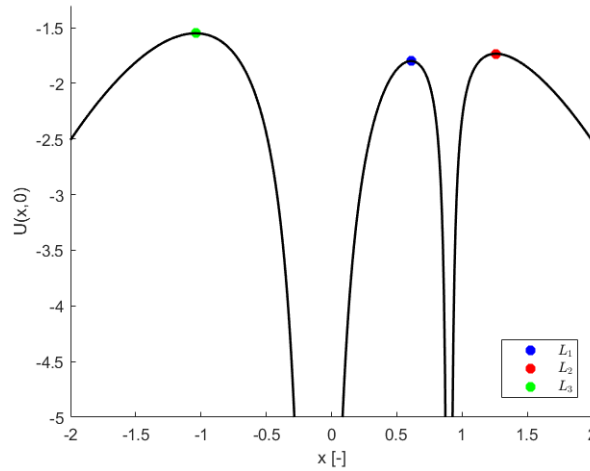
Figure 2.3: Critical points of the potential function with $\mu = 0.1$, fixing $y = 0$. This image clearly shows how each point falls within one of the intervals expressed in 2.32.

At this point, in order to locate the collinear points, it is easy to understand from Figure 2.3 that is required to compute the local maxima of the potential function, i.e. forcing $\frac{d}{dx}U(x, 0) = 0$. Defining as γ the distance between the i_{th} Lagrangian point and the closest primary from it, it will hold that [21][22]:

$$
\begin{cases}
L_1: & \gamma^5 - (3-\mu)\gamma^4 + (3-2\mu)\gamma^3 - \mu\gamma^2 + 2\mu\gamma - \mu = 0 \\
L_2: & \gamma^5 + (3-\mu)\gamma^4 + (3-2\mu)\gamma^3 - \mu\gamma^2 - 2\mu\gamma - \mu = 0 \\
L_3: & \gamma^5 + (2+\mu)\gamma^4 + (1+2\mu)\gamma^3 - (1-\mu)\gamma^2 - 2(1-\mu)\gamma - (1-\mu) = 0
\end{cases}
\tag{2.34}
$$

The series expansion of these solutions is provided by Szabehely et al. [22] and Moulton et al. [23]. The expressions are stated in 2.35. It is then possible to feed those solutions into a numerical solver, exploiting for example a Newton method, in order to retrieve the exact solution of the quintic equations reported in 2.34. Finally from them, it is easy to recover the positions of the collinear Lagrangian points from relation 2.36.

$$
\gamma_1 = r_h \left(1 - \frac{1}{3}r_h - \frac{1}{9}r_h^2 + ... \right)
$$

$$
\gamma_2 = r_h \left(1 + \frac{1}{3}r_h - \frac{1}{9}r_h^2 + ... \right)
\tag{2.35}
$$

$$
\gamma_3 = \frac{7}{12}\mu + \frac{23 \cdot 7^2}{12^4}\mu^3 + ...
$$

$$
\begin{cases}
L_1 = (1-\mu) - \gamma_1 \\
L_2 = \gamma_2 + (1-\mu) \\
L_3 = -\mu - \gamma_3
\end{cases}
\tag{2.36}
$$

In 2.35, the term r_h is called *Hill radius*, which can be computed as $r_h = (\frac{\mu}{3})^\eta$, with $\eta = \frac{1}{3}$. In fact, $\eta = \frac{1}{3}$ corresponds to the spherical volume within which the effects of the biggest primary are of the same order of magnitude with respect to the ones given by the smaller primary [24]. This, in particular, is defined as Hill's sphere, an argument that will be discussed in more detail in section 2.5.

The following figures represent the positions of the Lagrangian points found following the procedure described until now, in the case of the Earth-Moon three-body problem. Figure 2.5 reports a contour plot of the potential in Figure 2.2: this highlights particularly well the absolute dependence of these equilibrium points from the potential energy of the system. From Figures 2.4 and 2.5 is also evident how, due to Moon's gravitational effect, the point L_1 is able to rotate with the same angular rate (its position must remain fixed in the synodic frame) even though it is closer to Earth.

Finally, the numerical coordinates of the Lagrangian points, for the Earth-Moon system,
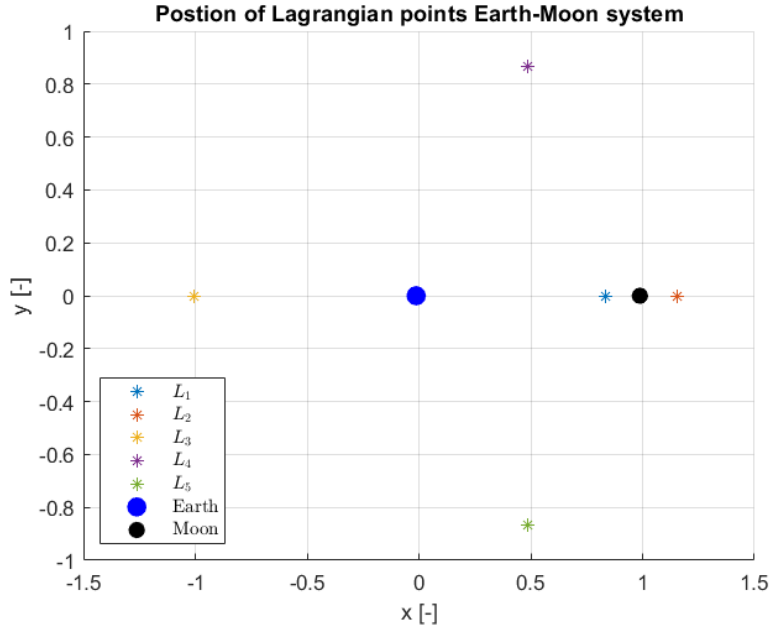
Figure 2.4: Position of the Lagrangian points in the Earth-Moon system.

are reported in Table 2.1.

Point	x [-]	y [-]
L_1	0.836905544208351	0
L_2	1.155683393219745	0
L_3	-1.005062645554134	0
L_4	0.487849413370501	0.866025403784439
L_5	0.487849413370501	-0.866025403784439

Table 2.1: Earth-Moon system LP's coordinates.

Once introduced the Lagrangian points, following [21], it is possible to distinguish the five cases of the Hill's region, the region bounded by the ZVCs. Calling E_i the energy associated to the i_{th} Lagrangian points, the possible scenarios are here below enumerated and shown in Figure 2.6.

1. $E < E_1$: the particle can not freely move from one primary to the other. The two realms are completely disconnected each other and also with the external one.

2. $E_1 < E < E_2$: a neck region around the first Lagrangian point opens, enabling a particle to pass from the bigger primary to the other and vice-versa but could never reach the external realm.

3. $E_2 < E < E_3$: at this energy level, not only the two realms are connected each other, but a particle can potentially escape from the system through the bottleneck
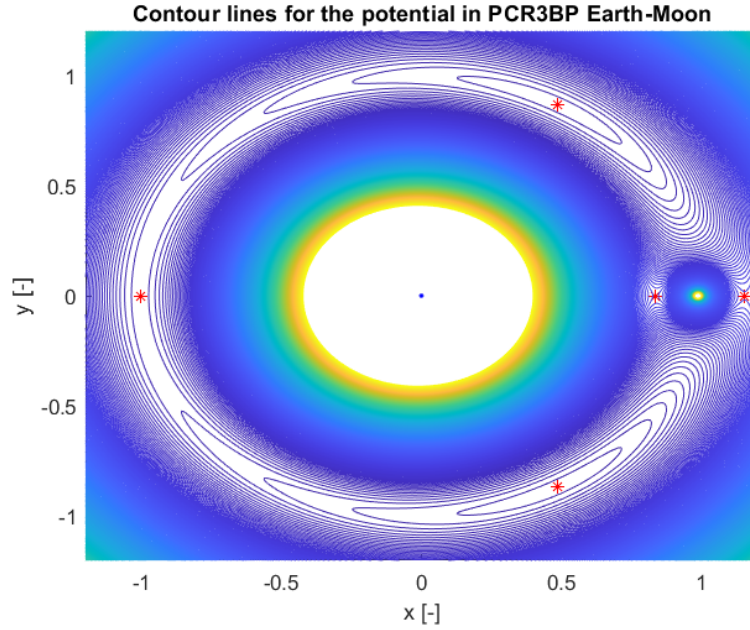
Figure 2.5: Position of the Lagrangian points in the Earth-Moon system. This plot clearly highlights the dependence of these equilibrium points on the potential function.

that opens at L2.

4. $E_3 < E < E_4 = E_5 = -3/2$: also a "backdoor" passage is opened for this energetic range. A neck opened at L3, in fact, enables the particle to escape form the system without passing for L1 and L2 bottlenecks. Note that E_4 is always equal to E_5, corresponding to -3/2.

5. $E > E_4 = E_5$: in this case, the particle is completely free to move everywhere. The forbidden realm has disappeared.

2.5. Hill's problem

Since this work is focused on the study of a Sun-Asteroid three-body system, it is convenient to make use of the so-called Hill's approximation, originally introduced for the study of lunar motion (Hill, 1878). Citing Batkhin [25], this approach can be seen as a limiting case of the R3BP for cases in which the smaller primary is vanishingly less massive than the bigger one, a condition that is perfectly suitable for the asteroid's case. From Equation 2.7, it is easy to understand that $0 \leq \mu \leq 1/2$ always, limits that correspond to $m_1 >> m_2$ and $m_1 = m_2$ respectively. This means that Hill's approximation is non-other than the study of the first limiting case, having $\mu \longrightarrow 0$ ([26]). Quoting Henon [27], the case of $\mu = 0$ can seem trivial: in this case, in fact, a third body feels the attraction of
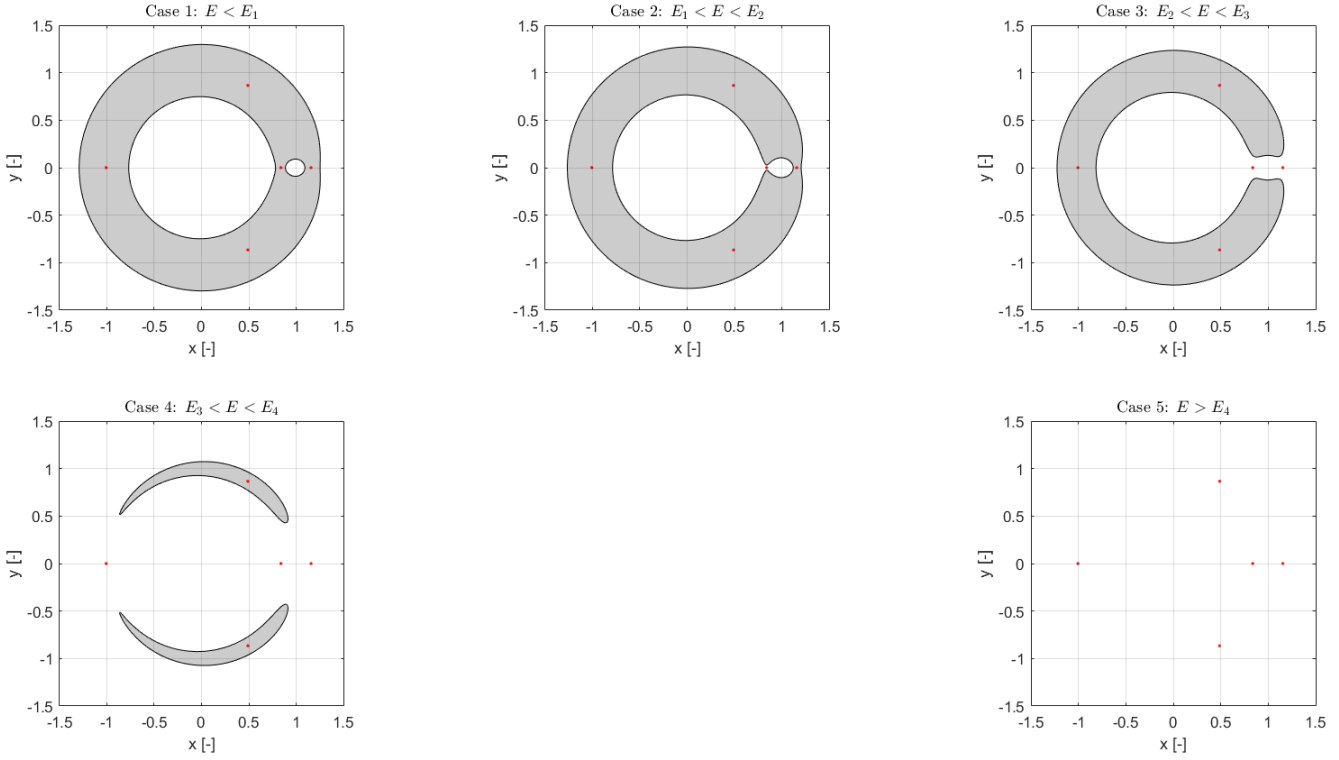
Figure 2.6: Cases for the Hill's Region: the results shown are completely in accordance with theory [21].

the bigger primary only, having therefore its motion described by the simple Keplerian two-body problem. However Hill, in 1886 [28], found a way to reach a non-trivial formulation for such a problem. Starting from a small value of μ but anyway different from zero, there will be a region in the neighborhood of the second primary within which its effect is not negligible but rather comparable with the one carried out by the biggest body. If at this point, it is let $\mu \longrightarrow 0$, i.e. making the second primary smaller and smaller, and, at the same time, the third body is moved closer and closer to it by an appropriate change of scale, the result will be a non-trivial system providing results different with respect to the ones of the two-body problem. The main advantages arising from such a formulation are the following [29][30]:

- the relative and the center of mass motions can be separated and the equation for the motion of the center of mass can be integrated analytically;

- it is an invariant model that does not depend on any parameter, thus resulting in broad generality for the results, whose application to different systems becomes a simple matter of scaling;

- the Jacobi constant is preserved;

- when numerically treated, the equations of motion of this formulation (see Equation 2.42) are not dependent on μ, avoiding numerical-related issues that would arise.

- it is a model that can be applied assuming that the distance between the Sun and the asteroid is much larger than the distance between the spacecraft and asteroid [3], which is a likely situation .

Following [27], it is possible to re-scale the coordinates as follows:

$$
\begin{cases}
x = 1 - \mu + \mu^{1/3} x_{Hill} \\
y = \mu^{1/3} y_{Hill}
\end{cases}
\tag{2.37}
$$

Substituting 2.37 into 2.17 and letting $\mu \longrightarrow 0$, the result is the *Hill's equations*:

$$
\begin{cases}
\ddot{x}_{Hill} - 2\dot{y}_{Hill} = -\dfrac{x_{Hill}}{r^3} + 3x_{Hill} \\[2ex]
\ddot{y}_{Hill} + 2\dot{x}_{Hill} = -\dfrac{y_{Hill}}{r^3}
\end{cases}
\tag{2.38}
$$

where $r = \sqrt{x_{Hill}^2 + y_{Hill}^2}$.

The Jacobi constant itself, even though still conserved, must be subjected to a re-scale as well. In particular, feeding 2.40 into 2.39 and making μ going towards 0, the re-scaled Jacobi constant can be expressed as stated in 2.41.

$$
C = 2 \left(\frac{1 - \mu}{r_{sp}} + \frac{\mu}{r_{ap}} \right) + (x^2 + y^2) - \dot{x} - \dot{y}
\tag{2.39}
$$

$$
C = 3 + \mu^{(2/3)} \Gamma
\tag{2.40}
$$

$$
\Gamma = 3x_{Hill}^2 + \frac{2}{r} - \dot{x}_{Hill} - \dot{y}_{Hill}
\tag{2.41}
$$

Once achieved this, highlighting the difference of the coordinates used in this new approach, for sake of brevity the subscript "Hill" will be no more reported from here on. Extending now the dissertation also along the third coordinate, the equations of motion and the Jacobi constant become [31]:

$$\begin{cases} \ddot{x} - 2\dot{y} = -\dfrac{x}{r^3} + 3x \\[2em] \ddot{y} + 2\dot{x} = -\dfrac{y}{r^3} \\[2em] \ddot{z} = -\dfrac{z}{r^3} - z \end{cases} \qquad (2.42)$$

$$\Gamma = 3x^2 + \frac{2}{r} - z^2 - (\dot{x}^2 + \dot{y}^2 + \dot{z}^2) \qquad (2.43)$$

where $r = \sqrt{x^2 + y^2 + z^2}$.

2.6. Perturbations Affecting the Dynamics

The discussion done until now does not include any perturbation affecting the motion of the third body. However, in general, this is not true. In particular, there are different kinds of forces that need to be taken into account to model the dynamics of asteroid ejecta, and several of them strongly depend on the size of the ejecta itself. Referring to Gustafson [32], identifying with s the linear dimension of a particle, while gravity is proportional to s^3 and pressure forces to s^2, electromagnetic Lorentz forces are proportional to s. The result is that this last action can usually be neglected for micrometer-sized particles, at least within Jupiter's orbit (that is the case of this work). For these reasons, the disturbances considered will be the ones due to the *solar radiation* and the *aspherical harmonics* gravitational perturbation.

2.6.1. Solar Radiation Pressure (SRP)

The effect of SRP is also in this case, as usually done, considered through a cannon-ball model. This method describes how spherical objects with equally distributed optical properties are affected by solar pressure [1]. These are all features that fit well with the problem considered. Moreover, in this way, the force due to SRP is systematically directed in the opposite direction of the Sun [33] and can be treated as conservative. This implies that the SRP contribution can be expressed as a potential [2]. Going into more details, from [19]:

$$\boldsymbol{F} = \frac{Gm_s m}{r_{sp}^2} \beta \left(\left(1 - \gamma \frac{\dot{r}}{c} \right) \hat{\boldsymbol{r}} - \gamma \frac{\boldsymbol{v}}{c} \right) \qquad (2.44)$$

where $\hat{\boldsymbol{r}} = \boldsymbol{r}/r$ is the radial versor, $\dot{r} = dr/dt$ is the radial velocity of the system, $\boldsymbol{v} = d\boldsymbol{r}/dt$ is the instantaneous velocity of the particle, c is the speedlight, $\gamma = 1 + F_{SW}/F_{PR}$ [^2]. If for $\gamma = 1$ the effect of the solar wind is neglected, for $\gamma = 0$ the only contribution considered is the SRP, ignoring therefore also the Pointing-Robertson effect. This, in fact, acts on time scales way larger than the ones of interest in this work and thus can be safely neglected [24].

Equation 2.44 presents also the term β, the so-called *lightness parameter*. This is the real key parameter in the study of the SRP effect and can be written as follows [2] [1]:

$$\beta = P_0 \frac{AU^2}{\mu_{sun}} \frac{3c_R}{2\rho_p d_p} \tag{2.45}$$

In 2.45:

- AU is the astronomic units, equal to $1.496 \cdot 10^8 km$

- P_0 is the solar flux at 1AU, equal to $1367 W/m^2$;

- c_R is the particle reflectivity coefficient;

- ρ_p is the particle density;

- d_p is the particle diameter;

Finally, from Equation 2.44 with $\gamma = 0$ and $V_{SRP} = -\beta \frac{\mu_{Sun}}{r_{sp}}$, the SRP contribute on acceleration can be written as:

$$\boldsymbol{a_{SRP}} = \frac{\beta \mu_{Sun}}{r_{sp}^2} \hat{\boldsymbol{r}} = \nabla V_{SRP} \hat{\boldsymbol{r}} \tag{2.46}$$

From 2.45 it is possible to see how β can be defined as the ratio between the SRP acceleration and the solar gravity acceleration. Even though, however, here P_0 is treated as a constant it should be noted that, for a fixed position in space, the solar flux is actually a time-dependent variable ruled by the solar cycle [1]. This results in a no-more strictly autonomous system whenever SRP is considered.

The equations of motion and the Jacobi constant become [31]:

[^2]: SW stands for *Solar wind* while PR for *Pointing-Robertson*.

$$
\begin{cases}
\ddot{x} - 2\dot{y} = -\dfrac{x}{r^3} + 3x + \beta \\[3mm]
\ddot{y} + 2\dot{x} = -\dfrac{y}{r^3} \\[3mm]
\ddot{z} = -\dfrac{z}{r^3} - z
\end{cases}
\tag{2.47}
$$

$$
\Gamma = 3x^2 + 2\beta x + \frac{2}{r} - z^2 - (\dot{x}^2 + \dot{y}^2 + \dot{z}^2)
\tag{2.48}
$$

The system of equations 2.47, that takes the name of *Photo-gravitational Hill Problem*, highlights how, whenever considering the SRP, i.e. $\beta \neq 0$, the dynamics of a particle will be strongly dependent on it dimensions. This means that SRP can be used a passive in-situ mass spectrometer (the larger the grain, the lower the β) [34]. Alternatively, after a grinding process to reduce all materials to a similar grain size, SRP can be exploited to sort particles by their density. Such opportunities are crucial to assess the dimensions and properties of the particles that will be gathered in a collection mission.

2.6.2.   Gravitational perturbation

When dealing with irregularly shaped bodies, such as asteroids, it becomes crucial to model the gravitational potential, but, since very little information are usually known concerning these bodies, this task is far from being trivial. The standard tool used for this goal is the spherical harmonics expansion: since it models the distribution of mass inside a sphere circumscribing the body, the method is suitable to describe small deviations from a spherical shape. This, at the end, means that in the case of strongly irregular and inhomogeneous bodies, expansions up to, usually, 24 degrees and orders are needed in order to match the irregular features of their gravitational potentials [10]. Nevertheless, the series will converge to the true gravity field only outside the chosen circumscribing sphere. Considering an Asteroid-Centred-Asteroid-Fixed (ACAF) reference frame, and defining the radial distance (r), the latitude (δ) and the longitude (λ) as shown in Equation 2.49, the general formulation of the potential[3] can be transformed into 2.50 [1].

---

[3]Note that $V = -U$.

$$\begin{cases} r = \sqrt{x_{ACAF}^2 + y_{ACAF}^2 + z_{ACAF}^2} \\ \sin \delta = \dfrac{z}{r} \\ \tan \lambda = \dfrac{y}{x} \end{cases} \tag{2.49}$$

$$V(r, \delta, \lambda) = \frac{\mu}{r} \sum_{l=0}^{\infty} \sum_{m=0}^{l} \left(\frac{R_{ref}}{r} \right)^l P_{lm} \sin \delta \left[C_{lm} \cos(m\lambda) + S_{lm} \sin(m\lambda) \right] \tag{2.50}$$

In 2.50:

- μ is the gravitational parameter of the asteroid;

- R_{ref} is the reference radius (i.e. the maximum or the mean radius) of the asteroid;

- $P_{lm} \sin \delta$ represent the associated Legendre polynomial (for $m = 0$ it becomes the conventional Legendre polynomials);

- C_{lm} and S_{lm} are the gravity field coefficients that identify the body studied. As a convention $J_l = -C_l$.

Since this work aims to just consider the J_2 perturbation, it is necessary to write down the conventional (i.e. $m = 0$) Legendre polynomials, with $l = 2$. These orthogonal polynomials $P_{l,0}(\nu)$ must satisfy 2.51 that, when solved, can be written as 2.52, known as *Rodrigues' formula* from the mathematician that first recovered it [35].

$$(1 - 2\nu x + x^2)^{-1/2} = \sum_{l=0}^{\infty} P_l(\nu) x^l \tag{2.51}$$

$$P_l(\nu) = \frac{1}{c^l l!} \frac{d^l}{d\nu^l} (\nu^2 - 1)^l \tag{2.52}$$

For $l = 2$, Equation 2.52 becomes:

$$P_2 = P_{2,0} = \frac{1}{2} (3\nu^2 - 1) \tag{2.53}$$

Substituting $\nu = \sin \delta$, after some manipulations the gravitational potential becomes:

$$V_{J_2} = \frac{\mu}{r} \left[1 - \frac{1}{2} J_2 \left(\frac{R_{ref}}{r} \right)^2 \left(3 \sin^2 \delta - 1 \right) \right] \tag{2.54}$$

$$J_2 = -C_{2,0} = \frac{1}{5R_{ref}} \left(c^2 - \frac{a^2 + b^2}{b} \right) = 0.008347066115702 \tag{2.55}$$

where a, b and c are shown in table 1.2.

A deeper dissertation is outside the aim of this work, thus if interested please refer to [1]. The conclusion is that, after some processes, the total potential V can be written as:

$$V = \frac{1}{2}\bar{n}^2(x^2 + y^2) + \frac{(1-\mu)(1-\beta)}{r_{sp}} + \frac{\mu}{r_{ap}}\left[1 - \frac{1}{2}J_2\left(\frac{\bar{a}}{r_{ap}}\right)^2\left(3\frac{z^2}{r_{sp}^2} - 1\right)\right] \tag{2.56}$$

with $\bar{a} = R_{ref}/R$ and $\bar{n}^2 = 1 + \frac{3}{2}J_2\bar{a}^2$. Writing than the equations of motion as stated in 2.57, the dynamics of a particle affected by both SRP and aspherical potential can be described by 2.58.

$$\begin{cases} \ddot{x} - 2\bar{n}\dot{y} = V_x \\ \ddot{y} + 2\bar{n}\dot{x} = V_y \\ \ddot{z} = V_z \end{cases} \tag{2.57}$$

$$\begin{cases} \ddot{x} - 2\bar{n}\dot{y} = \bar{n}^2x - \frac{(1-\beta)(1-\mu)(x+\mu)}{r_{sp}^3} - \frac{\mu}{r_{ap}^3}\left[1 - \frac{3}{2}J_2\left(\frac{\bar{a}}{r_{ap}}\right)^2\left(5\frac{z^2}{r_{ap}^2} - 1\right)\right](x+\mu-1) \\ \\ \ddot{y} + 2\bar{n}\dot{x} = \bar{n}^2y - \frac{(1-\beta)(1-\mu)}{r_{sp}^3}y - \frac{\mu}{r_{ap}^3}\left[1 - \frac{3}{2}J_2\left(\frac{\bar{a}}{r_{ap}}\right)^2\left(5\frac{z^2}{r_{ap}^2} - 1\right)\right]y \\ \\ \ddot{z} = -\frac{(1-\beta)(1-\mu)}{r_{sp}^3}z - \frac{\mu}{r_{ap}^3}\left[1 - \frac{3}{2}J_2\left(\frac{\bar{a}}{r_{ap}}\right)^2\left(5\frac{z^2}{r_{ap}^2} - 3\right)\right]z \end{cases} \tag{2.58}$$

2.6.3.   How disturbances affect lagrangian points

This section it is shown how the perturbation discussed above affects the location of the collinear Lagrangian points (since the focus of this study is on L_2) and the zero velocity curves.

In particular, when taking into account SRP, the quintic expressions shown 2.34 become:

$$L_1 : \gamma_1^5 - (3 - \mu)\gamma_1^4 + (3 - 2\mu)\gamma_1^3 - (\mu + (1 - \mu)\beta)\gamma_1^2 + 2\mu\gamma_1 - \mu = 0$$

$$L_2 : \gamma_2^2 + (3 - \mu)\gamma_2^4 + (3 - 2\mu)\gamma_2^3 - (\mu - (1 - \mu)\beta)\gamma_2^2 - 2\mu\gamma_2 - \mu = 0 \qquad (2.59)$$

$$L_3 : \gamma_3^5 + (2 + \mu)\gamma_3^4 + (1 + 2\mu)\gamma_3^3 - (1 - \beta)(1 - \mu)\gamma_3^2 - 2(1 - \beta)(1 - \mu)\gamma_3 - (1 - \beta)(1 - \mu) = 0$$

Solving these relations for the distance γ_i, it is then possible to find how the distances of the Lagrangian points from the center of mass of the system vary with β: Figure 2.7 shows these trends for the Earth-Moon system. In this case β goes from 0 to 1, corresponding to $a_{SRP} = 0$ and $a_{SRP} = a_{SolarGravity}$ respectively.

As can be seen, L_2 moves closer and closer to the Moon but, of course, it never approaches distances within the interval $(0, 1 - \mu)$. Both L_1 and L_3 instead, move towards the barycentre of the system.
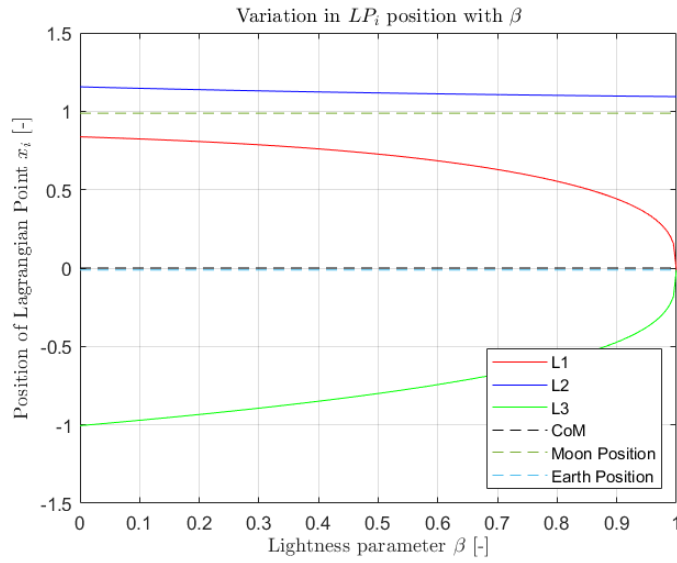
Figure 2.7: Variation of LP_i coordinate for increasing β

These results can of course be generalized to every three-body system. In particular, since, as previously said, L_2 moves towards the smaller body for bigger values of the lightness parameter, there will be a value of β for which the Lagrangian point coincides with the surface of the second primary. Following the analytical approximation of the position of L_2 realized by Latino et al. [1], the position of the coordinate of the second Lagrangian point can be obtained as:

$$x_2 = 1 - \mu + \sqrt{\frac{\alpha}{\beta}} \qquad (2.60)$$

with $\alpha = \mu/(1-\mu)$.

Reversing 2.60, it is therefore possible to find the value of β for which the Lagrangian point touches the surface of the second primary, i.e. $\gamma_2 = R$, with R being its radius (Equation 2.61).

$$\beta = \frac{\alpha}{(x_2 - 1 + \mu)^2} \tag{2.61}$$

This approximation holds under the assumption that $m_2 << m_1$, i.e. for very low values of μ. Such a condition is always true for the Sun-Asteroid system, while could be less accurate for a more proportional system such as the Earth-Moon one. The following lines will be devoted to investigating different errors committed applying Equation 2.60 for two different systems. In particular the focus will be on:

1. Earth-Moon system $\longrightarrow \mu = 0.01215$;

2. Sun-Ryugu system $\longrightarrow \mu = 2.27847 \cdot 10^{-19}$.
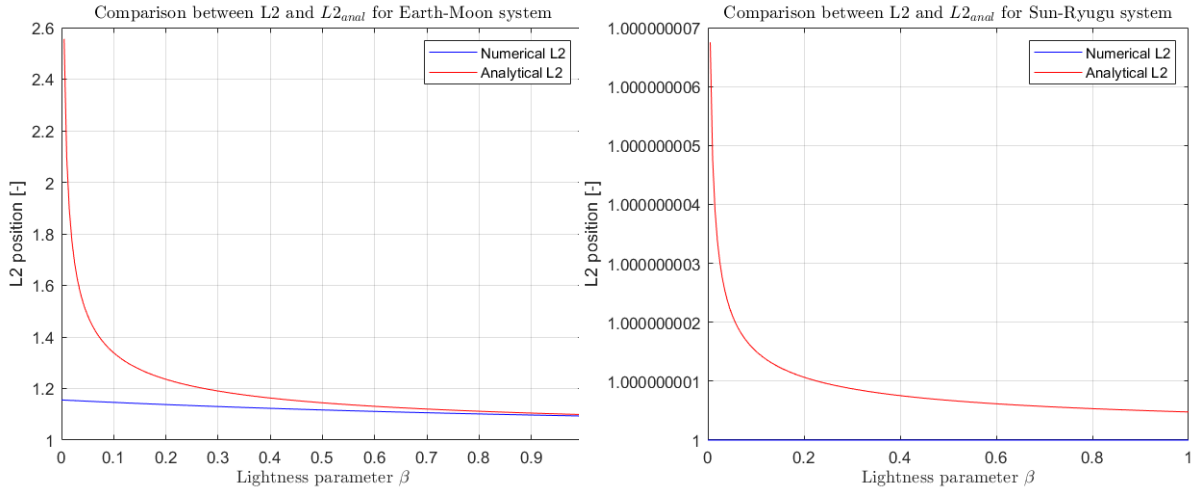
Figure 2.8: Behavior of L2 analytical and numerical for Earth-Moon system

Figure 2.9: Behavior of L2 analytical and numerical for Sun-Ryugu system

Even though Figures 2.8 and 2.9 present almost the same trend, the scale to which they refer is completely unbalanced. In fact, observing Figures 2.10 and 2.11 it is possible to see that, while the maximum error for the Sun-Ryugu case is around 1 km, for the Earth-Moon system the error is of the order of 10^5 km, meaning that the approximation applied is totally unsuitable for this kind of systems.

Up to this point, to make graphs, trends and behaves, it has always been shown the Earth-Moon case, since its higher μ granted a clearer vision of what was explained. Nevertheless,
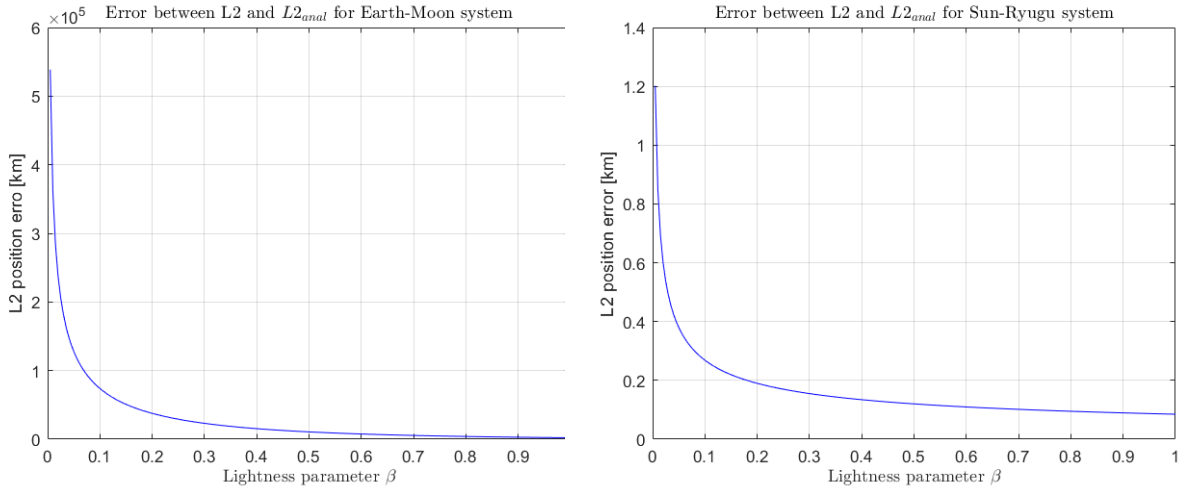
Figure 2.10: Error made between L2 analyt-Figure 2.11: Error made between L2 analytical and numerical for Earth-Moon system ical and numerical for Sun-Ryugu system

for the reasons discussed now, in order to show how ZVCs behave for different values of β and from here on, the reference system will be the Sun-Ryugu three-body system, finally entering into the study of a Sun-asteroid system as foreseen by this work.

Including now also the effect of the body's oblateness, the Equation 2.59 can be written, for the cases of L_1 and L_2, as follows [36]:

$$\begin{aligned}\pm 2n^2\gamma_i^7 + (2n^2\mu - 6n^2)\gamma_i^6 \pm (6n^2 - 4n^2\mu)\gamma_i^5 + (2n^2\mu - 2q\mu - 2n^2 + 2q \mp 2\mu)\gamma_i^4 \\ + 4\mu\gamma_i^3 \mp (2\mu + 3A\mu)\gamma_i^2 + 6A\mu\gamma_i \mp 3A\mu = 0\end{aligned} \tag{2.62}$$

for $j = 1, 2$. In Equation 2.62 $q = 1 - \beta$, $A = J_2 R_{ref}^2$ and n is the rotation rate, equal to 1 when using the adimensional formulation. By solving it, it is possible to retrieve the positions of the first and second Lagrangian points modified by the effect of the asteroid's oblateness. In particular, the difference between their coordinate with or without considering J_2 versus β is shown in Figure 2.12. The plot is completely in accordance with the effects caused by the SRP. The behavior of L1, in fact, shows that, since it moves towards the barycentre of the system, initially there will be a difference between $L1_{J_2}$ and L1 but, after a certain threshold, the asteroid is so far that the effect of its oblateness becomes negligible, therefore $L1_{J_2} - L1 = 0$. Contrarily, for L2 the situation is different: this Lagrangian point, in fact, shifts towards the asteroid for increasing values of β. This means that, for higher values of β, L2 will move closer and closer to the asteroid therefore feeling more and more the effect of its oblateness. The difference $L2_{J_2} - L2$ will

then increase for higher β, as clearly shown in Figure 2.12. Nevertheless, this shift is of the order of centimeters, being therefore practically negligible.
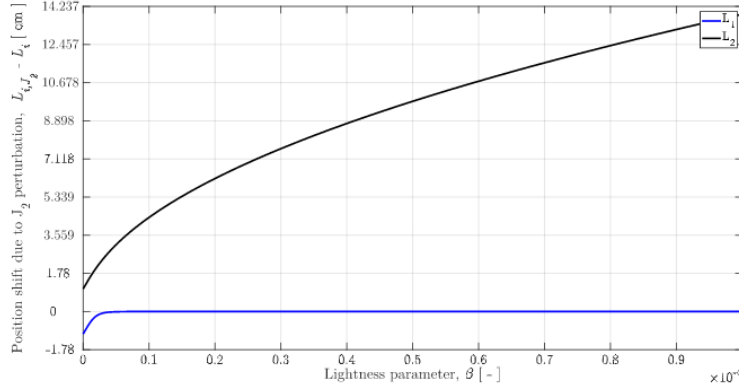
Figure 2.12: Position shift for L1 and L2 when considering SRP+J_2 or SRP only [1]

2.6.4.   How disturbances affect the zero velocity curves

Now that the behavior of the Lagrangian points including the different disturbances is known, it is possible to study how this will affect the ZVCs.

As understood, L2 shifts towards the asteroid as β increases: therefore, there will be a value for which the Lagrangian point is located on Ryugu's surface. Recalling Equation 2.61 and imposing $x_2 = R_{Ryugu}$, the value of the lightness parameter for which this happens is $\beta_{crit} = 0.0372972$. At this point, in the Equation 2.45 it is possible to impose the:

- $c_R = 0.07$ [31], avoiding the assumption of ideal specular reflection (i.e. $c_R = 2$) as done in [1];

- approximating the ejecta density with the one of the bulk of Ryugu, $\rho_p = 1282 kg/m^3$ (see table 1.2);

Being the other terms constants, the only parameter left is the ejecta size d_P. It is therefore possible to understand for which size, under these conditions, L2 will approach Ryugu's surface. In particular:

$$d_P = P_0 \frac{AU^2}{\mu_{sun}} \frac{3c_R}{2\rho_p \beta_{crit}} =\sim 1.689 \mu m$$

Figure 2.13 shows the ZVC associated with such values of particle size. According to the dissertation done, L2, represented by the red dot, is located on the surface of Ryugu. From the same plot, it is evident how part of the allowed region falls inside the asteroid,

being therefore impossible to exploit. The region on the asteroid's dark side (towards the right), i.e. the one opposite to the Sun, is almost completely allowed. In such a scenario, all the particles ejecting from that side of the asteroid will then escape through heliocentric trajectories. It is therefore useful to impose a lower limit to the particle size and consequently on the maximum value of β, in order to study cases in which ejecta actually have some closed region in the neighborhood of the asteroid within which they can freely move. Fixing a distance of $3km$ from Ryugu, it is found $\beta = 8.02315 \cdot 10^{-4}$ corresponding to a size particle $r_P \simeq 78.5\mu m$. This case is shown in Figure 2.14. Contrarily, there is no upper limit defined by the physics of the problem. This is then assessed by imposing a maximum size for asteroid ejecta equal to $r_P = 10mm$, i.e. $\beta = 6.29804 \cdot 10^{-6}$. Figure 2.15 shows the ZVC for this scenario, highlighting a position for L2 equal to $32.48km$.
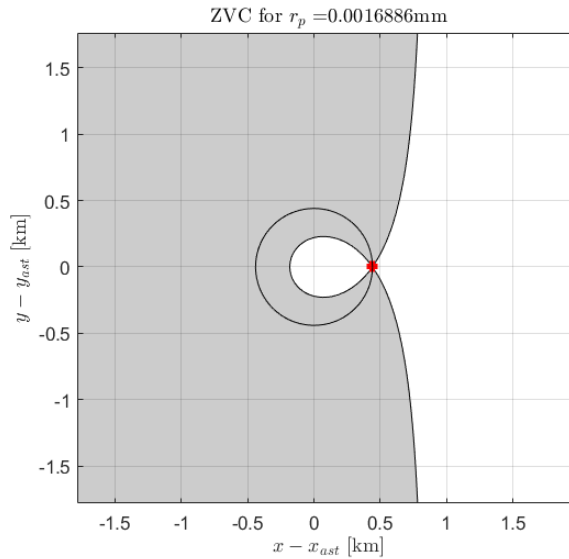
Figure 2.13: ZVC for critical lightness parameter, corresponding to $d_P = 1.689\mu m$
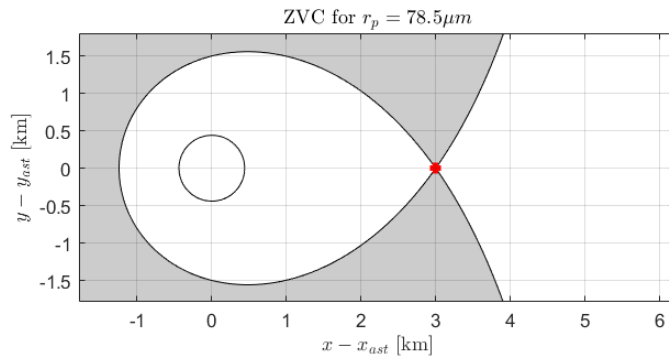
Figure 2.14: ZVC for $r_P = 78.5\mu m$, locating the LP at $3km$ from Ryugu.
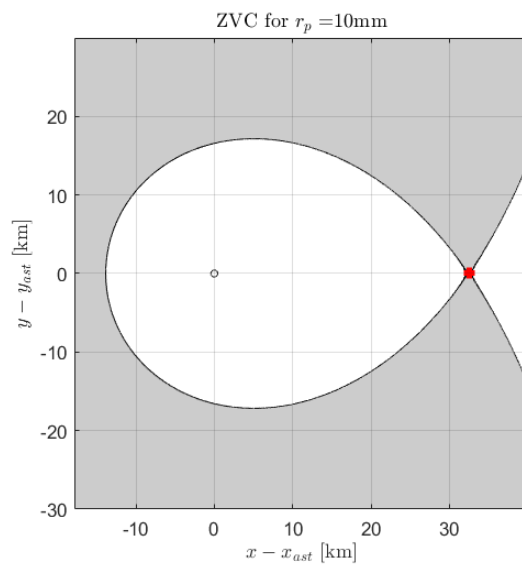
Figure 2.15: ZVC for $r_P = 10mm$, corresponding to a position for the LP of $32.48km$ from Ryugu.

3 | Ejecta dynamics and database creation

In this chapter the motion of the ejecta particles will be analyzed, identifying the number of particles falling within one of the following categories:

1. particles that re-impact on the asteroid shortly after their ejection;

2. particles that after an imposed time window are still orbiting around the asteroid;

3. particles that are able to escape from the system through the bottleneck opened at L2.

Only the ejecta of the third class will be the ones considered as collectible from a satellite orbiting a halo.

Following the example of the Hayabusa2 mission, the ejecta are assumed to be produced by a kinetic impactor that, creating a crater on the asteroid's soil, will push the so-formed particles away from its surface. Quoting Buhl et al. [37], ejecta size is much more correlated with the characteristics of the material rather than the impact energy, therefore it is hard to clearly understand a particle's dimension and velocity after the collision. For this reason, Housen & Holsapple [38] performed laboratory measurements of impact crater ejecta from 18 different studies. These are used from them to assess the dependence of ejecta velocity and mass distributions on the conditions of the impact event. They successfully recover point-source scaling laws to distinguish ejection properties for several classes of materials having different porosity. The outcome of these works gives the relation between the ejecta speed and mass with respect to the impactor characteristics, and it is reported in Equations 3.1 and 3.2 [24].

$$\frac{v}{U} = C_1 \left[\frac{x}{a} \left(\frac{\rho}{\delta} \right)^{\nu} \right]^{-1/\mu} \left(1 - \frac{x}{n_2 R} \right)^p \qquad n_1 a \leq x \leq n_2 R \qquad (3.1)$$

$$M = M_P \frac{3k}{4\pi} \frac{\rho}{\delta} \left[\left(\frac{x}{a} \right)^3 - n_1^3 \right] \qquad n_1 a \leq x \leq n_2 R \qquad (3.2)$$

In these equations v, U are the velocities of ejecta and projectile respectively; M, M_P are the masses of ejecta and projectile respectively; R, a are the radii of the crater and projectile respectively; ρ, δ are the densities of the soil surface and projectile respectively; x is the radial distance from the center of the crater while $C_1, \nu, \mu, p, n_1, n_2, k$ are non-dimensional constants depending on the material properties of the projectile and the target.

However, even though an impact on Ryugu already happened, meaning that such coefficients are quite well estimated, these parameters are difficult to retrieve in a general case, especially for poorly known asteroids. For this reason, this work approaches the problem the other way around, flipping over the point of view. Similarly to what has been done by Latino et al. [1], in fact, in this thesis the initial conditions relative to the ejecta are retrieved by discretizing on longitude and ejection angle, retrieving in this way the initial condition at each iteration of the loop.

First, it is required to recover of the magnitude of the particles' ejection velocity. Recalling what has been previously said, due to the presence of an integral of motion (i.e. the Jacobi constant) if the position and the energy level are fixed, then the velocity is unequivocally determined as well. This allows to exploitation of an energetic approach to find its value. In particular, from the definition of the Jacobi constant expressed in Equation 2.21 it is possible to compute the magnitude of the ejecta velocity with respect to a prescribed energy level. It has been chosen for this purpose the level corresponding to the second Lagrangian point since it represents the threshold value required in order to open a bottleneck in the ZVC and escape from the system. The velocity, therefore, can be written as follows:

$$v_{ej}(x, y, \beta) = \sqrt{C(x, y, \beta) - C_2} \tag{3.3}$$

The position, i.e. the x and y coordinates, depends of course on the longitude θ, while β is directly linked with the size of the particle (see Equation 2.45). The procedure to find v_{ej} therefore is:

1. initialisation of a loop on the particle size r_P;

2. for each value of r_P the β parameter is computed;

3. from β the analytical position of L2 is recovered according to Equation 2.60;

4. use that position as a guess to numerically solve the equation providing the correct coordinate of L2, then used to compute C_2;

5. initialization of a loop on the longitude θ;

6. for each value of θ compute

$$\begin{cases} x = r\cos\theta \\ y = r\sin\theta \end{cases}$$

with r being the adimensional radius of Ryugu. Use together x, y and β to find $C = -2U(x, y, \beta)$;

7. recover v_{ej} according to Equation 3.3.

The two nested cycles will scan all the possible $r_P - \theta$ combinations, having $78.5 \ \mu m \leq r_P \leq 10$ mm (see Figures 2.14 and 2.15) and $0° \leq \theta \leq 360°$. A contour of the result is depicted in Figure 3.1.
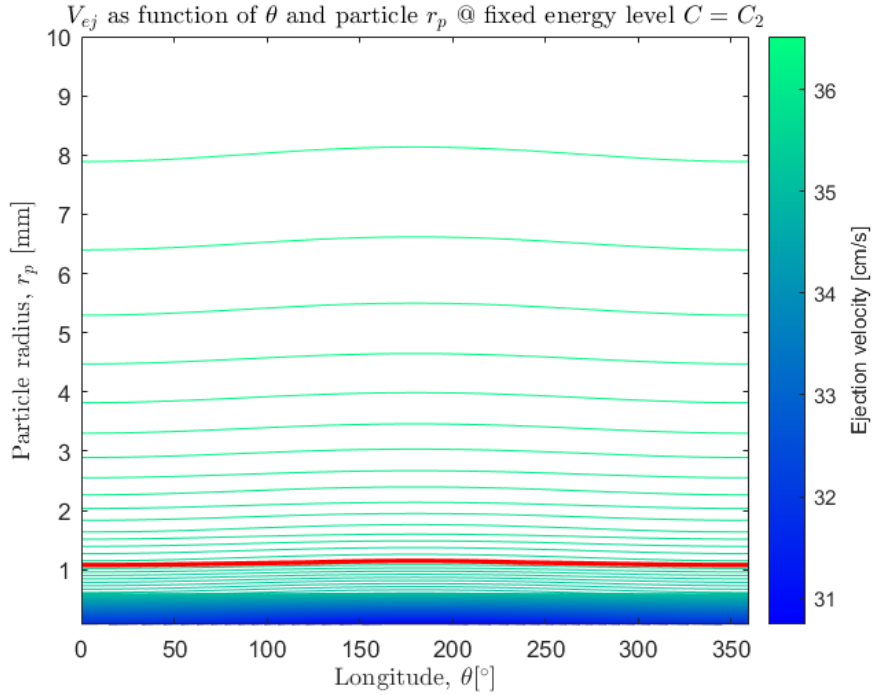
Figure 3.1: Contour plot of particles' ejection velocity as function of their size and ejection site longitude.

It is interesting to note that for the same v_{ej}, the corresponding particle's size reaches its maximum around $\theta = 180°$. Furthermore, fixing v_{ej}, i.e. following a contour line, bigger particles will re-impact while smaller ones can potentially escape. This is in accordance with theory and is particularly well explained by Figure 3.2. Fixing $v_{ej} = 35.59$ cm/s, represented by the red line in Figure 3.1, and $\theta = 0$, the energy associated with a particle on Ryugu's soil and to L2 have been recovered for increasing values of ejecta sizes. The graph shows how, as r_P increases, the difference $E_2 - E$ passes from being negative

(i.e. $E > E_2$) to be positive (i.e. $E < E_2$). As previously explained (see Figure 2.6), whenever $E < E_2$ the ZVC bottleneck at L2 closes. This, therefore, explains that for fixed ejection velocity and position, bigger particles surely will not escape from the system. Furthermore, in this example, $E = E_2$ for $r_P \simeq 1.05715$ mm, corresponding to the region just above the red line shown in the contour plot. Thus, by fixing v_{ej}, the plot will be divided into two regions: for the upper one, the ZVC will be closed while, for conditions falling in the lower region, the particles can potentially escape.
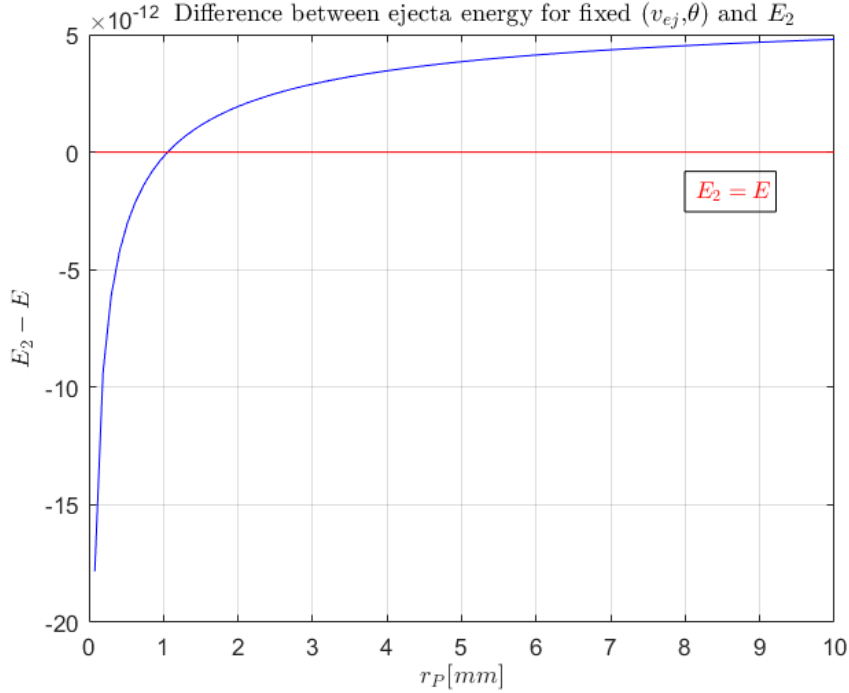
Figure 3.2: Difference between E_2 and E for increasing particles' size, keeping fixed ejection velocity and longitude.

However, Equation 3.3 is an expression that does not consider the asteroid's rotational contribute. Defining as ω_{rot} the rotational velocity of Ryugu around its z-axis and ω_{rev} the revolutionary velocity of Ryugu, i.e. the one with which the asteroid rotates around the Sun, the expression of the velocity is transformed into:

$$v_0^2 = v_{ej}^2 + \|\boldsymbol{\Omega} \times \boldsymbol{r}\| = v_{rad}^2 + \left(\frac{\omega_{rot}}{\omega_{rev}}r\right)^2 \tag{3.4}$$

where r is the asteroid's adimensional radius, $\boldsymbol{\Omega}$ is the vector $[0\ 0\ \omega_{rot}/\omega_{rev}]$ and $\boldsymbol{r} = [r\cos\theta\ r\sin\theta\ 0]$.

Applying this, Equation 3.3 becomes:

$$v_{ej}^2 + \left(\frac{\omega_{rot}}{\omega_{rev}}r\right)^2 = C(x, y, \beta) - C_2 \implies v_{ej} = \sqrt{C(x, y, \beta) - (\frac{\omega_{rot}}{\omega_{rev}}r)^2 - C_2} \qquad (3.5)$$

This discussion allows to comprehend that velocity will no longer be perfectly radial, since the asteroid's rotation will deflect its direction. Calling therefore γ the angle between the local normal direction $\hat{\boldsymbol{n}}$ and the velocity direction, following Latino et al. [1], it is possible to retrieve the initial velocity expressed in the cartesian frame as stated in Equation 3.6.

$$\boldsymbol{v_0} = \begin{bmatrix} v_\gamma \cos(\gamma + \theta) - v_\omega \sin\theta \\ v_\gamma \sin(\gamma + \theta) + v_\omega \cos\theta \\ 0 \end{bmatrix} \qquad (3.6)$$

with

$$\begin{cases} v_\omega = \dfrac{\omega_{rot}}{\omega_{rev}}r \\ v_\gamma = -v_w \sin\gamma + \sqrt{v_\omega^2 \sin^2\gamma + v_{ej}^2} \end{cases} \qquad (3.7)$$

This dissertation gives the possibility to add to the v_{ej} portrayed in Figure 3.1 the asteroid's rotation contribute. The aim now, is to compute all the trajectories arising from the initial conditions coming from the nested cycles on r_P, θ and γ. The equations of motion to be integrated are the ones reported in 2.58 and the propagation of each IC is then stopped whenever the particle hits again the surface of Ryugu or whenever it goes outside the Hill's region, i.e. for $r \leq r_{Ryugu}$ and $r \geq r_{Hill} = \left(\dfrac{\mu}{3}\right)^{(1/3)}$ respectively. When these occurrences are spotted, by means of an event function, two cases have to be distinguished:

1. if the particle is escaped from the system, the iteration stops and the next one begins;

2. if the particle has hit once again Ryugu's surface, then the bouncing behavior has to be studied.

Therefore, the discussion will now focus on the second case here highlighted. Firstly, it is important to introduce the *restitution coefficient*, which is defined as the ratio between the relative velocities of two colliding bodies after and before the impact. In this case, however, one of the bodies is the asteroid, which represents an immovable surface to the particle. Therefore, the restitution coefficient is just

$$e = \frac{v_f}{v_0} \qquad (3.8)$$

being v_f the particle velocity after the impact and v_0 the one right before. Moreover, from this definition it is possible to understand how, due to energy dissipation occurring throughout any collision, it is always true that $0 \leq e \leq 1$. Of course, re-impacts will likely occur at oblique angles, meaning that there is the necessity of identifying two separate coefficients, reported in Equation 3.9. In the relation, e_n represents the normal restitution coefficient, while e_t is the tangential.

$$\begin{cases} e_n = \dfrac{v_{nf}}{v_{n0}} \\ e_t = \dfrac{v_{tf}}{v_{t0}} \end{cases} \tag{3.9}$$

In particular:

- $0 \leq e_n < 1$, with 0 indicating a completely anelastic collision and 1 being the theoretical value representative of a completely elastic collision. However, usually e_n is found to be < 0.6.

- $-1 \leq e_t \leq 1$, where -1 means complete tangential reversal, 0 is associated with complete damping and 1 implies tangential decoupling.

Following Kikuchi et al. [17] however, it is possible to define other two parameters, called *impulse ratio (ζ)* and *critical impulse ratio (ζ^*)*, defined as follows:

$$\begin{cases} \zeta = \dfrac{1 - e_t}{1 + e_n} \tan \alpha \\ \\ \zeta^* = \dfrac{\tan \alpha}{(1 + \dfrac{mr_P^2}{I})(1 + e_n)} \xrightarrow[\text{assuming spherical particles}]{(I = \frac{2}{5}mr_P^2)} \zeta^* = \dfrac{\tan \alpha}{\dfrac{7}{2}(1 + e_n)} \end{cases} \tag{3.10}$$

with α begin the impact angle. Quoting the same paper, it is always true also that $\zeta \leq \zeta^*$. This restricts the possible impact angles that, specifically, shall guarantee [17]:

$$\begin{cases} A_{RB} = \{\alpha \in \mathbb{R} | 0 \leq \zeta(\alpha) \leq \zeta^*(\alpha)\} \\ A_{PM} = \{\alpha \in \mathbb{R} | 0 \leq \zeta(\alpha) \leq 1\} \end{cases} \tag{3.11}$$

An impact angle too high or too small would mean, in fact, almost-normal or almost-tangential collisions, therefore likely leading to rolling or frontal impact respectively, both unlikely to result in rebounds. Moreover, the previous formulations are related to the *rigid*

body (RB) and *point mass (PM)* approximations. The former is obtained by applying the rigid-body theory, but this is reasonable only for a first-step analysis. In fact, this does not allow taking into account tangential compliance which would result in elastic deformation, finally affecting ζ^*. For this reason, also the point mass approximation is given since, not requiring the rigid-body assumption, it leads to a more conservative formulation. Spanning through a set of *alpha*, Kikuchi recovered the feasible impact angles, i.e. the ones verifying relation 3.11. This procedure has been followed for both the artificial landmarks, called *target markers (TM)* deployed with success on Ryugu during the Hayabusa2 mission. From here on they will be referred to as TDM1 and TDM2, the former being representative of surface material, while the latter being representative of subsurface material brought out by the small carry-on impact [16][17]. Apart from that, the main distinction between them is the site they targeted, shown in Figure 3.3.
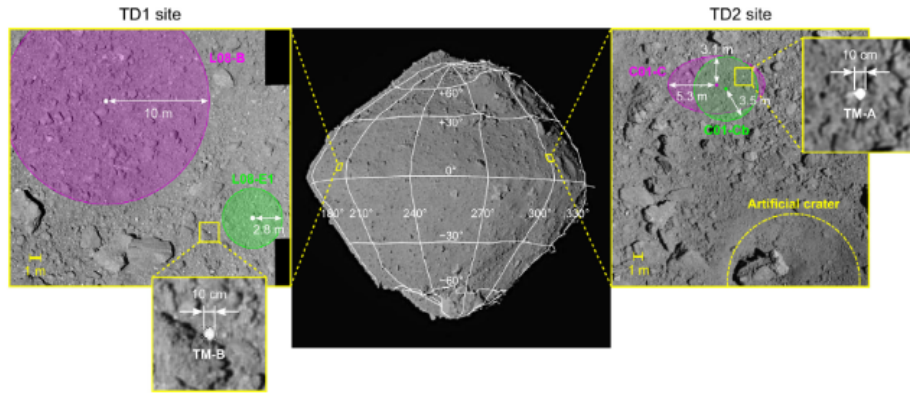
Figure 3.3: Target sites for the TDMs of the Hayabusa2 mission [17].

The results that Kikuchi found are reported in Figures 3.4 and 3.5, both for rigid body and point mass cases.

As can be seen, in both cases, the rigid body model provides a wider range of feasible impact angles. This is strictly related to the realms defined by Equation 3.11, reflecting the more conservative nature of the point mass model.

Furthermore, the values shown in these figures are then used to perform an interpolation exploiting the *Matlab* commands *polyfit* and *polyval*: the polynomial coefficients found in this way will enable to compute, at each impact, the approximated e_n and e_t for the impact angle of that specific collision if, of course, it is inside the feasible range. However, this procedure requires imposing the order n_{ord} which approximates the trend of the function to be interpolated. Thus, in order to obtain the best possible results, n_{ord} has been made to vary between 1 and n_{max}, where n_{max} represents the maximum order suitable for the interpolation, beyond which the polynomial arising results undetermined or poorly
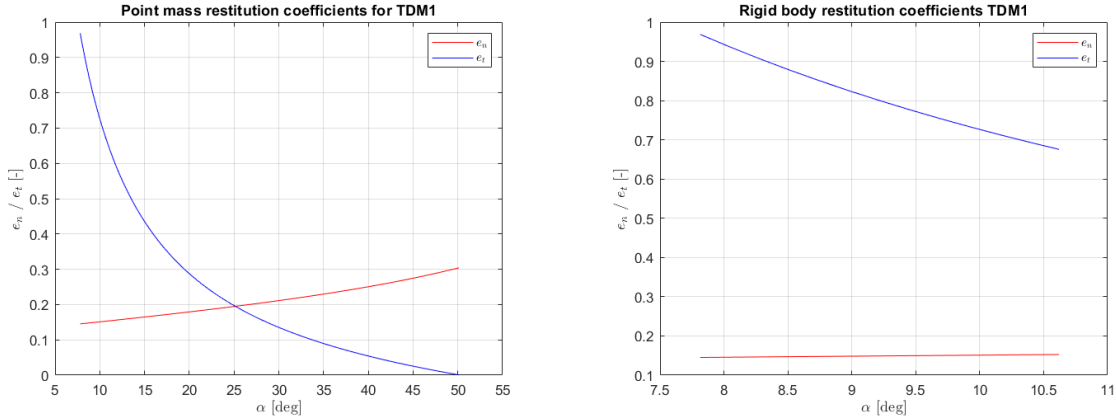
Figure 3.4: Restitution coefficients for TDM1, applying the point mass model (left) and the rigid body assumption (right).
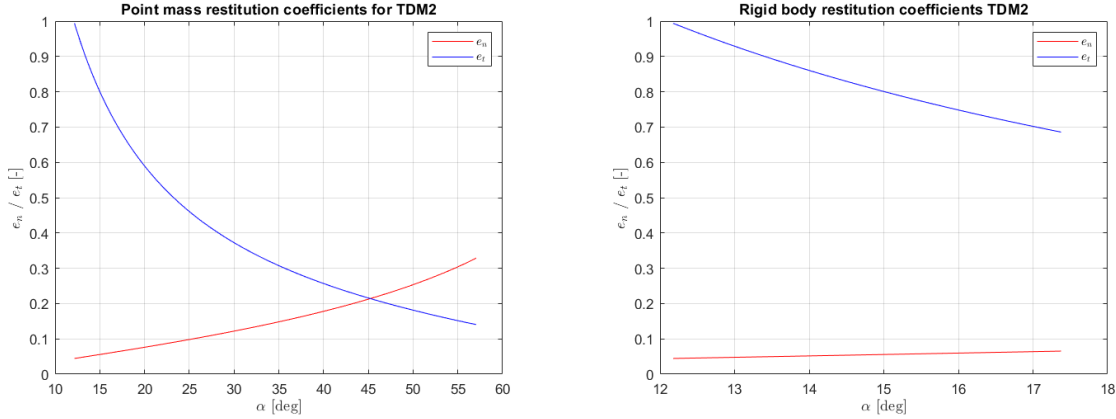
Figure 3.5: Restitution coefficients for TDM2, applying the point mass model (left) and the rigid body assumption (right).

conditioned. In particular, its value depends on the number of nodes provided by Kikuchi et al. [17]. The trends of the error on e_n and e_t, for both rigid body and point mass models, are shown in Figures 3.6 and 3.7. These show only the case of TDM1, while the one associated with TDM2 has been omitted for sake of brevity. However, the conclusions are the very same for both the TDMs.

As can be already seen from the pictures, the error tends to drop for increasing values of n_{ord}, as confirmed by the study of the *minimum squared distance (msd)* computed for each interpolation order. Concluding, this dissertation is able to provide the best orders of interpolation for the data available, and these are reported in table 3.1. This highlights how e_t will be approximated worse than e_n in all the cases. Furthermore, the table underlines that, in the case of rigid body, the coefficients are better estimated: this is due to the higher ratio between the number of data given and the range of the suitable

impact angles provided.
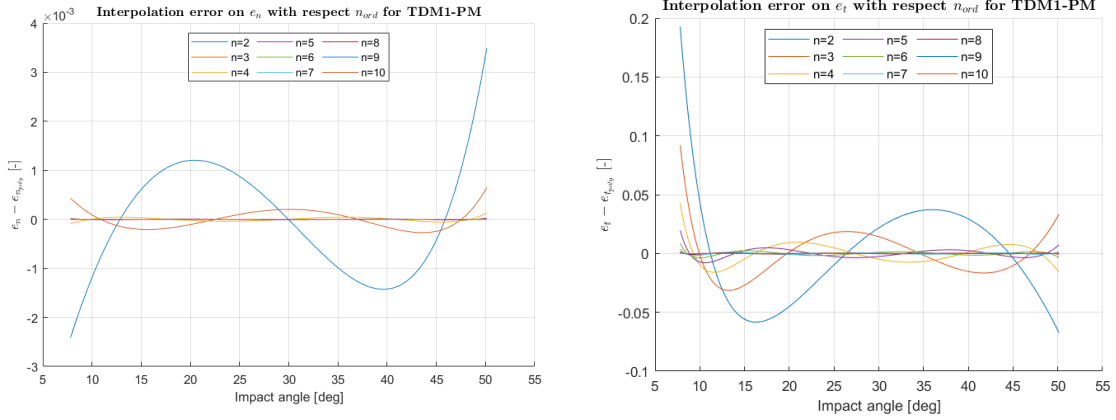
Figure 3.6: Error committed on e_n (left) and e_t (right) due to the interpolation applied to the TDM1-PM case.
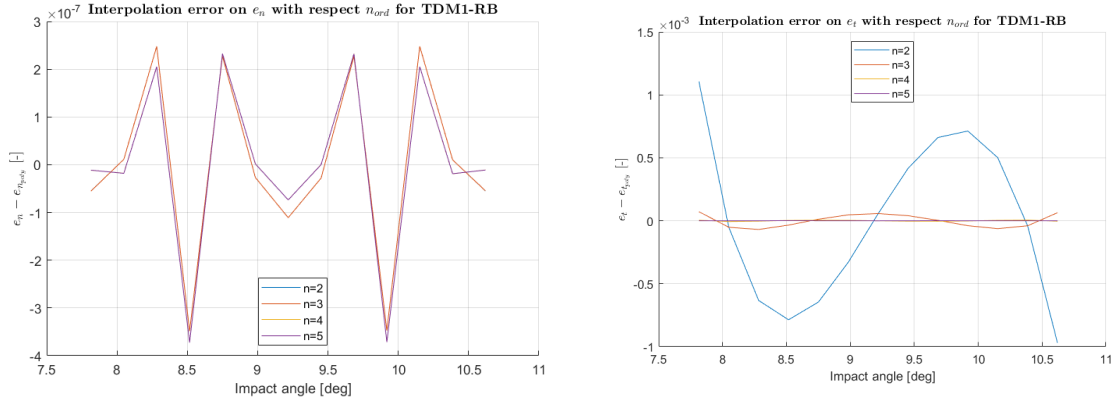
Figure 3.7: The error committed on e_n (left) and e_t (right) due to the interpolation applied to the TDM1-RB case.

Once characterized with this approach the restitution coefficients, which reproduce the damping occurring during a collision, the bouncing behavior can be analyzed. Of course, there will be the necessity of differentiating between ejecta that, once collided with Ryugu's surface, are actually bouncing back to orbit around the asteroid with those that start rolling on its soil, basically landing on it. To achieve this, two approaches are possible. The first one, proposed by Raducan et al. [39], is to impose a minimum velocity threshold after the impact. The second method, proposed by Yu et al. [40], is instead to fix a height beyond which the rebounding particle can be considered to actually bounce rather than roll. This method was the one selected for this work, applied by means of the energetic balance shown in Equation 3.12. The particle is considered to bounce if, when the energy is completely transformed into potential energy, the altitude with respect

TDM	Model	n_{ord}	msq_{e_n}	msq_{e_t}
TDM1	PM	10	$1.5474 \cdot 10^{-11}$	$6.4770 \cdot 10^{-07}$
TDM2	PM	10	$4.2685 \cdot 10^{-11}$	$5.4987 \cdot 10^{-08}$
TDM1	RB	5	$4.7519 \cdot 10^{-13}$	$1.6428 \cdot 10^{-12}$
TDM2	RB	5	$4.0090 \cdot 10^{-12}$	$2.9390 \cdot 10^{-11}$

Table 3.1: Table summarising the interpolation quality. The first row refers to the TDM considered, the second to the model applied, the third reports the best interpolation order ($n_{ord} = n_{max}$ in all the cases), fourth and fifth columns show the minimum squared distance on e_n and e_t respectively.

asteroid's surface is larger than the threshold chosen.

$$\frac{1}{2}v_n^2 = \frac{1}{2}\cancel{v_{nf}^2} + gh \implies h = \frac{v_n^2}{2g} \tag{3.12}$$

The possibilities are then:

- $h > l_{threshold}$, the particle goes back into orbit. New ICs are generated and the propagation is carried on until the next event or the end of the time window considered.

- $h < l_{threshold}$, the particle lands on the asteroid. Simulation stops and the next iteration begins.

The value of $l_{threshold}$ should be reasonably low, and is set in this case to 10 cm [1].
The next step required to implement the whole is to understand how to rotate from the cartesian frame $\{\boldsymbol{i}, \boldsymbol{j}, \boldsymbol{k}\}$ to the local tangent-normal frame $\{\boldsymbol{t}, \boldsymbol{n}, \boldsymbol{k}\}$: this is needed since the former is the frame in which the equations of motion are expressed and thus propagated, while the latter is required since the restitution coefficients are expressed through normal and tangential velocity components. To reach this goal, first ξ, the angle between $\boldsymbol{i}$ and $\boldsymbol{t}$ shall be computed. In particular, its expression changes depending on the longitude at which the impact occurs. They are shown in Figure 3.8 for each quarter.

Recovered ξ, this can be used to rotate the impact velocity obtained by the propagation, and therefore expressed in the cartesian frame, to the local tangent-normal frame. Mathematically:

$$\boldsymbol{R} = \begin{bmatrix} \cos\xi & \sin\xi & 0 \\ -\sin\xi & \cos\xi & 0 \\ 0 & 0 & 1 \end{bmatrix} \tag{3.13}$$
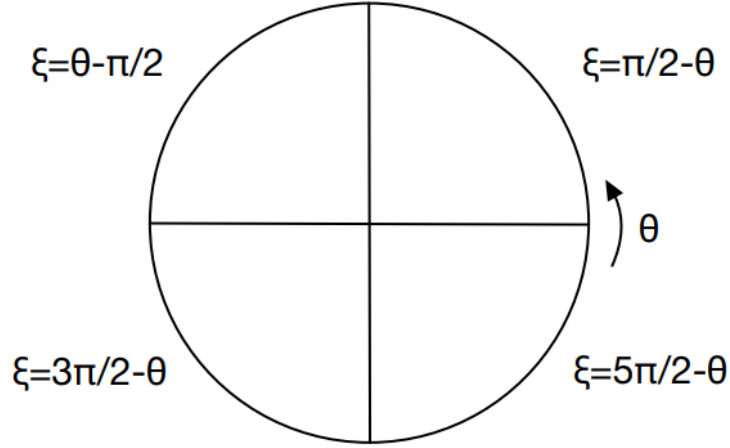
Figure 3.8: The different relations between ξ and θ depend on the quadrant where the particle impacts.

$$v_{tn} = R\ v_{ij} \tag{3.14}$$

Of course, matrix R shown in Equation 3.13 can be used to pass from cartesian to local frame and vice versa.

Once expressed the velocity in the $\{t, n\}$ frame, it is possible to apply on it the dissipation by means of the restitution coefficients. In particular, the velocity after the collision, expressed in the local frame, can be computed as stated by Equation 3.16.

$$E = \begin{bmatrix} e_t & 0 & 0 \\ 0 & -e_n & 0 \\ 0 & 0 & -1 \end{bmatrix} \tag{3.15}$$

$$v_{E_{tn}} = E\ v_{tn} \tag{3.16}$$

When $v_{E_{tn}}$ is retrieved, its component along the normal direction will be known, enabling to exploit relation 3.12 to understand the bouncing behavior. In the case in which the particle actually bounces back in orbit, according to the threshold height established, the damped velocity vector found through Equation 3.16 can be then rotated back to cartesian frame $v_{out} = R^T\ v_{E_{tn}}$. To this value, the asteroid's rotational contribution must be added, following the previous dissertation, thus obtaining the new initial conditions for the propagation of the post-rebound trajectory.

The whole procedure here above described is iterated, by means of three nested cycles, on

particle size r_P, longitude θ, and ejection angles γ. However, for clarity, the code block diagram has been reported in Appendix A.

As done by Latino et al. [1], the results are then stored in a table having nine columns forming in this way a database describing the ejecta dynamics and fate. An example of it is shown in Table 3.2. This will enable not only to manage easily the information found but also gives the opportunity to "search" for specific initial conditions and directly recover the final state without any further process or integration.

r_P [mm]	θ [°]	v_{ej} [cm/s]	γ [°]	θ_{imp} [°]	v_{imp} [cm/s]	γ_{imp} [°]	tof [days]	Condition
...	...	...	...	...	...	...	...	...

Table 3.2: Basic scheme of the database built.

In the so-built database, *tof* highlights the time of flight of that particular trajectory: this value will be equal to the maximum time window imposed whenever none of the events occur, i.e. if the particle is still on-orbit around the asteroid after the prescribed maximum time that, in this case, has been fixed to 90 days. The column *Condition*, instead, will highlight the final fate of that particular trajectory. The possible options are the following:

- *Escape*: the ejecta particle has been able to escape from the system through the L2 bottleneck.

- *Impact*: after orbiting around the asteroid for a timespan equal to tof, the ejecta particle hit on Ryugu's surface, with an impact angle within the feasible range.

- *OutRange*: after orbiting around the asteroid for a timespan equal to tof, the ejecta particle hit on Ryugu's surface, with an impact angle outside the feasible range. The particle here is considered as landed on the surface, unable to bounce back into orbit.

- *Orbit*: in this case $tof = t_{max}$, therefore ejecta has orbited around the asteroid without impact again on it or escape from the system. In this case, the ejecta is assumed to be still in orbit around Ryugu.

- *Escape$_{reb}$*: the ejecta particle has been able to escape from the system through the L2 bottleneck after a previous collision with Ryugu and consequent rebound.

- *Impact$_{reb}$*: after a collision with Ryugu and a consequent rebound, the particle has been orbiting around the asteroid for a timespan equal to tof before hitting again Ryugu's surface, with an impact angle within the feasible range.

- *OutRange$_{reb}$*: after a collision with Ryugu and a consequent rebound, the particle has been orbiting around the asteroid for a timespan equal to tof before hitting again Ryugu's surface, with an impact angle outside the feasible range.

- *Orbit$_{reb}$*: after a collision with Ryugu and a consequent rebound, the ejecta has orbited for $tof = t_{max}$ without impacting again on the asteroid's surface or escaping from the system. Also in this case, the ejecta is assumed to be still in orbit around Ryugu.

According to the discussion relative to Figures 2.14 and 2.15, the particle size has been made to vary from $78.5 \mu m$ to 10 mm. Following Trisolini et al. [2], γ has been considered to range from $-65°$ to $-25°$ and from $25°$ to $65°$ (see Figure 3.9). Finally, θ has been discretised once per degree, going from $0°$ to $360°$.
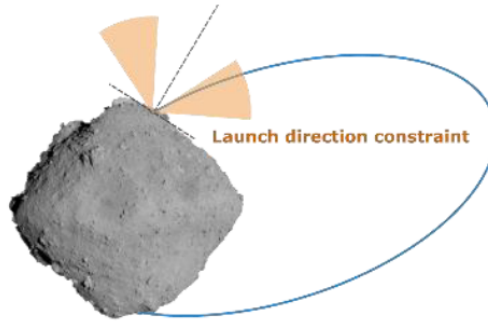
Figure 3.9: Orange regions identify the range of possible γ [2].

Knowing that Latino et al., in their work [1], considered e_t and e_n as constants, in the order, equal to 0.714 and 0.6, it is now possible to investigate what are the differences arising exploiting the new approach previously described to recover the coefficients of restitution. In particular, Figure 3.10 returns a global view about the sample trajectories distribution within the different categories. For sake of brevity, this is just shown for the case of TDM1 and PM model.

Of course, the first trivial observation regards the categories *OutRange* and *OutRange$_{reb}$*: since in [1] is not imposed any boundary to the impact angles suitable for rebound, when
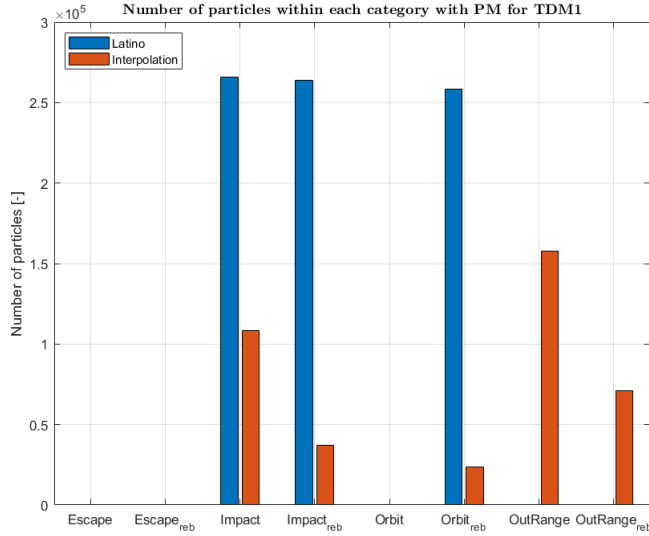
Figure 3.10: Comparison between sample trajectories fate applying Latino and Kikuchi's approaches.

studying the dynamics through this approach these categories will be empty. Another interesting point concerns the number of bouncing occurring for these simulations. With Latino's method, in fact, the sample trajectories arising from a rebound are found to be 522349, way higher than the 131853 recovered interpolating the data coming from Kikuchi et al. as proposed in this work. Such a trend is a direct consequence of the fact that, for Latino, any rebound is considered to be possible. Furthermore, the restitution coefficients used by Latino et al. are way higher, especially for e_n, than those retrieved in the PM case of Figure 3.4. This, at the end, returns a lower energy dissipation during a collision, leading to more particles having velocity enough to bounce again from Ryugu after the impact: as visible from the figure, the outcome is that almost all the *Impact* trajectories are followed by a successful rebound. Moreover, it can be seen that the three populated categories for Latino's scenario present almost the same amount of samples, meaning that a large part of the trajectories falling into the $Impact_{reb}$ lead to a particle injected in orbit around Ryugu after a second rebound. To be more precise, of the 263728 trajectories in $Impact_{reb}$, about the 98% drives to an orbit after a second rebound: once again, this underlines how the damping assumed by this scenario is not realistic. Moreover, $Impact_{reb}$ is the only category filling $Orbit_{reb}$, in which no trajectories are found to directly arrive from the *Impact* category. All these analysis explicate the necessity of introducing the novel approach proposed.

However, the results obtained in this way are totally unsatisfactory from the on-orbit collection viewpoint. As can be seen from Figure 3.10, in fact, even with the new approach,

no particles are found able to escape from the system, resulting in the conclusion of an unfeasible collection strategy for the kind of mission treated. For this reason, the next step is to expand the study to the halo region rather than strictly to the lagrangian point itself, enlarging the region of interest of the work. This means change the reference energetic level chosen during the dissertation that concluded with Figure 3.1, referring v_{ej} no longer to C_2 but to a $C' < C_2$. Thus, the analysis of halo orbits and particularly of periodic orbits in the neck region becomes crucial for the development of the work, and will be discussed in the next chapter.

4 | Calculation of periodic orbits

Once understood the trends for the ejecta dynamics, the next step is to recover the so-called Halo Orbits, which are the orbits where the spacecraft shall be injected in order to perform the actual collecting mission. This can be found by studying the linearised dynamics close to the libration point of interest. Due to the existence of the integral of motion, these periodic orbits can be grouped in one-parameter families, each one containing a simple infinity of periodic orbits and symmetric to the x-axis [27]. This, can be easily understood by analysing Equation 2.41. Remaining into the planar case (i.e. $z = \dot{z} = 0$), in fact, it is trivial to understand that, once fixed gamma, there will be a given $\dot{y}$ for each x. This is guaranteed by the knowledge that $\dot{y} > 0$ ([41], Figure 2). The planar hypothesis will be assumed from here on since, even though not rigorous, simplifies the dissertation carried on without threaten the validity and the results of the discourse. Moving forward, there are five main families of periodic orbits to be distinguished. They are [27][42]:

- a, which originates around L2 and presents a close approach to the second primary. Since, as previously reported, including the SRP perturbation will shift L_1 towards the biggest primary and L_2 closer to the asteroid, L_2 will be the most adapt to perform a collection such as the one thought for this work: this family will be therefore the main focus of this thesis;

- c, unstable-retrograde orbits originating around L1;

- f, family of stable retrograde orbits around the secondary primary;

- g, family of direct orbits around the smaller primary, presenting a double close approach with it;

- g' and g'', stable-unstable direct orbits which bifurcate from g.

However, the research of such periodic orbits is far from being trivial, especially since the initial conditions are hard to be recovered from and the problem is very stiff and IC-sensitive. The first consideration to be done is linked with the periodicity conditions. Analysing, in fact, Hill's equations (Equation 2.42), it comes out that the system presents

the symmetric relation state in Equation 4.1. This defines the so-called *Mirror configuration* [42]. The outcome of this is that, for a periodic orbit lying on the xy-plane with $y_0 = 0$, it must hold that $\dot{x}_0 = 0$. Therefore, the initial condition will show the form reported in expression 4.2.

$$(x, y, t) \longrightarrow (x, -y, -t) \tag{4.1}$$

$$\boldsymbol{x_0} = \begin{bmatrix} x_0 & 0 & 0 & \dot{y}_0 \end{bmatrix} \tag{4.2}$$

Once assessed, the main approach to obtain approximated ICs is to use the third-order expansion proposed by Richardson in 1979 [43]. The idea here is to recover a third-order analytical solution for the periodic motion around the collinear points. Another technique following the work of Richardson is the polynomial approach proposed by Kim [44], in which the third-order approximation of the ICs is then reformulated as polynomials by means of MATLAB functions such as *polyfit* and *polyval*. Kin stated that for Halo, in fact, polynomial expressions lead to more accurate computations also quicker to drive to convergence. However, since this work is discussing only the planar case, good initial conditions can be already found in Henon [27] or in Kalantonis [45]. These, will be then refined by means of a variational approach, through the so-called *differential correction* method.

4.1. Differential Correction to refine the initial conditions

A differential correction method can be used to improve the initial conditions to be then integrated. Recalling Equation 2.47, it is possible to write:

$$\begin{cases} \ddot{x} - 2\dot{y} = W_x(x, y, \beta) \\ \ddot{y} + 2\dot{x} = W_y(x, y, \beta) \end{cases} \tag{4.3}$$

with $W = \dfrac{3x^2}{2} + \dfrac{1}{r} + \beta x$.

Defining the new set of variables reported in 4.4, the equations of motion of the problem can be written as stated by Equation 4.5.

$$\begin{cases} x = x_1 \\ y = x_2 \\ \dot{x} = x_3 \\ \dot{y} = x_4 \end{cases} \tag{4.4}$$

$$\dot{x}_i = f_i(x_1, x_2, x_3, x_4) \qquad\qquad i = 1, ..., 4$$

$$\begin{cases} f_1 = x_3 \\ f_2 = x_4 \\ f_4 = 2x_4 - \dfrac{x_1}{r^3} + 3x_1 + \beta \\ f_5 = -2x_3 - \dfrac{x_2}{r^3} \end{cases} \tag{4.5}$$

with $r = (x_1^2 + x_2^2)^{(1/2)}$.

Let now the term $\phi(\boldsymbol{x}, t)$ represent a solution of Equation 4.5, it is possible to write $\phi(\boldsymbol{x}, 0) = \boldsymbol{x_0}$, i.e. $\phi(\boldsymbol{x}, 0)$ can be seen as an initial condition for a periodic orbit. This term represents the *flow* of the system, which can be used to map how perturbation on the initial conditions will affect the state at $t = t_f$. If the displace trajectory passes close to the reference one, it is then possible to perform a linearisation of the flow as follows:

$$\phi(\boldsymbol{x_0} + \delta\boldsymbol{x_0}, t) \simeq \phi(\boldsymbol{x_0}, t) + \frac{\partial\phi}{\partial\boldsymbol{x_0}}(\boldsymbol{x_0}, t)\delta\boldsymbol{x_0} \tag{4.6}$$

As previously said, ϕ can map the perturbations up to the final state, meaning that:

$$\boldsymbol{x} + \delta\boldsymbol{x} = \phi(\boldsymbol{x_0} + \delta\boldsymbol{x_0}, t) \tag{4.7}$$

Substituting Equation 4.7 into 4.6, and recalling that by definition $\boldsymbol{x} = \phi(\boldsymbol{x_0}, t)$, it is possible to obtain relation 4.8.

$$\delta\boldsymbol{x} = \frac{\partial\phi}{\partial\boldsymbol{x_0}}(\boldsymbol{x_0}, t)\delta\boldsymbol{x_0} \tag{4.8}$$

In Equation 4.8 the term $\frac{\partial\phi}{\partial\boldsymbol{x_0}}(\boldsymbol{x_0}, t)$ is a matrix representing the Jacobian of the flow. It takes the name of *State Transition Matrix* ($\boldsymbol{\Phi}$) and can be used to correct the guess on the initial state for a periodic orbit. Furthermore, for $t = T$, the state transition matrix

is called instead *Monodromy matrix.* This is of particular importance since it, by means of its eigenvalues, rules the stability of the periodic orbit that it describes. Specifically, since the system is autonomous, there will be two unit eigenvalues and the rest forming reciprocal pairs [15]: a periodic orbit will be stable if all its eigenvalues are situated on the unit circle. In particular, introducing the parameters k_i computed from the eigenvalues of the monodromy matrix (λ_i in Equation 4.9), the periodic orbit will be stable if k_i is real and $|k_i| < 2$. This is known as the *Broucke's stability condition* [15][31].

$$k_i = \frac{1}{\lambda_i} + \lambda_i \quad \text{with} \quad i = 1, 2 \tag{4.9}$$

In addition to this, its properties can be exploited to verify if the variational equations have been well written and propagated. The monodromy matrix, in fact, not only must present two unit eigenvalues, but also its determinant must be unitary as well. Then, the monodromy matrix must also be symplectic, i.e. it shall grant the relations reported in Equation 4.10.

$$\boldsymbol{\Phi}^{*T} \begin{pmatrix} \boldsymbol{0}_{2\times 2} & \boldsymbol{I}_{2\times 2} \\ \boldsymbol{-I}_{2\times 2} & \boldsymbol{0}_{2\times 2} \end{pmatrix} \boldsymbol{\Phi}^{*} = \begin{pmatrix} \boldsymbol{0}_{2\times 2} & \boldsymbol{I}_{2\times 2} \\ \boldsymbol{-I}_{2\times 2} & \boldsymbol{0}_{2\times 2} \end{pmatrix} \tag{4.10}$$

with

$$\begin{pmatrix} \boldsymbol{I}_{2\times 2} & \boldsymbol{0}_{2\times 2} \\ \boldsymbol{-\Omega} & \boldsymbol{I}_{2\times 2} \end{pmatrix} \boldsymbol{\Phi}(t, 0) \begin{pmatrix} \boldsymbol{I}_{2\times 2} & \boldsymbol{0}_{2\times 2} \\ \boldsymbol{\Omega} & \boldsymbol{I}_{2\times 2} \end{pmatrix} = \boldsymbol{\Phi}^{*} \tag{4.11}$$

$$\boldsymbol{\Omega} = \begin{bmatrix} 0 & 1 \\ -1 & 0 \end{bmatrix} \tag{4.12}$$

All these properties (and the constancy of the Jacobi constant within the same propagation) have been verified, proving the validity of the work done.

Making a step forward, hereafter the procedure to correct the initial conditions generating a periodic orbit will be explained.

First, considering an initial guess $\boldsymbol{x} = [x_0\ 0\ 0\ y_0]$, the trajectory is propagated for half the orbital period. This, can be recovered through two different approaches:

1. Implement an event function able to stop the integration whenever $y = 0$ for the first time after the initial condition. This, named *Lindstend-Poincarè* technique, identifies the so-called *Poincarè map* or *first-return map* [44], and the time for which this occurs defines the semi-period of the orbit.

2. The period of known periodic orbits can be found in literature and therefore can be provided as the initial guess for the propagation time span.

In this work, the second option has been followed. Due to periodicity constraints, when the trajectory crosses again the y-axis, it must be perpendicular to it, maintaining therefore the form $\boldsymbol{x} = [\tilde{x}\ 0\ 0\ \tilde{v}_y]$. However, in general, for $T = T_{1/2}$, the resulting state will have $\tilde{v}_x \neq 0$, therefore $\boldsymbol{\phi}(\boldsymbol{x}, T_{1/2}) = [\tilde{x}_f\ 0\ \tilde{v}_x\ \tilde{v}_y]$. At this point, since, as stated before, ϕ is a solution of Equation 4.5, it will hold that

$$\frac{\partial \boldsymbol{\phi}(\boldsymbol{x}, t)}{\partial t} = \boldsymbol{f}(\boldsymbol{\phi}(\boldsymbol{x}, t)) \tag{4.13}$$

Analysing then a first-order expansion of the flow map, expressed as reported in Equation 4.14, on the right hand side it is possible to recognize both $\boldsymbol{\Phi}$ and $\boldsymbol{f}_i$ (the terms in the squared brackets in Equation 4.14). Therefore, the relationships arising from the linearisation is the one expressed in Equation 4.15.

$$\boldsymbol{\phi}(\boldsymbol{x} + \delta\boldsymbol{x}, T_{1/2} + \delta t) = \boldsymbol{\phi}(\boldsymbol{x}, T_{1/2}) + \left[\frac{\partial \boldsymbol{\phi}(\boldsymbol{x}, T_{1/2})}{\partial \boldsymbol{x}}\right]\delta\boldsymbol{x} + \left[\frac{\partial \boldsymbol{\phi}(\boldsymbol{x}, T_{1/2})}{\partial t}\right]\delta t \tag{4.14}$$

$$\begin{bmatrix} \bar{x} \\ 0 \\ 0 \\ \bar{v}_y \end{bmatrix} = \begin{bmatrix} \tilde{x} \\ 0 \\ \tilde{v}_x \\ \tilde{v}_y \end{bmatrix} + \boldsymbol{\Phi}(\boldsymbol{x}, T_{1/2}) \begin{bmatrix} \delta x \\ 0 \\ 0 \\ \delta v_y \end{bmatrix} + \boldsymbol{f}(\boldsymbol{x}, T_{1/2})\delta t \tag{4.15}$$

Rearranging this relation and considering just the second and third rows, the system will result in [42] [46]:

$$\begin{cases} \Phi_{21}\delta x + \Phi_{24}\delta v_y + f_2\delta t = 0 \\ \Phi_{31}\delta x + \Phi_{34}\delta v_y + f_3\delta t = -\tilde{v}_x \end{cases} \tag{4.16}$$

As can be easily deduced, this relation presents three unknowns in two equations, leading to an indeterminate system: this agrees with theory, of course, since the family that will come out will be then parameterised by one parameter, i.e. the one that is chosen to keep fixed. Imposing $\delta x = 0$, the corrective terms can be recovered as:

$$\begin{bmatrix} \delta v_y \\ \delta t \end{bmatrix} = \begin{bmatrix} \Phi_{24} & f_2 \\ \Phi_{34} & f_3 \end{bmatrix}^{-1} \begin{bmatrix} 0 \\ -\tilde{v}_x \end{bmatrix} \tag{4.17}$$

Thus, the new IC will be $\boldsymbol{x_0} = [\tilde{x}_0 \ 0 \ 0 \ \tilde{v}_y + \delta v_y]$ while $T_{half} = T_{half} + \delta t$. This procedure will iterate until $\tilde{v}_x < tol$.

The point still open is how to compute the state transition matrix. Even though approaches exploiting finite differences techniques have been developed, these are not suitable for the computational recovery of periodic orbits. The *variational approach* is instead the one used in this field, and will be explained hereafter. Taking the first order expansion of $\boldsymbol{f}$ with respect to $\boldsymbol{x}$, it will result that:

$$\dot{\boldsymbol{x}} = \boldsymbol{f}(\boldsymbol{x}^*, t) + \frac{\partial \boldsymbol{f}(\boldsymbol{x}^*, t)}{\partial \boldsymbol{x}}(\boldsymbol{x} - \boldsymbol{x}^*) \tag{4.18}$$

Defining the displacement as $\delta\boldsymbol{x} = \boldsymbol{x} - \boldsymbol{x}^*$, it will hold that

$$\delta\dot{\boldsymbol{x}} = \dot{\boldsymbol{x}} - \dot{\boldsymbol{x}}^* \longrightarrow \dot{\boldsymbol{x}} = \dot{\boldsymbol{x}}^* + \delta\dot{\boldsymbol{x}} \tag{4.19}$$

Replacing this into 4.18, the outcome is

$$\dot{\boldsymbol{x}}^* + \delta\dot{\boldsymbol{x}} = \boldsymbol{f}(\boldsymbol{x}^*, t) + \frac{\partial \boldsymbol{f}(\boldsymbol{x}^*, t)}{\partial \boldsymbol{x}}\delta\boldsymbol{x} \tag{4.20}$$

where the term $\dfrac{\partial \boldsymbol{f}(\boldsymbol{x}^*, t)}{\partial \boldsymbol{x}}$ can be expressed as follow:

$$\frac{\partial \boldsymbol{f}(\boldsymbol{x}^*, t)}{\partial \boldsymbol{x}} = \boldsymbol{A} = \begin{bmatrix} 0 & 0 & 1 & 0 \\ 0 & 0 & 0 & 1 \\ W_{/xx} & W_{/xy} & 0 & 2 \\ W_{/yx} & W_{/yy} & -2 & 0 \end{bmatrix} \tag{4.21}$$

At this point, from Equations 4.20 and 4.8, in overall it is known that:

$$\begin{cases} \delta\dot{\boldsymbol{x}} = \boldsymbol{A}\delta\boldsymbol{x} \\ \delta\boldsymbol{x} = \boldsymbol{\Phi}\delta\boldsymbol{x_0} \end{cases} \tag{4.22}$$

Rearranging system 4.22, finally it is recovered that:

$$\dot{\boldsymbol{\Phi}} = \boldsymbol{A} \, \boldsymbol{\Phi} \tag{4.23}$$

Relation 4.23 shall therefore be integrated together with the equations of motion, resulting

in a system of 42 ODEs. In particular, the initial conditions on $\boldsymbol{\Phi}$ is easily recovered from Equation 4.8 with $t = t_0$, as reported in Equation 4.24

$$\delta\boldsymbol{x} = \boldsymbol{\Phi}(t, t_0)\delta\boldsymbol{x_0} \xrightarrow{[t = t_0]} \delta\cancel{\boldsymbol{x_0}} = \boldsymbol{\Phi}(t_0, t_0)\delta\cancel{\boldsymbol{x_0}} \longrightarrow \boldsymbol{\Phi}(t_0, t_0) = \boldsymbol{I} \qquad (4.24)$$

where $\boldsymbol{I}$ is the identity matrix.

The problem is thus transformed into:

$$\begin{cases} \dot{\boldsymbol{x}} = \boldsymbol{f}(\boldsymbol{x}) \\ \dot{\boldsymbol{\Phi}} = \boldsymbol{A}\,\boldsymbol{\Phi} \\ \boldsymbol{x}(0) = \boldsymbol{x_0} \\ \boldsymbol{\Phi}(0) = \boldsymbol{I} \end{cases} \qquad (4.25)$$

Applying this procedure to some of the initial conditions provided by Henon (table I, [27]), the periodic orbits found (see Figure 4.1) have the second intersection with x-axis at the same values reported in the paper: this assesses again the correctness of the work done up to this point.
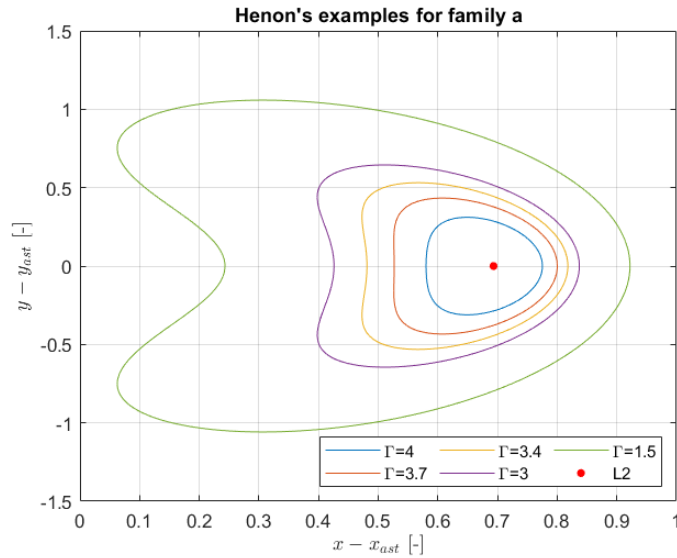
Figure 4.1: Some periodic orbits $\in$ family a found starting from ICs provided in [27].

4.2.   Continuation method to obtain a Halo family

In order to then retrieve a complete family of periodic orbits, with different amplitude and therefore energy, it is possible to apply the *continuation method*. This approach aims to

recover more orbits starting from two initial conditions proved to generate periodic orbits. Specifically, once one solution is found exploiting the method herein-above explained, the procedure to be followed to generate a family is the following [42]:

1. perturbing the known solution $\boldsymbol{x_1} = [x_1 \ 0 \ 0 \ v_{y1}]$, a new initial guess $\boldsymbol{x_2} = [x_1 + dx \ 0 \ 0 \ v_{y1}]$ is obtained;

2. $\boldsymbol{x_2}$ can be then improved exploiting the differential correction method;

3. being now $\boldsymbol{x_2}$ and $\boldsymbol{x_1}$ two known correct solutions, it is possible to write $\Delta\boldsymbol{x} = \boldsymbol{x_2} - \boldsymbol{x_1} = [dx \ 0 \ 0 \ dv_y]$;

4. the new initial guess is then $\boldsymbol{x_3} = \boldsymbol{x_2} + \Delta\boldsymbol{x} = [x_2 + dx \ 0 \ 0 \ v_{y2} + dv_y] = [x_3 \ 0 \ 0 \ v_{y3}]$;

5. $\boldsymbol{x_3}$ can be then corrected using the differential correction method generating a new accurate solution;

6. the process is then iterated until a family is generated.

The crucial parameter of this method is the dx applied to $\boldsymbol{x_1}$ on step 1. If this is too large, in fact, the differential correction will not be able to find any solution if not one completely divergent: this, once again, underlines the large sensitivity of the problem. Following this approach, the halo families a, c, g and f of the Sun-Ryugu system have been found and are shown in Figures 4.2 and 4.3.
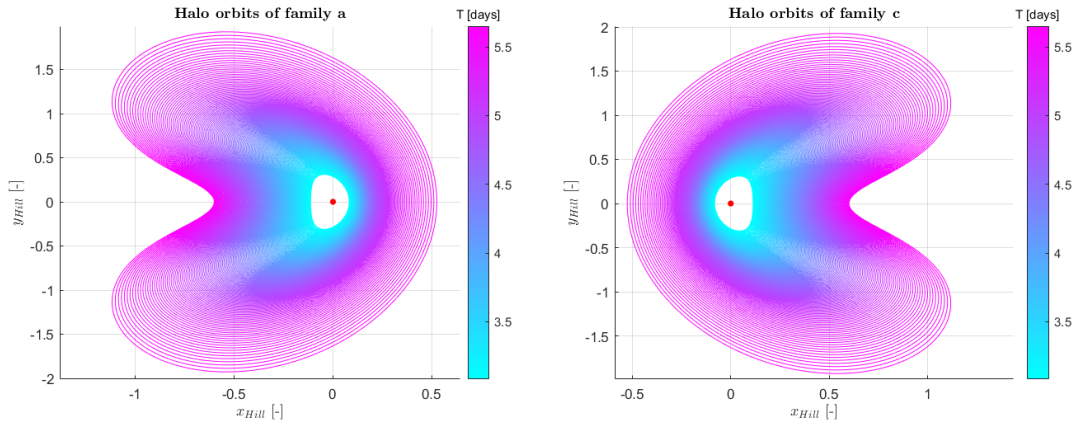
Figure 4.2: Halo families a and c were found with the continuation method, starting from an initial guess provided by [45] and [27]. From this image, it is clear the symmetry between the two families.
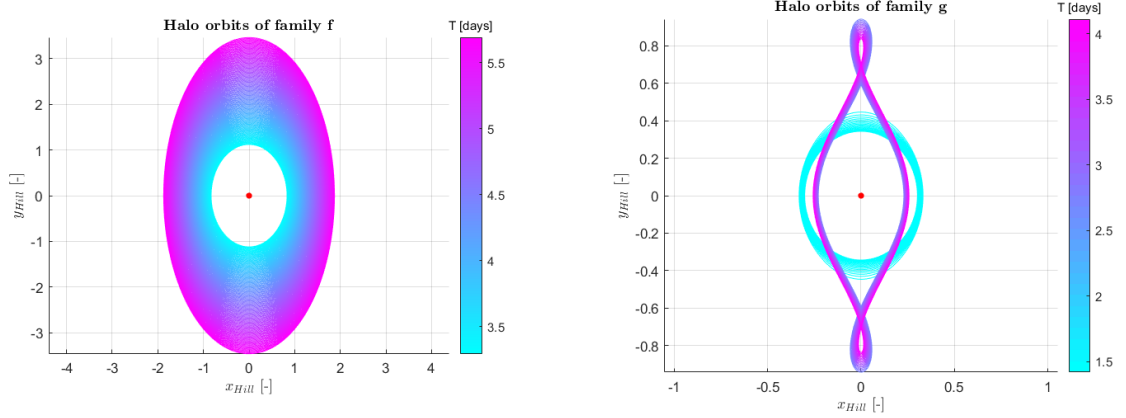
Figure 4.3: Halo families f and g found with the continuation method, starting from an initial guess provided by [45] and [27]. Family f is shown on the left while family g on the right.

4.3.   Trajectory in the Neck Region

In this section, it will be analyzed the motion in the neck region, required due to the expansion of the portion of space of interest to the neighboring zones of L2. Firstly, it is necessary to introduce the lagrangian function L that, in a rotating frame, can be expressed as stated in Equation 4.26 [21].

$$L(x, y, \dot{x}, \dot{y}) = \frac{1}{2}((\dot{x} - y)^2 + (\dot{y} + x)^2) - U(x, y) \tag{4.26}$$

with $U(x, y) = -\dfrac{\mu_1}{r_1} - \dfrac{\mu_2}{r_2} - \dfrac{1}{2}\mu_1\mu_2$, being $r_1^2 = (x + \mu_2)^2 + y^2$ and $r_2^2 = (x - \mu_1)^2 + y^2$. Once introduced this quantity, it is possible to transform the lagrangian system into the Hamiltonian form by means of the Legendre transformation applied in Equation 4.27. From this, the Hamiltonian equations of motion take the form shown in expression 4.28 [21].

$$p_i = \frac{\partial L}{\partial \dot{q}^i}, \qquad H(q^i, p_i) = \sum_{i=1}^{n} p_i \dot{q}^i - L(q_i, p_i) \tag{4.27}$$

$$\begin{cases} \dot{q}^i = \dfrac{\partial H}{\partial p_i} \\[4mm] \dot{p}_i = -\dfrac{\partial H}{\partial q^i} \end{cases} \tag{4.28}$$

In this case, the Legendre transformation is given by Equation 4.29, leading to the Hamiltonian function expressed in Equation 4.30.

$$
\begin{cases}
p_x = \dfrac{\partial L}{\partial \dot{x}} = \dot{x} - y \\[3mm]
p_y = \dfrac{\partial L}{\partial \dot{y}} = \dot{y} + x
\end{cases}
\tag{4.29}
$$

$$
H(x, y, p_x, p_y) = p_x \dot{x} + p_y \dot{y} - L = \frac{1}{2}\left((p_x + y)^2 + (p_y - x)^2\right) + \bar{U}
\tag{4.30}
$$

Now, aiming to study the linearised motion around the lagrangian point as done previously, the quadratic terms of H will be necessary. To achieve this, an expansion of H about the equilibrium point is performed, obtaining the Hamiltonian function for the linearised equations (H_l), which are shown in Equation 4.32 [21].

$$
H_l = \frac{1}{2}\left[(p_x + y)^2 + (p_y - x)^2 - ax^2 + by^2\right]
\tag{4.31}
$$

$$
\begin{cases}
\dot{x} = \dfrac{\partial H_l}{\partial p_x} = p_x + y \\[3mm]
\dot{y} = \dfrac{\partial H_l}{\partial p_y} = p_y - x \\[3mm]
\dot{p}_x = -\dfrac{\partial H_l}{\partial x} = p_y - x + ax \\[3mm]
\dot{p}_y = -\dfrac{\partial H_l}{\partial y} = -p_x - y - by
\end{cases}
\tag{4.32}
$$

In Equation 4.31, $a = 2\bar{\mu} + 1$ and $b = \bar{\mu} - 1$, where $\bar{\mu}$ can be recovered from relation 4.33, where x_e in this case shall be replaced with the abscissa of L2.

$$
\bar{\mu} = \mu |x_e - 1 + \mu|^{-3} + (1 - \mu)|x_e + \mu|^{-3}
\tag{4.33}
$$

Having defined these quantities, it is then possible to return back to lagrangian form by means of the inverse Legendre transformation. This enables to recover the linearised lagrangian equations of motion, reported in relation 4.34.

$$\begin{cases} \dot{x} = v_x \\ \dot{y} = v_y \\ \ddot{x} = \dot{v}_x = 2v_y + ax \\ \ddot{y} = \dot{v}_y = -2v_x - by \end{cases} \tag{4.34}$$

Equation 4.34 can be written in a vector-matrix form as follow:

$$\begin{bmatrix} \dot{x} \\ \dot{y} \\ \dot{v}_x \\ \dot{v}_y \end{bmatrix} = \begin{bmatrix} 0 & 0 & 1 & 0 \\ 0 & 0 & 0 & 1 \\ a & 0 & 0 & 2 \\ 0 & -b & -2 & 0 \end{bmatrix} \begin{bmatrix} x \\ y \\ v_x \\ v_y \end{bmatrix} \tag{4.35}$$

Calling the matrix on the right-hand side of relation 4.35 as $\boldsymbol{M}$, it is easy to find out that it presents two real and two imaginary eigenvalues, $\pm\lambda$ and $\pm i\nu$ respectively corresponding to the eigenvectors $\boldsymbol{u_1}, \boldsymbol{u_2}, \boldsymbol{\omega_1}, \boldsymbol{\omega_2}$. From this consideration it is possible to deduce that the general solution will have the form reported in Equation 4.36

$$\boldsymbol{x} = (x, y, \dot{x}, \dot{y}) = \alpha_1 e^{\lambda t} u_1 + \alpha_2 e^{-\lambda t} u_2 + 2\,\mathrm{Re}(\beta e^{i\nu t}\omega_1) \tag{4.36}$$

where α_1, α_2 are real while $\beta = \alpha_1^2 + i\alpha_2^2$ is complex. It is easy to understand how the solution is thus strongly dependent on α_i and, in fact, following Koon et al. [21], nine different classes of orbits comes out for different combinations of α_i signs. Nevertheless, the one of particular interest for this work is the *Lyapunov orbit* that arises for $\alpha_1 = \alpha_2 = 0$. According to Conley [47], this periodic orbit projects onto the xy-plane as an ellipse centered at L2, having major and minor axis of length equal to $2\tau\sqrt{\epsilon/k}$ and $2\sqrt{\epsilon/k}$ respectively. While ϵ is a variable that rules the amplitude of the orbit, k is a constant that can be computed as:

$$k = -a + b\tau^2 + \nu^2 + \nu^2\tau^2 \quad \text{with} \quad \tau = -\left(\frac{\nu^2 + a}{2\nu}\right) \tag{4.37}$$

Aiming to extend the region of interest to a halo neighborhood, it is required to decrease the energy level to which the ZVC are referred. In particular, it will be no longer considered the energetic level C_2 but one *slightly* smaller, called C' ($C' = 0.9999999999997C_2$, highlighting once again how sensitive this problem really is). Such a value is imposed taking care of how the ZVC will be affected by it. The new ZVC, shown in Figure 4.4 for

both $r_P = 78.5 \ \mu m$ and $r_P = 10$ mm, shall still present a shape giving important hints on the direction from where the particles are escaping. To evidence this concept, Figure 4.5 portrays the ZVC for $C'' \ (= 0.999999999999 C_2)$: as can be seen, the accessible realm becomes too wide to provide functional indication of where the particles are escaping from the system.
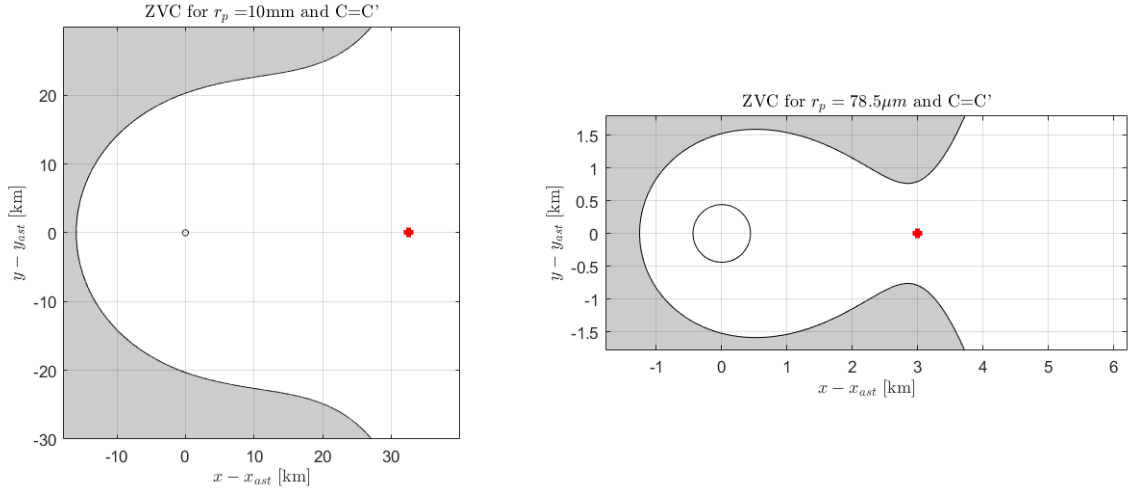
Figure 4.4: Zero velocity curve for energy level fixed at C' for $r_P = 10$ mm (left) and $r_P = 78.5 \mu m$ (right).
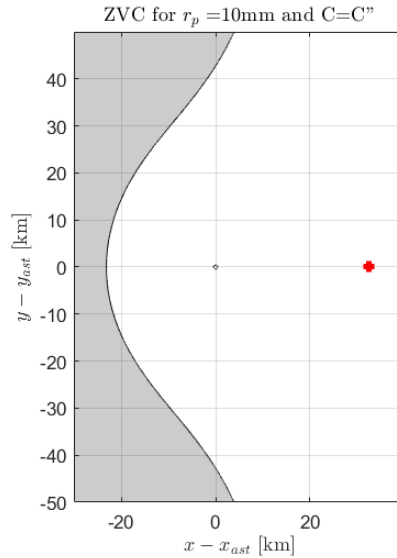
Figure 4.5: Zero velocity curve for energy level fixed at C'' for $r_P = 10$ mm.

Assuming this new energetic level as the level of interest, it is then possible to design the motion in the neck region, i.e. in the region corresponding to the bottleneck opened at L2. This has been done for both the values of r_P, in order to underline all the advantages or

drawbacks arising from them. Assuming for $r_P = 78.5$ μm and $r_P = 10$ mm a semi-major axis (SMA) of 0.75 km and 28.5 km respectively, through Equation 4.38 it is possible to retrieve the adimensional values of ϵ, which are reported in Table 4.1.

$$\epsilon = \left(\frac{SMA_{adim}}{\tau}\right)^2 k \quad \text{with} \quad SMA_{adim} = \frac{SMA}{l_{ref}} \tag{4.38}$$

-	$r_P = 78.5\mu m$	$r_P = 10$ mm
ϵ	$1.6902 \cdot 10^{-12}$	$1.9452 \cdot 10^{-12}$

Table 4.1: ϵ values for cases with $r_P = 78.5\mu m$ and $r_P = 10$ mm.

The resulting orbits are shown in Figure 4.6. It is evident how, in the case of $r_P = 78.5$ μm, the small orbit resulting enables the spacecraft to fast "survey" around the whole bottleneck opened. In this scenario, therefore, almost all the ejecta escaping through the bottleneck having sizes close 78.5 μm can be assumed to be captured. Contrarily, the biggest particles will not have to pass through that same aperture, therefore just a tiny portion of this kind of ejecta can be considered to be actually gathered. On the other hand, a bigger orbit such as the one obtained for $r_P = 10$ mm enables the capture of a wider range of particles. In fact, pretty much all the ejecta escaping from the system will pass throughout that portion of space. However, since the orbit is much bigger, it can not be ensured that, when an ejecta is escaping, the spacecraft will be there and not in another tract of its path.
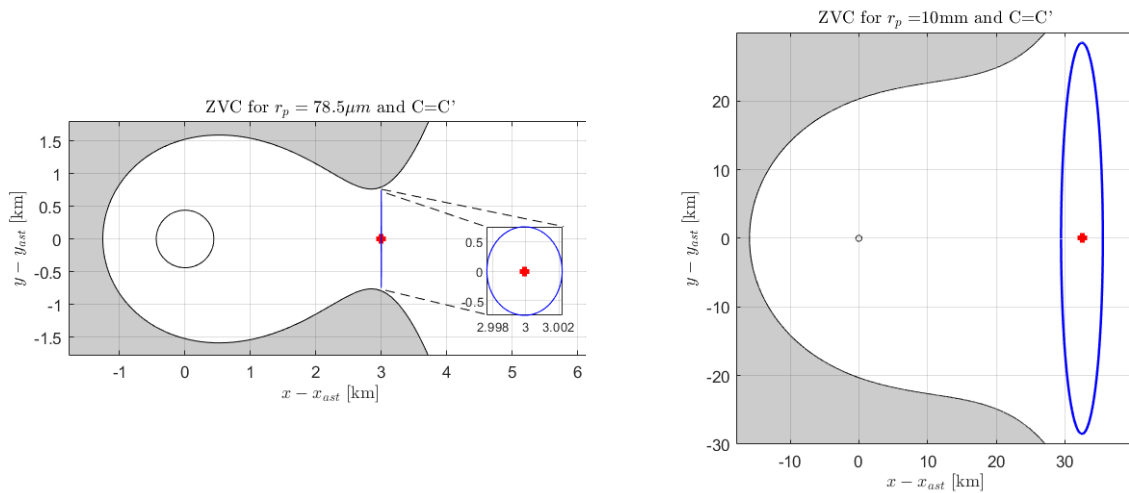
Figure 4.6: Periodic orbit in the neck region formed by the ZVC with $C = C'$ for $r_P = 78.5$ μm (left) and $r_P = 10$ mm (right).

5 | Results of ejecta dynamics

In this section, finally the results obtained by fixing the energetic level of interest to $C = C'$ will be analysed. Firstly, it is interesting to understand the number of particles falling within each category, important to have a quick and general impression of the feasibility of the mission. This, achieved by counting the trajectories falling into each category in the obtained database, is shown in Figures 5.1 and 5.2 for point mass and rigid body respectively and, in percentage terms, in Table 5.1.
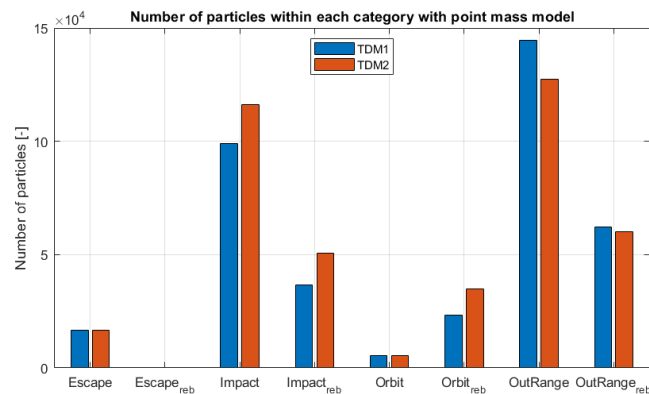
Figure 5.1: Histogram representative of the number of ejecta falling within each category for the point mass model.

It can be noticed from the figures that the number of particles escaping the system does not change when considering PM or RB approximation. For both TDM1 and TDM2, in fact, independently of the model exploited, the number of ejecta able to leave the interior realm of the ZVC is found to be 16610: This is simply explained by recalling the real difference between PM and RB models, i.e. the range of allowed impact angles. From this consideration it is straightforward to understand that, whatever the chosen approach, it will not affect the behavior of particles that do not impact back on Ryugu, neither for *Escape* nor *Orbit* categories. This last, in fact, counts in all the cases of 5588 ejecta. Nevertheless, even though these numbers remain the same, what changes is the percentage corresponding to them, as highlighted in Table 5.1, which therefore can be seen as data able to better reflect the conduct of the system.
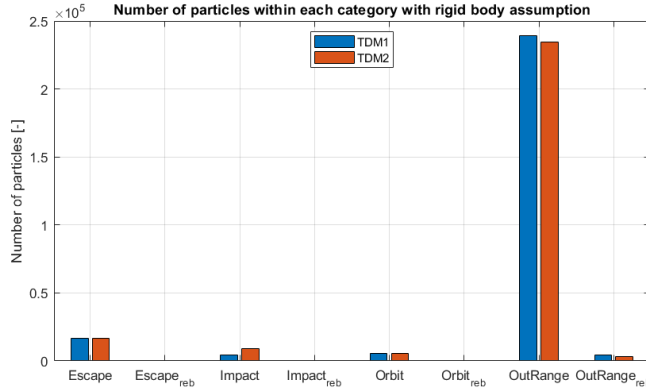
Figure 5.2: Histogram representative of the number of ejecta falling within each category for the rigid body approximation.

	TDM1		TDM2	
	PM	RB	PM	RB
Escape	4.2820	6.1476	4.0390	6.1717
Impact	25.5078	1.6058	28.2682	3.3291
Orbit	1.4408	2.0686	1.3591	2.0767
OutRange	27.2735	88.5271	30.9506	87.1572
Escape_{reb}	0	0	0	0
Impact_{reb}	9.4676	0.0470	12.3214	0.03939
Orbit_{reb}	5.9877	0.0448	8.4655	0
OutRange_{reb}	16.0400	1.5588	14.5960	1.2256

Table 5.1: Percentages of ejecta falling inside each category with respect to the total trajectories computed for each scenario.

Contrarily, as can be seen, changing the model will of course result in a drastic change in the number of the ejecta categorized as *Out Range*. Reflecting the more conservative nature of the PM model, in fact, Figure 5.1 shows a more proportioned number of ejecta between the categories *Impact* and *Out Range*. At the same time Figure 5.2, due to the huge amount of particles falling within the category *Out Range*, evidence how all the categories linked to a previous rebound feature an important drop in the number of particles. Specifically, for Impact_{reb} and Orbit_{reb} the percentage drops below the 0.05%. In such a scenario, the most probable fate for a particle is therefore to escape or to re-impact on Ryugu[1], a result completely in accordance with what was assessed by Scheeres et al. in [5]. One more interesting outcome is that analysing TDM2, the data available for this site led to a higher impact on the asteroid's soil with respect to the TDM1 case. Moreover, with PM model, these collisions will more likely occur with impact angles inside

---

[1]Note that also the *Out Range* category implies an impact.

the feasible range, therefore increasing not only the successive rebounds (i.e. categories $Impact_{reb}$ and $OutRange_{reb}$), but also the number of ejecta that can be found orbiting the asteroid, populating in this way the $Orbit_{reb}$ category.

Finally, a consideration on the category $Escape_{reb}$ that seems obvious: no particle is found to be able to escape from the system after an impact with Ryugu and the consequent rebound. The trivial indication, here, is that if a particle is ejected from Ryugu in conditions that do not permit a direct escape, that particle will never be able to leave the system neither after a sort of "re-tuning" of its initial conditions by means of an impact on Ryugu. This, of course, is a consequence of the dissipation of energy occurring during the collision with the asteroid's soil.

However, since the differences between TDM1 and TDM2 are found to be low, from here on just the TDM1 case will be shown given that, differently from TDM2, it is representative of the surface material [17], which is the one of interest in this work. Due to its more conservative formulation then, the PM approximation will be the baseline of the discussion even though the RB model could represent a better approximation of a real scenario: only in the cases where important differences arise from the use of the different models also RB will be shown. However, for completeness, all the graphs and figures described in this section will be reported, for all the cases, in Appendix B.

Studying at first the behavior of the particles impacting again on Ryugu, i.e. belonging to the 2nd-4th-6th-8th columns of Table 5.1, image 5.3 is able to return a global idea on which is the time required for this ejecta to collide with the soil. In the figure, blue is for Impact, green is for $Impact_{reb}$, red is for OutRange and magenta is for $OutRange_{reb}$.
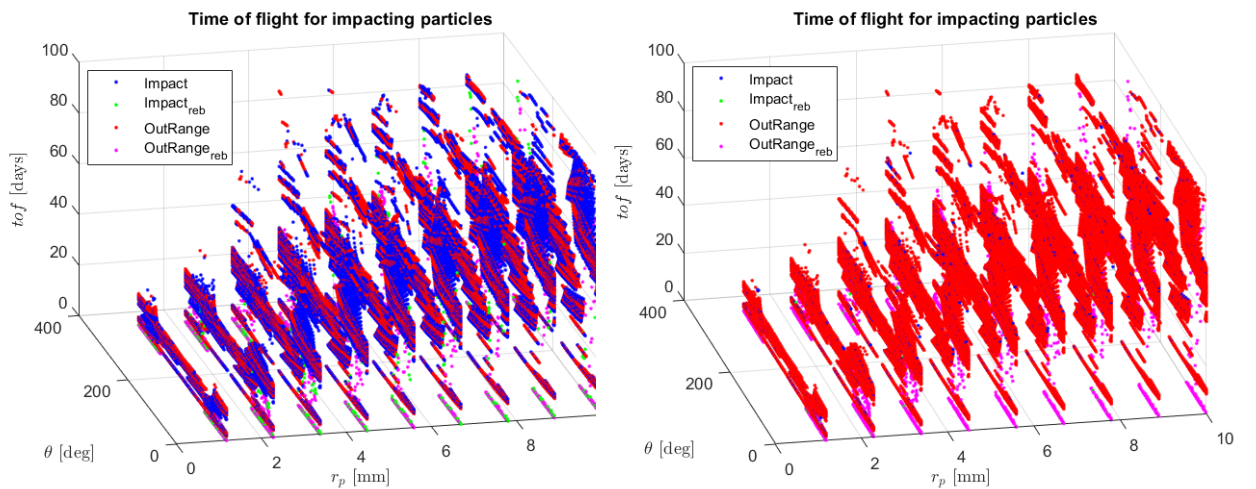
Figure 5.3: Time of flight for impacting particles for PM (left) and for RB (right). Both are representative of TDM1.

As visible, the larger the ejecta the higher will be the number of particles impacting again

with the asteroid. Contemporary, the plot shows also that the time that ejecta will take to collide again with the soil grows with r_P as well. This means that, for larger particles, a higher percentage will stay detached from the surface for a larger time. Therefore, these ejecta will likely interact with the particles found to escape, which will be actually fewer. The graph, then, highlights how, applying RB model rather than the PM one, the global trend is the very same, but much more particles fall within both the OutRange categories. The number of collisions occurring with impact angles within the suitable range, in fact, drastically passes from 39.61% for PM to 1.80% for RB.

For the same reason, it is important to understand what are the conditions that more likely will put ejecta into orbit around Ryugu: these, in fact, could represent a non-negligible source of "traffic" that escaping particles will have to overcome before successfully leaving the system. Figure 5.4 relates r_P, θ and v_{ej} able to inject a particle in orbit: specifically, blue stays for direct orbit while red for orbiting after a previous rebound.
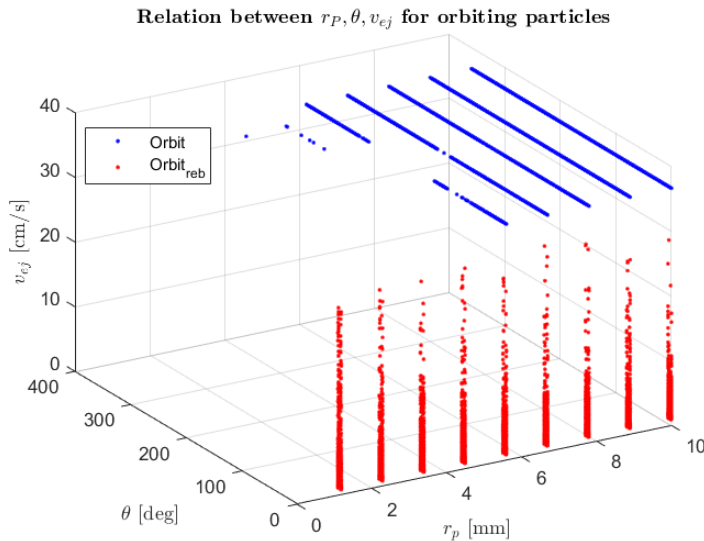
Figure 5.4: Plot highlighting how r_P, θ and v_{ej} are related for particles injected on orbit.

Looking at the graph, firstly it is possible to note how the conditions for having a direct or indirect orbit are well decoupled. For direct orbit, in fact, v_{ej} shall be slightly higher than 36 cm/s. Furthermore, for higher r_P the range of longitude able to inject a particle in orbit becomes wider, leading therefore to the observation that the higher r_P, the higher will be the probability of having a particle able to directly orbit the asteroid. It is also curious the fact that no conditions can directly inject into orbit the smallest particles. Contrarily, with low r_P the number of indirect orbits is large, then dropping for increasing particles' size. Interesting is the fact that all the indirect orbits found in this work were born from previous impacts occurring at a longitude between 0 and 6 degrees. From the

moment that the number of orbits presents a different trend with r_P between direct and indirect, it can be interesting to study which particles' dimension leads to the highest number of orbiting ejecta. This, is clearly shown in Figure 5.5.
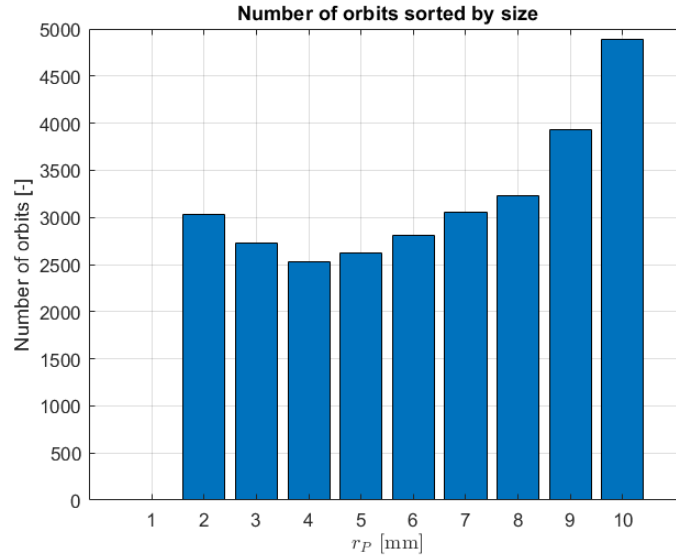
Figure 5.5: Number of orbits (direct+indirect) sorted by size.

The bar graph highlights that for central values of r_P the number of orbits found is lower, but this increases both for smaller and larger particles. However, the most common orbits will regard the biggest particles: these orbits therefore represent even more severe obstacle for ejecta that is running away from Ryugu's system. However, these interactions are not retained to be particularly relevant, also since all the ejecta will be generated from the same initial plume, meaning that once the remaining particles start orbiting for some revolutions, the smaller particles will have already left the neighborhood of the asteroid. For these reasons, such inter-particles are considered to be safely neglected and therefore the dissertation will continue without taking into account the "traffic" that an escaping particle could face, both from orbiting particles and for particles that have not impacted yet.

Focusing at this point on the escaped ejecta themselves, these are the ones that really rule the feasibility of the mission. Figure 5.6 evidence the number of ejecta escaped depending on their size and on the ejection longitude.

The figure, shows that the conditions that make a particle able to escape can be divided in two groups: one having $\theta < 100°$ and another with $200° < \theta < 350°$. This division will be present and reflected in all the analyses performed in this work. A further observation highlights how increasing r_P, the range θ allowing particle escape grows. Linked to this, in the figure it is also visible how the number of escaping ejecta increases for higher values
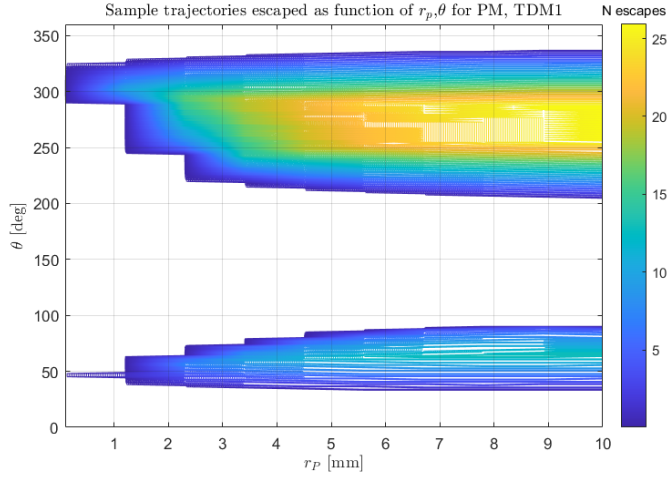
Figure 5.6: Contour plot on the sample trajectories found to escape depending on r_P and θ.

of r_P. This is intuitive since, for larger particles, the bottleneck of the ZVC grows in size (see Figure 4.6). However, the trend shown is a bit different: in fact, a higher r_P will correspond to a relevant rise of the escaping sample trajectories only for longitudes around the central region of each one of the groups mentioned before. Anyway, from Figure 5.6 it is possible to conclude that the biggest part of the ejecta able to escape comes from the upper group, departing therefore from longitudes between 200 and 350 degrees, especially for larger sizes . No particles passing throughout the neck region are found for $100° < \theta < 200°$. A more quantitative analysis is depicted in Figure 5.7: once, again the number of sample trajectories that successfully escape from the system increases with r_P. Interestingly, no particles having $r_P = 78.5 \ \mu m$ are found to successfully escape.

Similarly, another plot has been recovered analysing this time the behavior with γ_{ej} rather than r_P (see Figure 5.8).

Correctly, due to problem's geometry, the plot does not show any symmetric behavior on γ_{ej}. In addition, once again, the figure distinguishes the same two groups highlighted in Figure 5.6. The group on the left, i.e. the lower on Figure 5.6, shows that most of the escaping trajectories comes from the lowest longitude and the highest (γ_{ej} here is negative) ejection angles while, as θ increases, not only the escapes are less but also require lower γ_{ej}. Contrarily, the other group exhibits the opposite trend: the number of escaped orbits, in fact, is higher for lower positive values of γ_{ej} and increases with θ. This is of course a consequence of the geometry of the problem, as can be seen in Figure 5.9. The conditions highlighted by Figure 5.8 as the ones providing the larger number of ran away ejecta, in fact, are those driving the particle to be ejected towards the direction of the bottleneck.
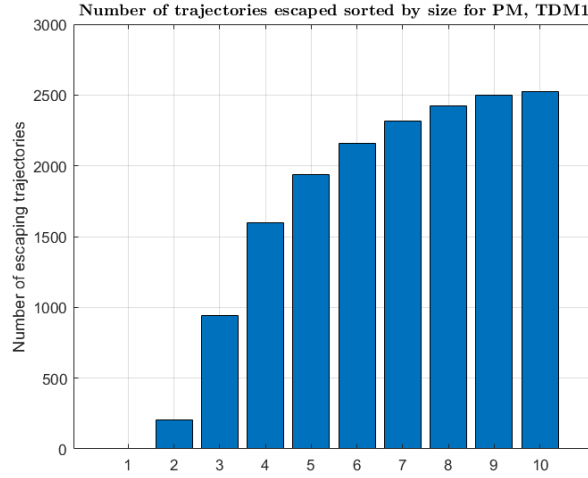
Figure 5.7: Sample trajectories leaving the system sorted by size for PM and TDM1

Another crucial variable able to assess or negate the feasibility of the mission is the time required to perform the collection. Specifically, for this preliminary study, the time of flight of each particle is assumed as the time at which the ejecta leaves the Hill's sphere. Visually it is shown in Figure 5.10 with respect to r_P and θ.

The very first observation to be done here is to evidence how smaller particles are able to escape quicker than the larger ones. This is connected to the fact the smaller particles experience a higher acceleration due to SRP and it is in agreement with the findings in [31] and [34]. Furthermore, the plot shows that, for the same r_P, particles leaving from Ryugu with $200° < \theta < 350°$, i.e. the ones belonging to the upper group in Figure 5.6, will be able to escape from the system, on average, in less time: this can represent valuable information on the ejection behavior.

As already said, the feasibility of the mission will be strongly dependent on the time window fixed for the mission itself. Analysing how the percentage of ejecta escaped (and potentially collected) with respect to the total number found with this analysis versus the possible time spans of the mission, the plot obtained is the one reported in Figure 5.11. Then, fixing time spans from 1 to 3 months, the percentage values found are reported in Table 5.2. From this analysis, it is possible to conclude that this kind of mission will have to last more than one month.

	1 month	2 months	3 months
%	12.176	95.972	100

Table 5.2: Variation of % of ejecta escaped for time windows fixed to 1-2-3 month(s).

To better assess the required time span, it is possible to follow another approach. Specif-
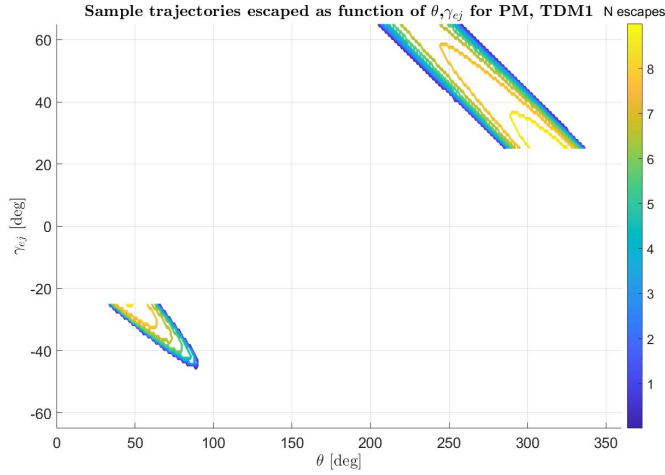
Figure 5.8: Contour plot on the number of escaped sample trajectories depending on θ and γ_{ej}.

ically, from Figure 5.7 and knowing the density of the particles, it is then possible to retrieve the mass escaped, and therefore possibly collected, sorted by size. The mass escaped for each particle's dimension is reported in Figure 5.12, leading to a total mass equal to $m_{tot} = 36.2683$ kg. Note that, even though for scale reasons the second and third columns ($r_P \simeq 1.181$ mm and $r_P \simeq 2.283$ mm) seem empty, the result is that they actually provide about 1.8040 and 60.343 g respectively.

Of course, the biggest portion of mass that can be gathered comes from the larger ejecta but, for what has been previously explained and highlighted when dealing with advantages and disadvantages between the possible neck orbits (see Figure 4.6), the larger the ejecta of interest, the lower the capture probability will be. For this reason, in order to maximise the collection probability, it is possible to choose as a reference scenario the one having the neck orbit shown in Figure 4.6 on the left. The threshold value on the gathered mass, able to determine the feasibility of the mission, is here imposed as the same mass collected on Hayabusa2 mission, that is about 5.262 g [16]. Such a value is retained suitable to give a preliminary hint on the feasibility for the kind of mission here proposed, since being able to collect the same amount of material but without any landing can be considered a complete success. Stated this, the procedure followed has been, summing the masses corresponding to each particle's size starting from the smallest, to understand which particles could have been neglected. All this reasoning can be applied from the moment that the smallest particles feature the lowest tof before escape. The result is that, for $78.5\mu m < r_P \leq 2.283$ mm, the total mass is found to be $\simeq 62.15$ g. This value comprehends 1.8040 g deriving from particles having $r_P = 1.181$ mm, while the
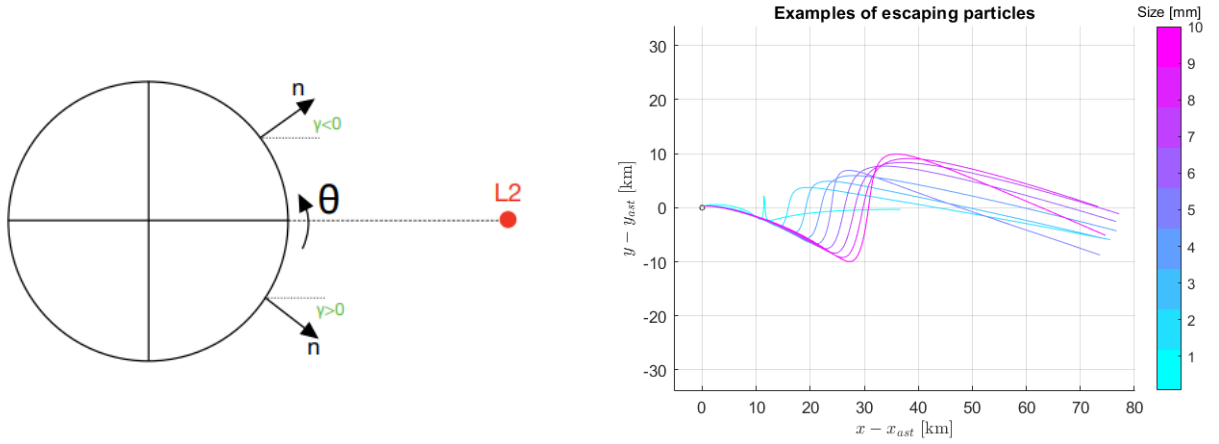
Figure 5.9: The simplified sketch on the left (not in scale) evidences how the best conditions for particle escape highlighted in Figure 5.8 represent the situation for which the particle "points" towards L2. On the right is thus reported an example of few escaping trajectories that support what said.

rest is attributed to ejecta with $r_P = 2.283$ mm. Assuming, for the reasons explained herein above and relatively to Figure 4.6, that in such a scenario the particles can be all considered to be collected, it is now possible to understand how long should be the mission time span in order to gather the remaining $5.262 - 1.8040 = 3.458$ g coming only from the ejecta with $r_P = 2.283$ mm. Following this approach, it is found that the ejecta having $r_P = 2.283$ mm are able to provide the required mass after 22.48 days, as shown in Figure 5.13. This is therefore the minimum mission duration (excluding travel time to get to Ryugu's system) proposed at the end of this work.

The next step it to estimate the velocity at which the collection will occur. This is fundamental information necessary to start a preliminary design of the capture mechanism, that will be introduced in Chapter 6. In this work, the capture velocity will be assumed to be the velocity with which the particle run away from the Hill's sphere, i.e. when it is assumed to be successfully escaped. Actually, to this purpose, the velocity that should be considered is the relative speed between the ejecta and the spacecraft. However, the assumption explained before shall be enough to start a preliminary design. Following this idea, the capture velocity is easily recovered propagating the conditions stored in the database leading to the condition *Escape* for $t = tof$. The result obtained can be seen in Figure 5.14 .

From it, it is clear that the smaller the ejecta, the higher will be the velocity with which it will escape and therefore assumed to be captured. This is a positive aspect since,
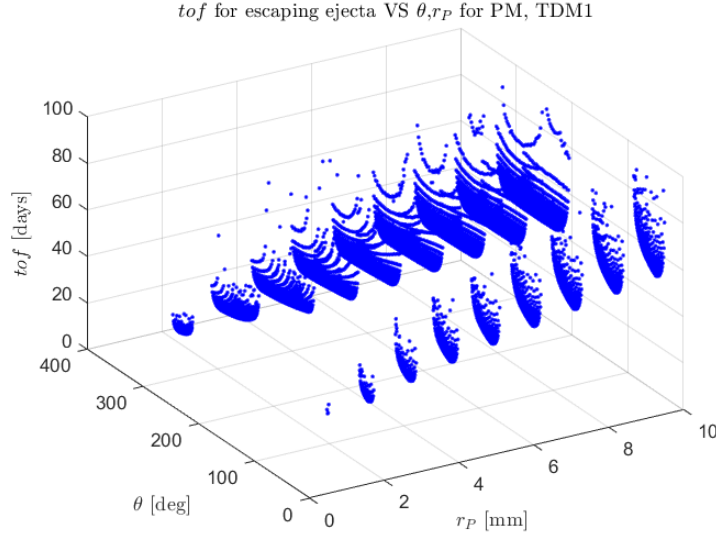
Figure 5.10: Time of flight of escaping particles with respect to r_P and θ.

otherwise, the kinetic energy recovered for the ejecta would grow both with r_P and $V_{capture}$, likely touching prohibitive values. Moreover, it is possible to see how, for ejecta belonging to the upper group defined in Figure 5.6, the capture velocity is found to be slightly inferior on average with respect to the ejecta of the second group. Knowing from Figure 5.6 that the biggest part of the ejecta escapes from the first group, this graph is telling that the majority of the ejecta is arriving at lower velocities, especially for high r_P. In addition to this, from Figure 3.1 it is known that bigger particles feature a higher v_{ej}: this means that, contrarily to what could be thought, particles departing from Ryugu with the highest velocities are the same that could be collected at a lower capture speed. To conclude, this plot also shows that, apart for some isolated case, almost all the particle will arrive with a velocity between 100 and 300 m/s. It is therefore interesting now to analyze the kinetic energy with which the particle would be captured, that corresponds to the one that the collection mechanism will have to dissipate. From $V_{capture}$, the kinetic energy can be computed as:

$$E_{kin} = \frac{1}{2}mV_{cap}^2 = \frac{1}{2}\rho_P \left(\frac{4}{3}\pi r_P^3\right) V_{cap}^2 \tag{5.1}$$

Picture 5.15 shows the result as function of $V_{capture}$ and r_P.

The graph clearly shows how the larger particles are the ones with the higher kinetic energy even when they present a lower capture velocity, meaning that r_P "weights" more than the velocity. This not only agrees with the exponents of relation 5.1, but also underlines
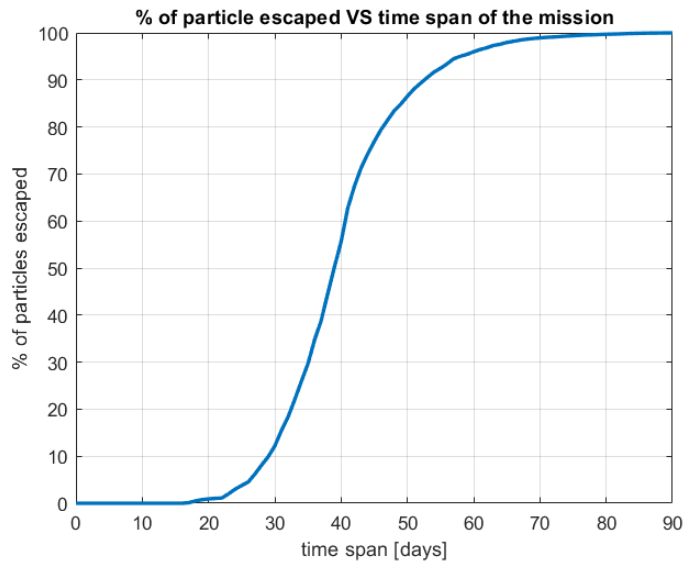
Figure 5.11: Trend of the % of ejecta escaped with respect to the time window.

the dissertation done earlier regarding the relation between v_{ej} and $V_{capture}$: correlated to this, it is also found that the larger the ejecta dimension, the lower the minimum capture speed. Furthermore, one of the most important outcomes of this explanation regards the maximum kinetic energy that should be dissipated by the collection mechanism. Specifically, its value is found to be $E_{kin_{max}} = 1.9258 \cdot 10^{-4} J$ and will be used to impose a preliminary design concerning the collection technique.
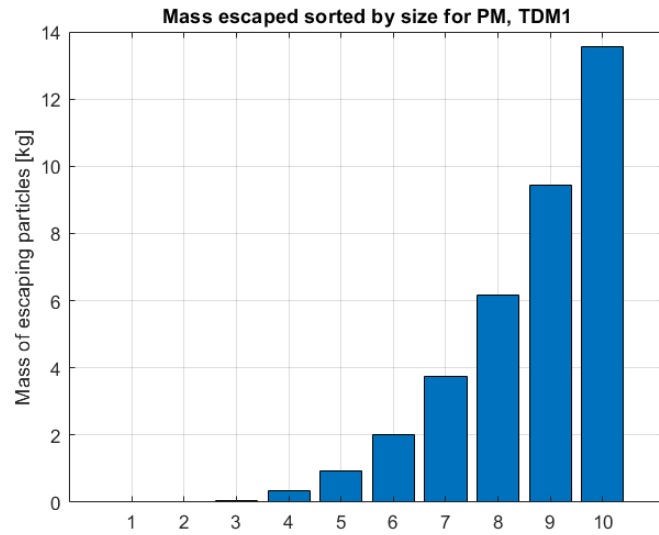
Figure 5.12: Distribution of the mass possible to gather sorted by size.
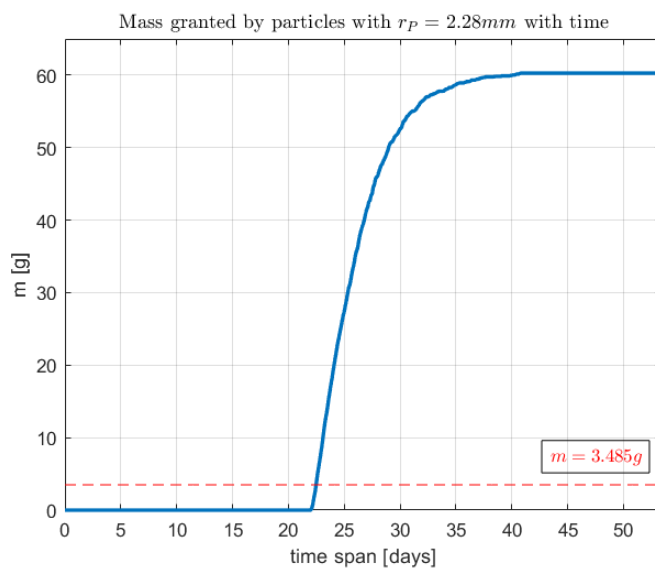
Figure 5.13: Mass granted by particles with $r_P = 2.28$ mm over time.
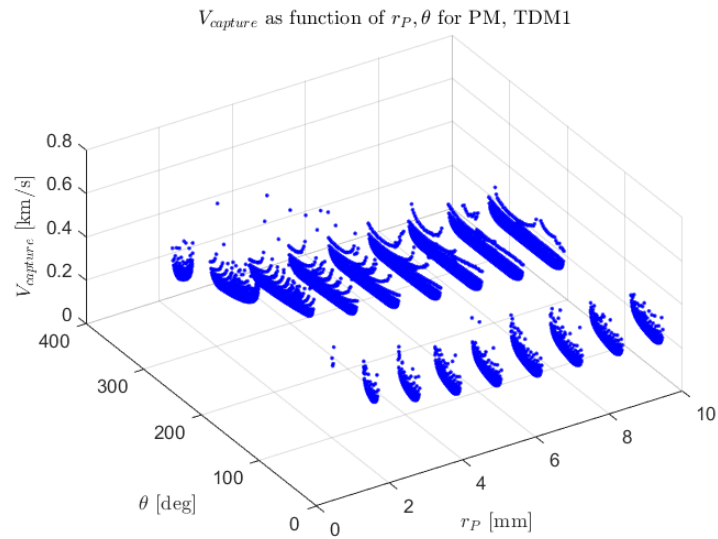
Figure 5.14: Capture velocity expressed as function of r_P and θ.
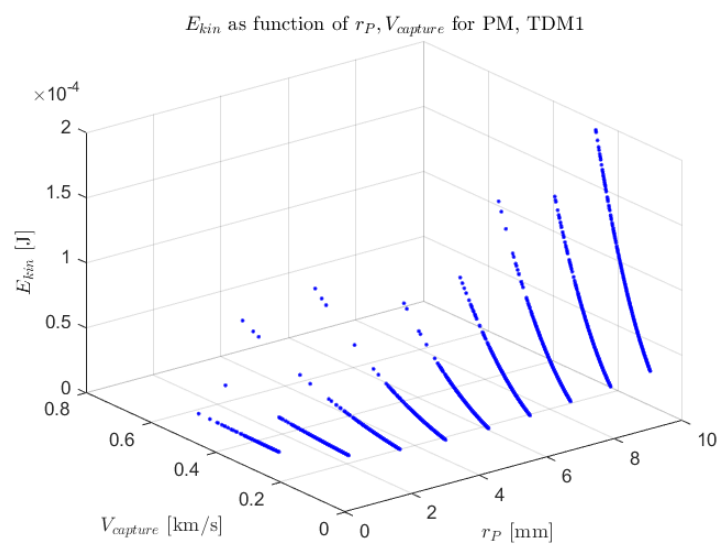
Figure 5.15: Ejecta's kinetic energy when exiting from the system throughout the L2 bottleneck.

6 | Capture mechanism

This section will discuss the main strategies adopted until now to perform on-orbit captures, then highlight advantages, disadvantages and modifications needed to complete the task required for this mission. Finally, some guidelines and indications for a preliminary design will be provided.

Concerning the possible approaches deriving for debris removal around Earth, the main possibilities are based on the use of a robotic-base on-orbit service (OOS) or on flexible tether nets, even though different systems have been thought in the past few years. The RemoveDEBRIS mission in fact, was a satellite research project, carried on by the *University of Surrey*, which aimed to demonstrate various space debris removals technologies such as net systems, harpoons, vision-based navigation (VBN) and a dragsail [48]. However, these are not adapted to be exploited for a collection mission of multiple particles that, moreover, foresees a re-entry phase for sample analysis rather than de-orbiting as planned for Earth debris removal operations. Regarding instead a robotic OOS, the major problem encountered is the attitude disturbance provoked to the spacecraft base when robotic arm and target particle physically intercept, causing destabilization or severe hardware damage [7]. Even though these aspects could be partially overcome throughout the *Reaction-Null Space* concept introduced by Yoshida and Nenchev [49], this solution remains unsuitable for the capture of multiple particles at a time, considering also the wide size range of the ejecta.

The conclusion is that, for this work's scenario, the most suitable technology is represented by the so-called *aerogel capture*, already introduced in section 1.3.2 talking about the Stardust-NExT mission but then improved for the *Tanpopo Cosmic Dust Collector* mission. Such a capture mechanism is based on the use of silica aerogel. This, is considered to be the world's lightest solid and, to give an idea of its particularity, NASA's website says that *"it is probably not possible to make aerogel any lighter because then it would not gel - the molecules of silicon would not connect"*. For this reason aerogel is sometimes referred to as a "solid smoke" being formed for 99.8% of air, resulting in an ultra-low density material. This is a fundamental property, since, for the same internal structure, lower density yields lower pressure shock levels at impact [50].

Furthermore, this highly porous material based on silicon dioxide (of which production procedure is briefly sketched in Figure 6.1) presents a mesostructure that resembles strings of pearls with sizes from 10 to 100 Å: this also grants an high emissivity for the material, which is therefore able to dissipate heat, avoiding any issue related to the thermal cycles felt in space [50]. Aerogel, in fact, was also exploited as lightweight thermal insulator on one of the Mars Pathfinder's rovers.

For several decades, it was believed that an intact capture of a "cosmic projectile" was not possible without converting the particle into plasma, in order to then collect the vaporized condensates, i.e. without atomizing the ejecta . The development of this technology, instead, enables intact particle capture, preserving therefore not only its elemental composition but also its structural phases, morphology and chemical isotopic composition as well.
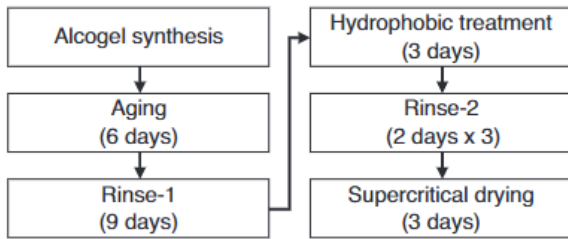
Figure 6.1: Simplified scheme of aerogel production [51].
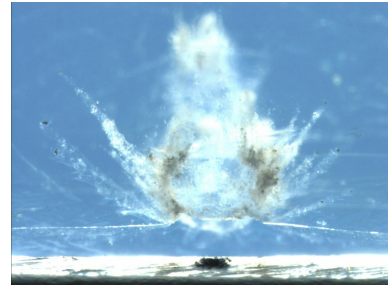
Figure 6.2: During a capture, aerogel melts around the particle trapping it. Credits: NASA/JPL.

Aerogel, in fact, slows down gradually the colliding particle: in this way, the ejecta is not vaporized or melted but, contrarily, the dissipation of energy caused by their interaction will raise the temperature, melting aerogel around the particle trapping it inside the mesostructure (see Figure 6.2). Up to date, this is achieved by creating aerogel tiles that comprise two layers with densities of 0.01 and 0.03 g/cm^3. The top layer of the panel features a lower density and it is designed to minimize the initial impact shock, while the dense layer can stop the most-energetic particles hitting the aerogel panel. This configuration enables the capture of particles having a wider energy range without the necessity of increasing the panel's thickness to stop them [52]. This double-layer structure is perfectly visible in Figure 6.4. In the picture, a particle with $r_P = 30 \ \mu m$ and $\rho_P = 2.44$ g/cm^3 impacting at a velocity equal to 5.97 km/s is able to reach depth inside the aerogel of 13 mm [51]. These measures have to be re-scaled to particle sizes and impact velocities characteristics of the capture problem described in this work. Assuming that the aerogel

carried aboard for this mission will have the same properties of the one used for the test, it is possible to approximate the thickness that the aerogel tiles shall have from the capacity of dissipating kinetic energy. In particular, recovering the dissipation per unit length that the panel is able to grant as reported in Equation 6.1, the length required for the mission can be approximated as done in Equation 6.2:

$$\bar{E} = \frac{\frac{1}{2}\left(\frac{4}{3}\pi r_P^3\right)\rho_P v^2}{l_{depth}} = 3.7828 \cdot 10^{-7} \; J/m \tag{6.1}$$

$$l_{thick} = \frac{E_{kin_{max}}}{\bar{E}} \simeq 509 \; m \tag{6.2}$$

Such a value is completely unfeasible for the kind of mission proposed, therefore another approach shall be considered. Specifically, from Burchell et al. [53], a relation between track length and aerogel density is available. The figure of interest is the one reported in Figure 6.3.
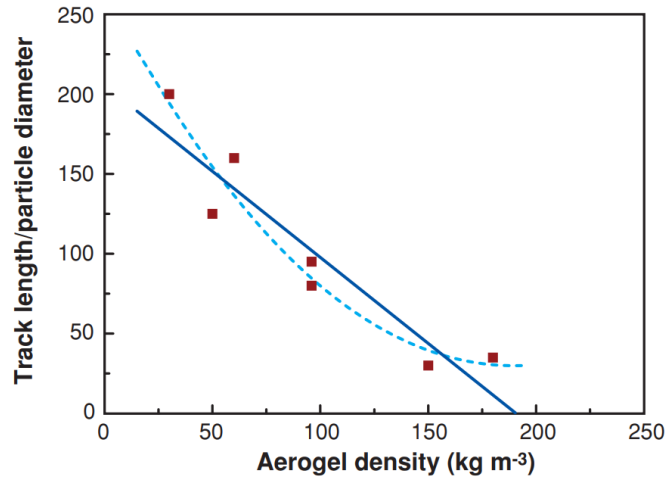
Figure 6.3: Track length over particle diameter VS aerogel density [53].

Considering the mean density between the layers as the aerogel density (i.e. 20 kg/m^3), it is possible to find that a track length over the ejecta diameter equal to ~ 182.64 [1]. Following this approach, the estimated track length enabling to collection also the biggest particles is $l = 3.6528$ m. Moreover, in NASA/JPL *Return Capsule press-kit*[2] it is assessed that the sizes of the particles that Stardust-NeXT was expecting to collect ranged mostly from less than a micron to nearly a millimeter. This interval is close to the one proposed

---

[1]To recover this value the open source *WebPlotDigitizer* available online has been exploited.
[2]https://www.jpl.nasa.gov/missions/stardust

for this new mission, which expects sizes up to 10 mm. Moreover, in the same paper, it is said that the carrot-shaped track created by the impacting particle can reach up to 200 times the dimension of the particle itself (thus close to the one found following Burchell et al.) leading in this case to $l = 4m$. However, these data were provided for different sizes and impact velocities ($5 - 6$ km/s), evidencing how these values are not possible to be clearly understood but rather they have to be simulated again in laboratory to grant the effectiveness and efficiency of the capture.
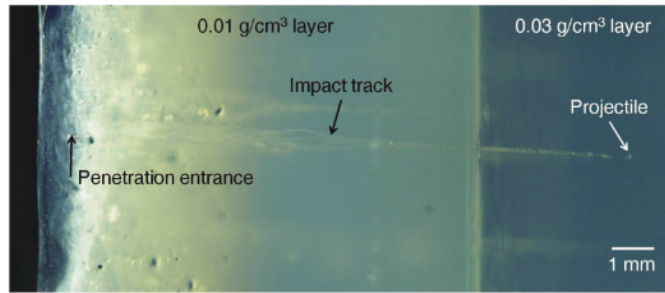
Figure 6.4: Track of a projectile with $r_P = 30\mu m$ and $\rho_P = 2.44 g/cm^3$ impacting at a velocity equal to $5.97 km/s$. The particle penetrates up to $13mm$ [51].

Another important feature that can be deduced from Figure 6.4 regards the transparency of the medium. This grants the ability to easily localize and remove capture particles, tasks that can be considered as important as the capture itself since, of course, not finding a captured particle is equivalent to no capture at all. Localizing $\mu m - mm$ particles in a wide enough collecting surface is already a cumbersome task; with an opaque medium this will become nearly impossible. Sticking into this, it is now evident the importance of both capture efficiency and extractability. This is why transparency of aerogel is an important property to not be underestimated. For this purpose NASA's Johnson Space Center (Houston, Texas) has a laboratory with specially designed equipment to optically scan the aerogel and locate captured grains within it, already used for the Stardust-NExT mission. Therefore, this step does not represent a novelty nor a demand for any technology development but could be directly applied also for the mission proposed in this thesis. Another main aspect of such collection strategy is its simplicity: being a passive technique, in fact, aerogel capture does not require precision pointing, mechanisms to warm up or any other kind of devices [50]. This finally results in high simplicity and reliability for the technology.

Once in position, similar to what happened in Stardust-NeXT, the spacecraft shall open a kind of tennis-racket-shaped catcher filled with aerogel, shown in Figure 6.5. Finished the capture, this device will fold down into a return capsule, enclosing the sample for its safe delivery to Earth.
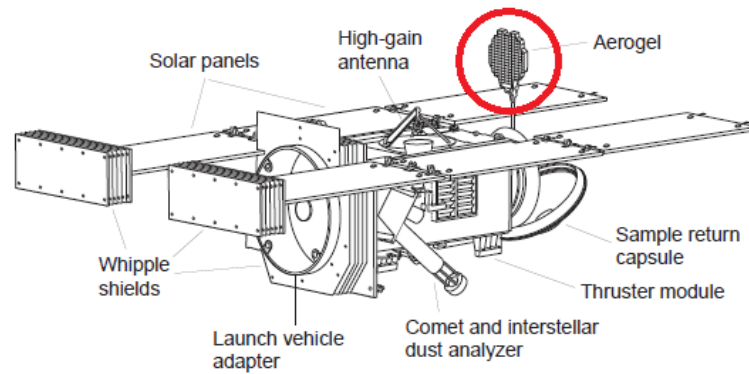
Figure 6.5: Stardust spacecraft. The red circle evidences the tennis-racket-shaped deployable collector filled with aerogel.

Such a device shall of course be linked to a *holder* rather than directly in contact with the aerogel. This shall be designed accordingly to aerogel panel dimensions and must maximise the exposure area. The most widely used approach is to fabricate a body case with aluminum alloy A7075, shaping it as a gridded lid (see Figure 6.6). In particular, Tabata et al. [54] reports that, for an aerogel of 92 mm $\times$ 92 mm, the final exposure area is approximately 56 cm^2, therefore having the holder covering about the 33.84% of the aerogel surface. This means that if, as in the case of Stardust-NeXT, the exposure area wanted is around 1040 cm^2, the actual surface considering also the holder is $\simeq$ 1392 cm^2.
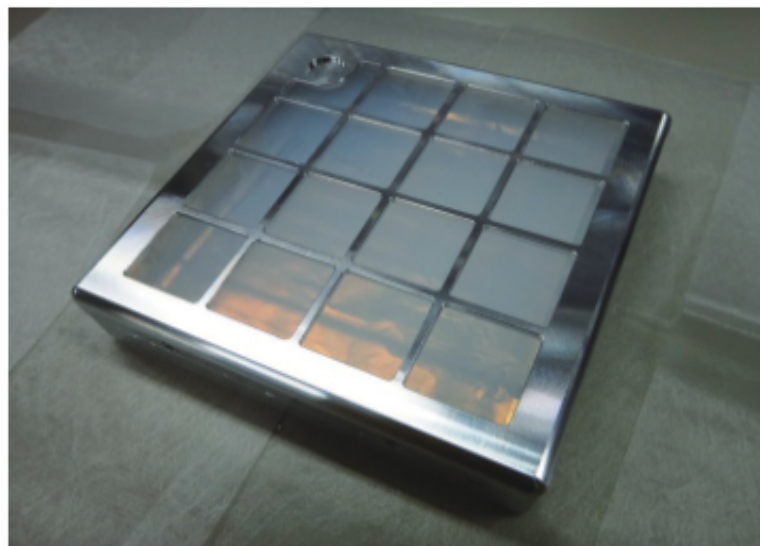
Figure 6.6: Holder mounted on a prototype aerogel [54].

Regarding instead the other subsystems, the main requirements on them will be:

- **Propulsion subsystem:** the thrusters shall be located on the opposite side of the

spacecraft with respect to the one where the collector will be deployed. Moreover, monopropellant systems are preferred for this kind of application and therefore this solution could represent a good baseline.

- **Attitude control subsystem:** shall be able to fix the spacecraft's orientation in space, keeping constantly the aerogel collector pointed towards the ejecta arriving direction.

- **Thermal control subsystem:** exploiting louvers, coatings and MLI, this subsystems shall be able to maintain the spacecraft and all its elements within their temperature ranges. The collector, being external to the actual S/C (when deployed) and due to the fact that aerogel is a thermal insulator, can be initially studied through a 1-node approximation.

- **Power subsystems:** shall be able to provide at each component the power needed for it to work. The principal solution for this kind of mission is represented by the use of solar arrays.

To summarise everything up, the main advantages of the use of aerogel for this type of on-orbit capture are:

- aerogel is an already tested and space-proven technology.

- aerogel passed both pressurization/re-pressurization and vibration tests [54].

- due to its mesostructure, aerogel features and high emissivity. It therefore does not trap heat and is insensitive to the thermal cycles proper of space environment.

- aerogel's transparency grants traceability of trapped particles., which can be then detected and extracted with relative ease.

- aerogel capture is relatively simple, therefore improving simplicity and reliability.

- being inorganic, aerogel is impervious to radiation and to ionic erosion [50].

- having an ultra-low density, even for a very large collector no mass constraints will arise.

- aerogel enables intact particle capture, preserving particles' elemental composition, structural phases, morphology and chemical isotopic composition.

On the other hand, aerogel have never been used for this range of velocities. In fact, it is generally adopted to stop cosmic dust impacting with hypervelocities (km/s) while in this mission's scenario, with the assumptions explained earlier, the velocities considered

are one order of magnitude lower. Capture efficiency in these conditions still has to be proven.

7 | Conclusions and future developments

In this chapter, the most relevant outcomes of the work will be exposed but, at the meantime, its limits will be highlighted in terms of assumptions and future developments to be done. Having assessed in Chapter 3 the necessity to surpass the approach carried on by Latino et al. in [1], the interpolation approached proposed in this work will be the matter of the discussion.

First of all, the number of sample trajectories found to escape propagating each initial condition for a maximum of 90 days is 16610. This number does not change when considering point mass or rigid body approximation, since it does not depend on the number of collision occurring. A data that can be partially seen as a confirmation of the work carried on, regards the category $Escape_{reb}$ which, due to the energy dissipated within each collision, is empty. This means that all the 16610 found to escape comes from a direct run away of the ejecta. Furthermore, these trajectories are found able to escape for $\theta < 100°$ and $200° < \theta < 350°$, identifying two distinct groups of initial conditions enabling a particle to leave the system. Even though the second is the one providing the vast majority of ejecta, for both these groups the amount of escaping orbits grows with the size: interestingly, no particles with $r_P = 78.5 \ \mu m$ are found able to leave Ryugu independently of the ejection conditions. This behavior can be probably attributed to the tightness of the bottleneck shown in Figure 4.4 (on the right) and to the value chosen for C'. Moreover, studying how γ_{ej} affects this behavior, it is found out that that the best possible conditions to grant an escape are the ones that make a particle ejecting towards the bottleneck. Although, considering TDM1 and PM, the trajectories orbiting Ryugu are 28810 (of which 23222 orbit after a rebound) and those that have not impacted yet with it are 135645 (of which 36718 impact after a rebound) and 206766 (of which 62208 impact after a rebound) for in-range and out-range collision respectively, their inter-particle effects have been here considered to be safely negligible. Nevertheless, other inter-particle effects ignored in this dissertation such as the ejecta electrostatic coupling and the particle-particle collisions have actually a relevant influence: these, even

tough not so crucial in the advanced ejecta plume behavior, represent a crucial aspect to define the particles' dimension and velocity distributions which characterize the firsts instants of the ejecta plume. Quoting Larson and Sarid [55], the distribution will either experience an increased particle's size due to accretion or a decreased dimension due to ejecta break up during collisions. This, as underlined in the whole work presented, will strongly affect the perturbation induced by the SRP. Concerning again SRP, in this work the succession of the eclipses, i.e. moments in which $\beta = 0$, have not been considered, therefore leading to important differences in the dynamics. Moreover, the propagation of the sample trajectories are not proportional to the actual number of particles ejected from a crater, therefore requiring a more detailed investigation.

Apart from the number of escaped ejecta, the other key parameter is the time required to perform the collection. In particular, it is found that, experiencing a higher SRP acceleration, the dynamics of smaller particles will be faster, meaning that the larger an ejecta the longer it will take to leave the system. In order to quantify then the amount of time needed to retain the mission successful, only particles having $r_P = 1.181$ mm and $r_P = 2.283$ mm are considered. This derive from the choice of the smaller neck orbit between those considered in Figure 4.6 which, granting a fast scanning of the bottleneck, is here assumed to maximise the capture probability. All the particles exiting having the dimensions previously reported are in fact considered to be all captured. This not only is not completely true, but also the neck orbit itself will require to be better identified. However, with these simplifications, after 22.48 days (i.e. 23 days), the mission is found able to gather 1.8040 g and 3.458 g from particles having, in the order, $r_P = 1.181$ mm and $r_P = 2.283$ mm. The total mass accumulated found with this approach is therefore equal to 5.262 g, equal to the one collected by Hayabusa2 according to [16]. This has been considered a good baseline threshold able to identify a satisfying amount of material required to gather.

Concerning instead the preliminary design of the capture mechanism, the optimal strategy is to exploit a silica-based aerogel able to trap the particles inside its mesostructure. At first, a study on the kinetic energy of the ejecta when colliding with aerogel has been performed. However, the energy has been recovered assuming as impact velocity the one that the ejecta will have at $t = tof$, suggesting that the capture occurs at the same instant that the simulation found the particle escapes from the Hill's sphere. This is a huge simplification of the problem which, furthermore, takes as impact velocity just the one of the ejecta instead of the relative speed between the satellite and the particle itself. Anyway, besides all these hypothesis, it is found that the maximum kinetic energy required to be dissipated by the aerogel is equal to $E_{kin_{max}} = 1.9258 \cdot 10^{-4}$. Note that, even though is said that the capture would interest only ejecta with $r_P \leq 2.283$ mm, this value corresponds

to a particle having $r_P = 10$ mm, that is not excluded here to stay as conservative as possible. Moreover, this quantity has been found to be physically limited since for larger dimensions, that are those presenting the higher v_{ej}, V_{cap} will be the lower. In any case, capture velocity is between 100 and 300 m/s.

Knowing the maximum kinetic energy, this work assessed, exploiting reference trends found in literature, a minimum thickness of the aerogel tiles of about 4 m: this values is however not reliable since those studies were carried on for different particle's sizes and velocity. The best option would be to simulate again in laboratory to assess the effectiveness, efficiency and quality of the capture. When the capture-phase begins, the aerogel tiles are exposed to space deploying a racket-shaped catcher as the one used in the Stardust-NeXT mission. This must be attached to a gridded aluminum-based holder: investigating Tanpopo and Stardust-NeXT mission the preliminary analysis returns a surface area $\simeq 1392$ cm^2.

Apart from those already exposed, two other main future studies would strongly improve the quality of the dissertation: first, the dynamics shall be expanded to the elliptical case, analysing the Elliptical Restricted Three-Body Problem; second, the point mass model, here assumed as the baseline due to its more conservative nature, shall be refined not by a rigid body assumption, but rather considering the tangential compliance caused by the elastic deformation that would take place during the impact. Although its effect is expected to be negligible for a low-velocity impact, it might be a subject of interest for future research [17].

To conclude, the submitted work, even though with several simplifying assumptions, has been able to assess the feasibility of an on-orbit asteroid's sample collection by means of a satellite orbiting around a libration point. Exploiting an aerogel-based capture strategy, in fact, the proposed mission is able to collect 5.262 g of Ryugu's ejecta in 23 days from the arrive at the asteroid.

Bibliography

[1] A. Latino, "Ejecta orbital and bouncing dynamics around asteroid ryugu," 2019.

[2] M. Trisolini, C. Colombo, Y. Tsuda, *et al.*, "Ejecta dynamics around asteroids in view of in-orbit particle collection missions," in *72nd International Astronautical Congress (IAC 2021)*, pp. 1–10, 2021.

[3] S. Takahashi and D. J. Scheeres, "Autonomous exploration of a small near-earth asteroid," *Journal of Guidance, Control, and Dynamics*, vol. 44, no. 4, pp. 701–718, 2021.

[4] M. Trisolini, C. Colombo, and Y. Tsuda, "Ejecta models for particles generated by small kinetic impactors onto asteroid surfaces," in *AIAA Scitech 2022 Forum*, p. 2383, 2022.

[5] D. Scheeres, D. Durda, and P. Geissler, "The fate of asteroid ejecta," *Asteroids III*, vol. 1, pp. 527–544, 2002.

[6] G. Zhai, Y. Qiu, B. Liang, and C. Li, "On-orbit capture with flexible tether–net system," *Acta Astronautica*, vol. 65, no. 5-6, pp. 613–623, 2009.

[7] A. Flores-Abad, L. Zhang, Z. Wei, and O. Ma, "Optimal capture of a tumbling object in orbit using a space manipulator," *Journal of Intelligent & Robotic Systems*, vol. 86, no. 2, pp. 199–211, 2017.

[8] S. Soldini and Y. Tsuda, "Assessing the hazard posed by ryugu ejecta dynamics on hayabusa2 spacecraft," in *26th International Symposium of Space Flight Dynamics*, pp. 1–11, 2017.

[9] B. Koberlein, "Why the asteroid belt doesn't threaten spacecraft," *Universe Today*, 2014.

[10] A. Turconi, *Modelling small bodies gravitational potential for autonomous proximity operations.* PhD thesis, University of Surrey, 2018.

[11] I. E. Johansson, T. Tsareva, J. Griswold, P. Lubin, G. B. Hughes, H. O'Neill, P. Mein-

hold, J. Suen, Q. Zhang, J. Riley, *et al.*, "Effects of asteroid rotation on directed energy deflection," in *Nanophotonics and Macrophotonics for Space Environments VIII*, vol. 9226, pp. 71–84, SPIE, 2014.

[12] D. J. Tholen, *Asteroid taxonomy from cluster analysis of photometry.* The University of Arizona, 1984.

[13] B. Carry, "Density of asteroids," *Planetary and Space Science*, vol. 73, no. 1, pp. 98–118, 2012.

[14] Y. Shi, Y. Wang, and S. Xu, "Global search for periodic orbits in the irregular gravity field of a binary asteroid system," *Acta Astronautica*, vol. 163, pp. 11–23, 2019.

[15] D. Karydis, G. Voyatzis, and K. Tsiganis, "A continuation approach for computing periodic orbits around irregular-shaped asteroids. an application to 433 eros," *Advances in Space Research*, vol. 68, no. 11, pp. 4418–4433, 2021.

[16] T. Yada, M. Abe, T. Okada, A. Nakato, K. Yogata, A. Miyazaki, K. Hatakeda, K. Kumagai, M. Nishimura, Y. Hitomi, *et al.*, "Preliminary analysis of the hayabusa2 samples returned from c-type asteroid ryugu," *Nature Astronomy*, vol. 6, no. 2, pp. 214–220, 2022.

[17] S. Kikuchi, N. Ogawa, O. Mori, T. Saiki, Y. Takei, F. Terui, G. Ono, Y. Mimasu, K. Yoshikawa, S. Van Wal, *et al.*, "Ballistic deployment of the hayabusa2 artificial landmarks in the microgravity environment of ryugu," *Icarus*, vol. 358, p. 114220, 2021.

[18] C. Colombo, "Orbital mechanics course slides - three body problem," 2021.

[19] C. Lhotka and A. Celletti, "The effect of poynting–robertson drag on the triangular lagrangian points," *Icarus*, vol. 250, pp. 249–261, 2015.

[20] D. Westra, "Lagrangian points," 2017.

[21] W. S. Koon, M. W. Lo, J. E. Marsden, and S. D. Ross, "Dynamical systems, the three-body problem and space mission design," in *Equadiff 99: (In 2 Volumes)*, pp. 1167–1181, World Scientific, 2000.

[22] V. Szebehely, *Theory of orbit: The restricted problem of three Bodies.* Elsevier, 2012.

[23] F. R. Moulton, *An introduction to celestial mechanics.* Courier Corporation, 1970.

[24] Y. Yu, P. Michel, S. Schwartz, S. Naidu, and L. Benner, "Ejecta cloud from a kinetic impact on the secondary of a binary asteroid: I," *Mechanical Environment and Dynamic Model.(in preperation)*, 2016.

[25] A. B. Batkhin, "Families of symmetric periodic solutions of the generalized hill's problem,"   .   , no. 0, pp. 60–24, 2013.

[26] V. Szebehely, "Stability of planetary orbits in binary systems," *Celestial mechanics*, vol. 22, no. 1, pp. 7–12, 1980.

[27] M. Hénon, "Numerical exploration of the restricted problem, v," *Astronomy and Astrophysics*, vol. 1, pp. 223–238, 1969.

[28] G. W. Hill, "On the part of the motion of the lunar perigee which is a function of the mean motions of the sun and moon," *Acta mathematica*, vol. 8, no. 1, pp. 1–36, 1886.

[29] K. Nakazawa and S. Ida, "Hill's approximation in the three-body problem," *Progress of Theoretical Physics Supplement*, vol. 96, pp. 167–174, 1988.

[30] M. Lara and J. F. Palacián, "Hill problem analytical theory to the order four: application to the computation of frozen orbits around planetary satellites," *Mathematical Problems in Engineering*, vol. 2009, 2009.

[31] D. Villegas-Pinto, S. Soldini, Y. Tsuda, and J. Heiligers, "Temporary capture of asteroid ejecta into periodic orbits: Application to jaxa's hayabusa2 impact event," in *AIAA Scitech 2020 Forum*, p. 0221, 2020.

[32] B. A. Gustafson, "Physics of zodiacal dust," *Annual Review of Earth and Planetary Sciences*, vol. 22, pp. 553–595, 1994.

[33] L. Dell'Elce, N. Baresi, S. Naidu, L. Benner, and D. Scheeres, "Numerical investigation of the dynamical environment of 65803 didymos," *Advances in Space Research*, vol. 59, no. 5, pp. 1304–1320, 2017.

[34] D. Garcia Yarnoz, J.-P. Sanchez Cuartielles, and C. R. McInnes, "Passive sorting of asteroid material using solar radiation pressure," *Journal of Guidance, Control, and Dynamics*, vol. 37, no. 4, pp. 1223–1235, 2014.

[35] O. Rodrigues, *De l'attraction des sphéroïdes, Correspondence sur l'É-cole Impériale Polytechnique*. PhD thesis, PhD thesis, Thesis for the Faculty of Science of the University of Paris, 1816.

[36] S. Bucciarelli, M. Ceccaroni, A. Celletti, and G. Pucacco, "Qualitative and analytical results of the bifurcation thresholds to halo orbits," *Annali di Matematica Pura ed Applicata (1923-)*, vol. 195, no. 2, pp. 489–512, 2016.

[37] E. Buhl, F. Sommer, M. H. Poelchau, G. Dresen, and T. Kenkmann, "Ejecta from

experimental impact craters: Particle size distribution and fragmentation energy," *Icarus*, vol. 237, pp. 131–142, 2014.

[38] K. R. Housen and K. A. Holsapple, "Ejecta from impact craters," *Icarus*, vol. 211, no. 1, pp. 856–875, 2011.

[39] S. Raducan, T. Davison, R. Luther, and G. Collins, "The role of asteroid strength, porosity and internal friction in impact momentum transfer," *Icarus*, vol. 329, pp. 282–295, 2019.

[40] Y. Yu, *Orbital dynamics in the gravitational field of small bodies*. Springer, 2016.

[41] M. Hénon, "Exploration numérique du problème restreint. i. masses égales; orbites périodiques," in *Annales d'Astrophysique*, vol. 28, p. 499, 1965.

[42] M. Stramacchia, "Master thesis: Distant periodic orbits for asteroid detection," 2013.

[43] D. L. Richardson, "Analytic construction of periodic orbits about the collinear points," *Celestial mechanics*, vol. 22, no. 3, pp. 241–253, 1980.

[44] M. Kim and C. D. Hall, "Lyapunov and halo orbits about l2," in *Proceedings of the 2001 AAS/AIAA Astrodynamics Specialist Conference, Quebec City, Canada*, vol. 109, pp. 349–366, 2001.

[45] V. S. Kalantonis, "Numerical investigation for periodic orbits in the hill three-body problem," *Universe*, vol. 6, no. 6, p. 72, 2020.

[46] S. Soldini, *Design and control of solar radiation pressure assisted missions in the sun-earth restricted three-body problem*. PhD thesis, University of Southampton, August 2016.

[47] C. Conley, "Low energy transit orbits in the restricted three-body problems," *SIAM Journal on Applied Mathematics*, vol. 16, no. 4, pp. 732–746, 1968.

[48] J. L. Forshaw, G. S. Aglietti, T. Salmon, I. Retat, C. Burgess, T. Chabot, A. Pisseloup, A. Phipps, C. Bernal, A. Pollini, *et al.*, "The removedebris adr mission: preparing for an international space station launch," in *7th European Conference on Space Debris*, 2017.

[49] K. Yoshida and D. N. Nenchev, "Space robot impact analysis and satellite-base impulse minimization using reaction null-space," in *ICRA*, pp. 1271–1277, 1995.

[50] P. Tsou, "Silica aerogel captures cosmic dust intact," *Journal of Non-Crystalline Solids*, vol. 186, pp. 415–427, 1995.

[51] M. Tabata, Y. Kawaguchi, S.-i. Yokobori, H. Kawai, J.-i. Takahashi, H. Yano, and A. Yamagishi, "Tanpopo cosmic dust collector: silica aerogel production and bacterial dna contamination analysis," *Biological Sciences in Space*, vol. 25, no. 1, pp. 7–12, 2011.

[52] M. Tabata, H. Yano, H. Kawai, E. Imai, Y. Kawaguchi, H. Hashimoto, and A. Yamagishi, "Silica aerogel for capturing intact interplanetary dust particles for the tanpopo experiment," *Origins of Life and Evolution of Biospheres*, vol. 45, no. 1, pp. 225–229, 2015.

[53] M. J. Burchell, G. Graham, and A. Kearsley, "Cosmic dust collection in aerogel," *Annu. Rev. Earth Planet. Sci.*, vol. 34, pp. 385–418, 2006.

[54] M. Tabata, E. Imai, H. Yano, H. Hashimoto, H. Kawai, Y. Kawaguchi, K. Kobayashi, H. Mita, K. Okudaira, S. Sasaki, *et al.*, "Design of a silica-aerogel-based cosmic dust collector for the tanpopo mission aboard the international space station," *Transactions of the Japan Society for Aeronautical and Space Sciences, Aerospace Technology Japan*, vol. 12, no. ists29, pp. Pk_29–Pk_34, 2014.

[55] J. N. Larson and G. Sarid, "An n-body approach to modelling debris and ejecta off small bodies: implementation and application," *Monthly Notices of the Royal Astronomical Society*, vol. 503, no. 1, pp. 1070–1081, 2021.

A | Appendix A
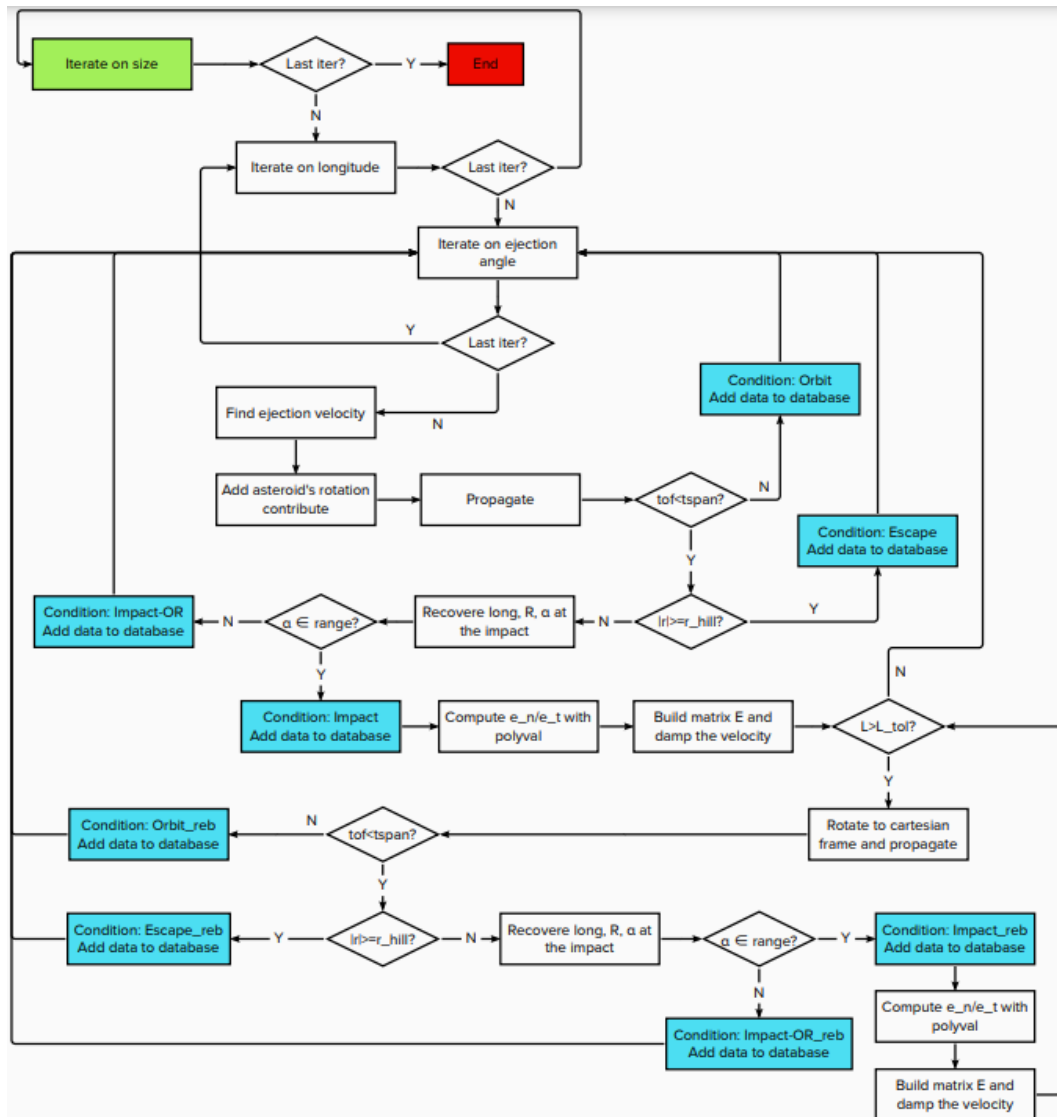
Figure A.1: Block diagram representative of the database code. Green represents the starting block, red the final one. In blue are highlighted all the blocks assessing a final condition to the ejecta, which is then added to the database.

B | Appendix B
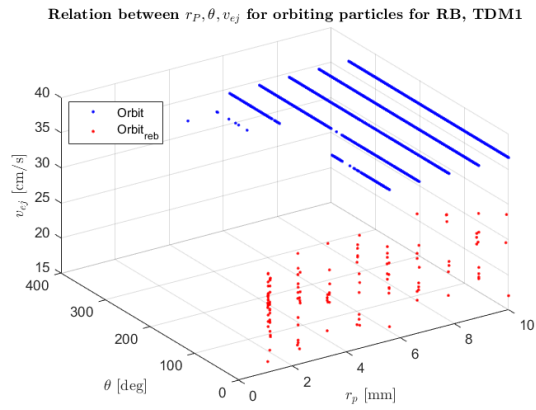
Figure B.1: Relation between r_P, θ, v_{ej} for orbiting trajectories, assuming RB and TDM1.
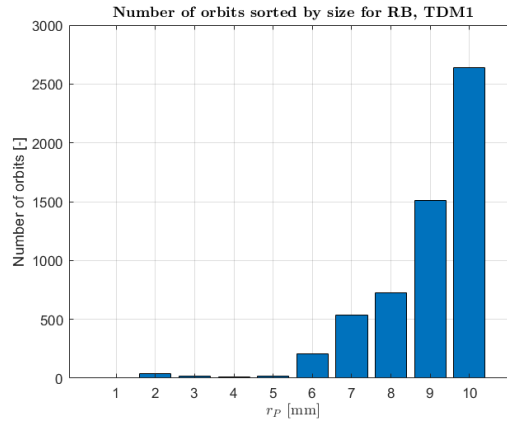
Figure B.2: Number of orbits sorted by size for RB and TDM1.
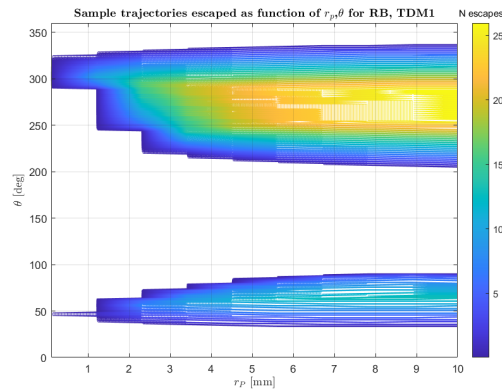
Figure B.3: Contour plot on the sample trajectories found to escape depending on r_P and θ for RB and TDM1.
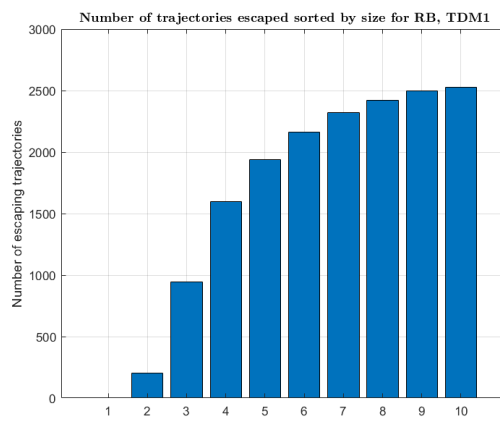
Figure B.4: Escaping sample trajectories sorted by r_P for RB and TDM1.
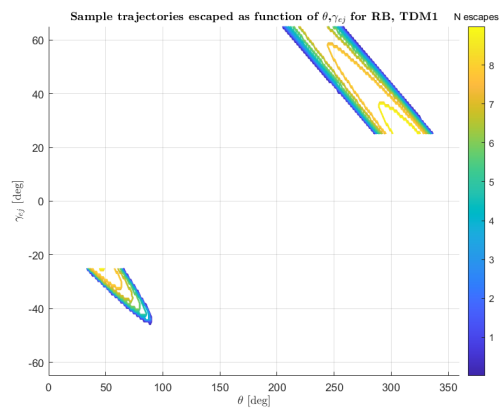
Figure B.5: Contour plot on the sample trajectories found to escape depending on θ and γ_{ej} for RB and TDM1.
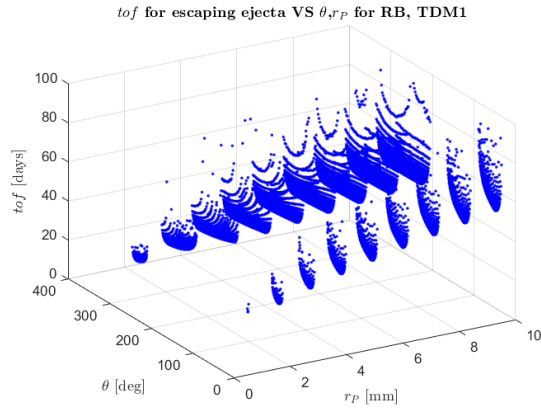
Figure B.6: Time of flight for escaping trajectories with respect to r_P, θ for RB and TDM1.
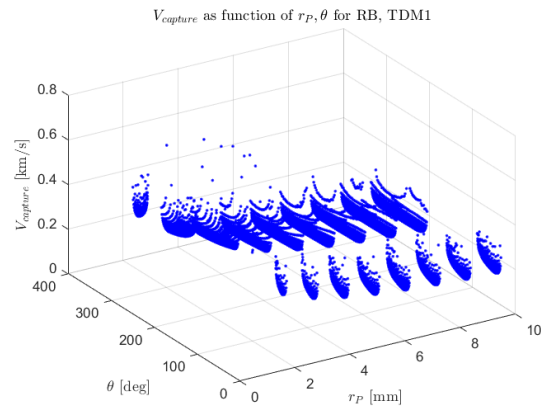
Figure B.7: Capture velocity expressed as function of r_P and θ for RB and TDM1.
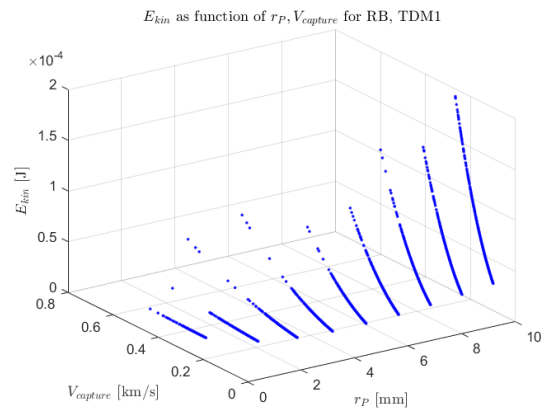
Figure B.8: Ejecta's kinetic energy when exiting from the system throughout the L2 bottleneck for RB and TDM1.
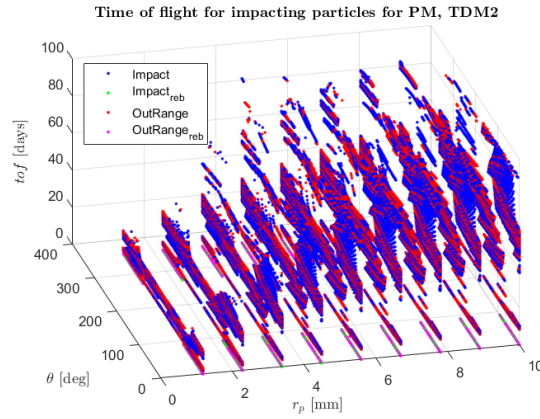
Figure B.9: Time of flight of impacting trajectories as function of r_P, θ, assuming PM and TDM2.
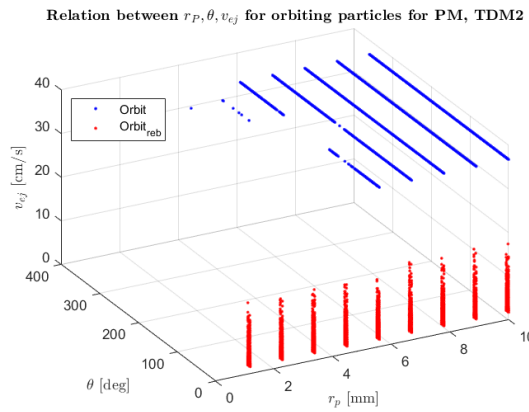
Figure B.10: Relation between r_P, θ, v_{ej} for orbiting trajectories, assuming PM and TDM2.
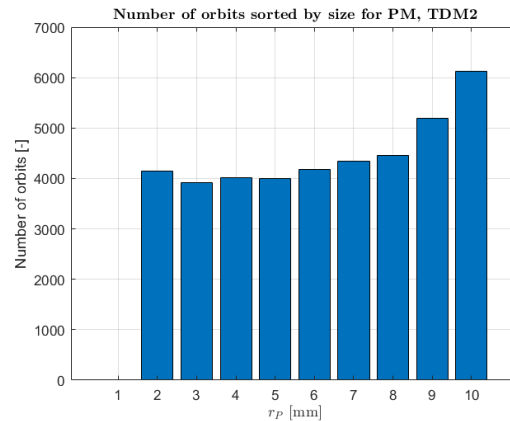
Figure B.11: Number of orbits sorted by size for PM and TDM2.
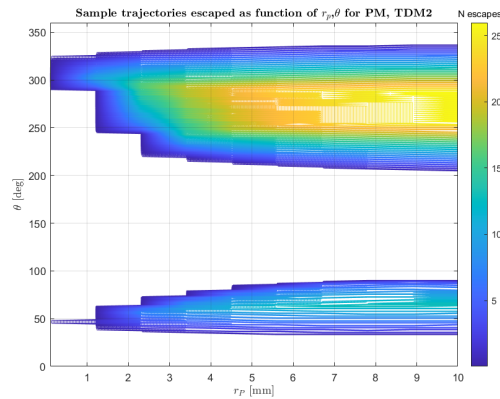
Figure B.12: Contour plot on the sample trajectories found to escape depending on r_P and θ for PM and TDM2.
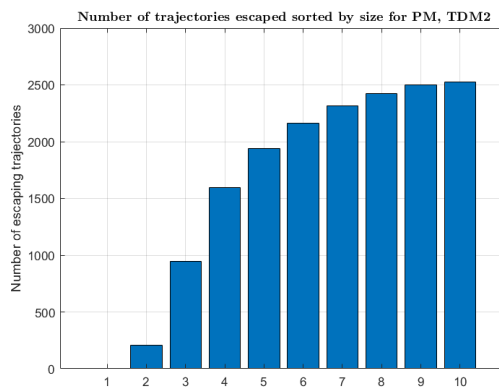
Figure B.13: Escaping sample trajectories sorted by r_P for PM and TDM2.
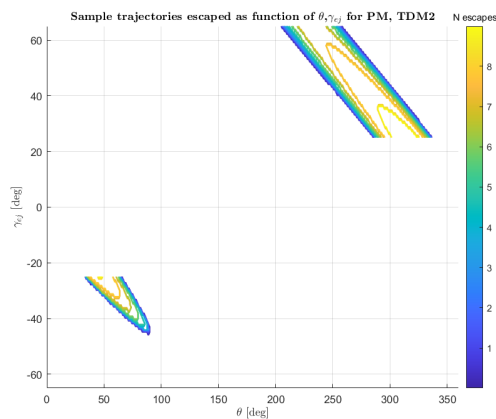
Figure B.14: Contour plot on the sample trajectories found to escape depending on θ and γ_{ej} for PM and TDM2.
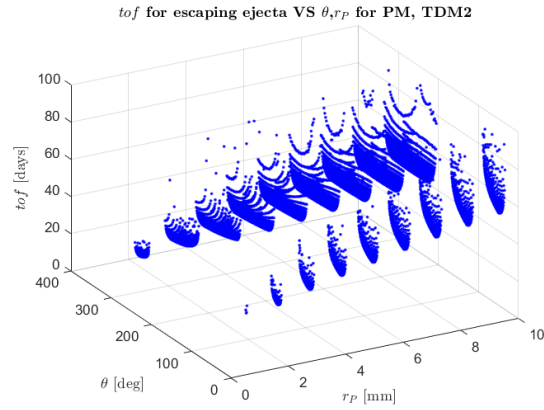
Figure B.15: Time of flight for escaping trajectories with respect to r_P, θ for PM and TDM2.
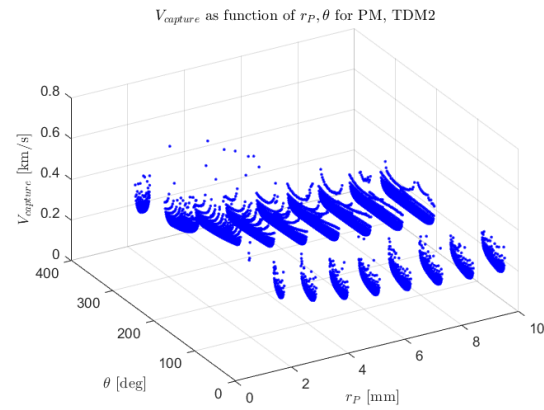
Figure B.16: Capture velocity expressed as function of r_P and θ for PM and TDM2.
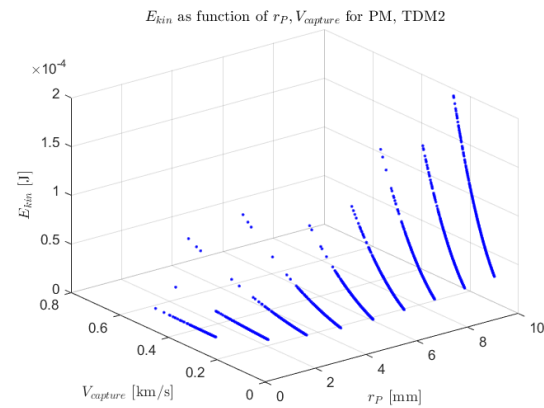
Figure B.17: Ejecta's kinetic energy when exiting from the system throughout the L2 bottleneck for PM and TDM2.
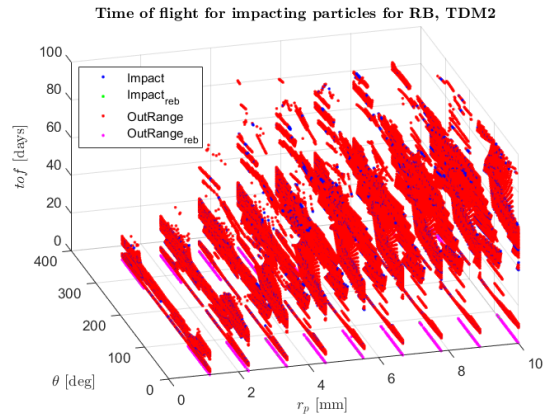
Figure B.18: Time of flight of impacting trajectories as function of r_P, θ, assuming RB and TDM2.
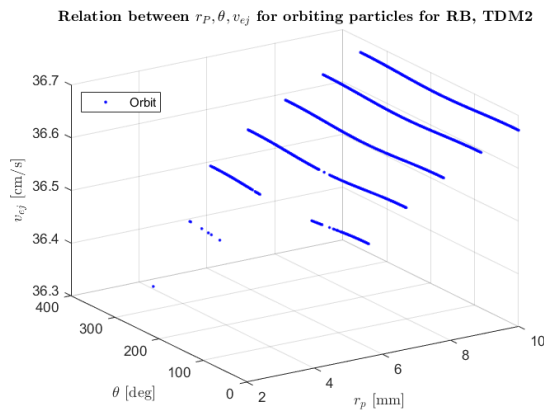
Figure B.19: Relation between r_P, θ, v_{ej} for orbiting trajectories, assuming RB and TDM2.
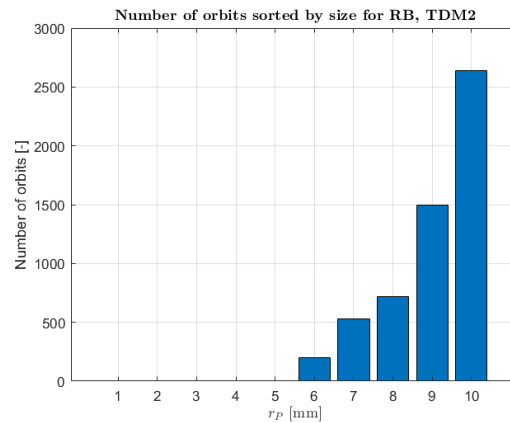
Figure B.20: Number of orbits sorted by size for RB and TDM2.
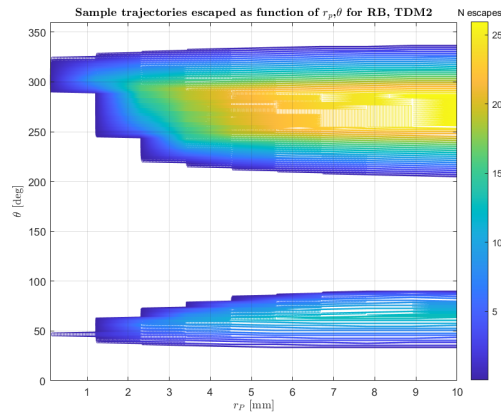
Figure B.21: Contour plot on the sample trajectories found to escape depending on r_P and θ for RB and TDM2.
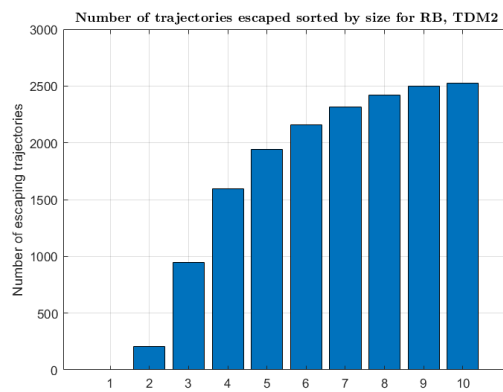
Figure B.22: Escaping sample trajectories sorted by r_P for RB and TDM2.
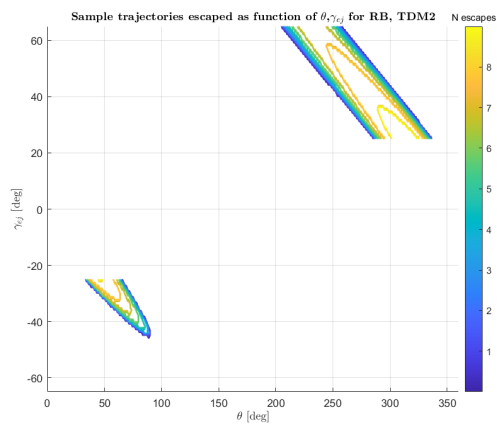
Figure B.23: Contour plot on the sample trajectories found to escape depending on θ and γ_{ej} for RB and TDM2.
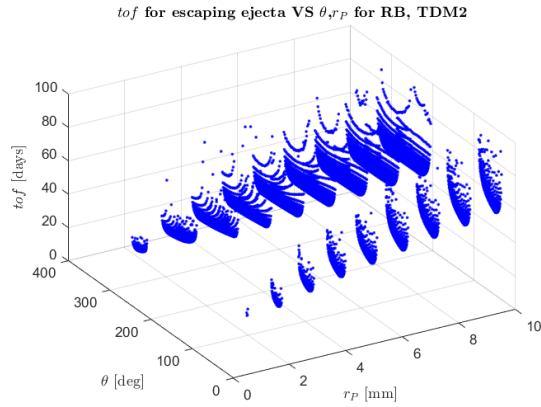
Figure B.24: Time of flight for escaping trajectories with respect to r_P, θ for RB and TDM2.
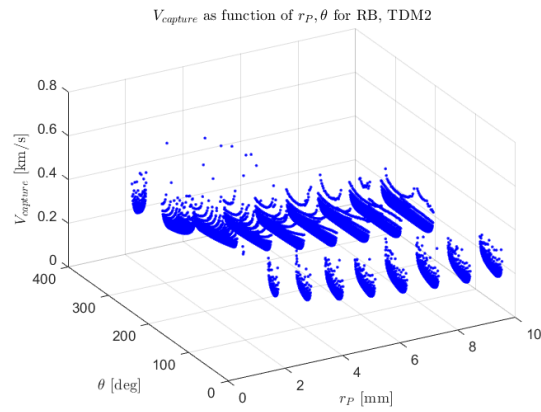
Figure B.25: Capture velocity expressed as function of r_P and θ for RB and TDM2.

Figure B.26: Ejecta's kinetic energy when exiting from the system throughout the L2 bottleneck for RB and TDM2.

List of Figures

List of Tables

Acknowledgements

To my family for the continuous trust and unconditional support.

To my lifelong forever friends who have always welcomed me back, making me feel always at home again.

To Palma and her patience with me during these months of hard work.

To the friends met done during this voyage and to the university friends, especially Fabio "The Buonfa", without whom I would have never been able to reach this achievement.

This is just the beginning of a long journey.